MASTER THESIS

Theoretical description of time-domain electromagnetic fields in the interaction of fast electrons and metallic nanoparticles

by

Andrea Konečná

Acknowledgement

Contents

CONTENTS

Introduction

The field of electron microscopy has passed a long way since its invention in early 1930s. In the beginnings, electron microscopes were capable of magnification in the order of hundreds, but nowadays they can achieve atomic resolution [45], which is possible thanks to great advances in the correction of aberrations, development of better electron sources, detectors and vacuum devices. Together with these improvements, application of many techniques employing electron microscopy started.

The first measurements by means of electron energy loss spectroscopy (EELS) were introduced by Ruthemann in 1941 [50] and by Hillier and Baker in 1944 [29]. EELS has been widely used for identifying the energies of various types of excitations in materials and in 1950s, it helped to discover the existence of surface plasmon, which were detected in thin metallic foils together with the already known bulk plasma oscillations. A theoretical explanation was given by Ritchie [48] in 1957 and the name of the excitation comes from Stern and Ferrell [51]. These and other works in the last years led to great development of the field of physics, nowadays called plasmonics.

Although it seems plasmonics is something completely new, people have known plasmons since ancient times. There can occur not only bulk or surface plasmons in metallic layers, but it is possible to observe localized surface plasmons in small metal particles as well. When we illuminate tiny particles, e.g. in colloidal solutions, we can see them shining in different colours related to their resonant frequencies, which depend on size, shape or material. This effect was employed by glass-blowers, who produced beautiful colourful glass (Lycurgus cup can serve as a nice example [38]).

This phenomena is now being intensively studied because of many possible applications derived from the confinement and enhancement of the fields associated with surface plasmons. Localized surface plasmons can be used for biodetection due to the high sensitivity of the resonant frequency to dielectric environment in surroundings of the particle and they are also employed in a branch of so-called enhanced spectroscopies (e.g. surface enhanced Raman spectroscopy or surface enhanced infrared absorption) as they help to enhance the detected signal. Great efforts are also invested in using such particles in near-field optical devices and in controlling optical signals [44].

For the development of new applications it is necessary to be able to design particles and structures of properties on demand. Many techniques to manufacture particles differing in sizes, shapes and composition exist, as well as lots of characterization methods, including spectroscopies and microscopies covering a wide variety of frequency ranges. Although developed 70 years ago, EELS still remains on of the most fundamental methods to explore resonant modes of these nanoparticles. Due to the evanescent nature of the fields produced by moving electrons, EELS can reveal not only bright, but also dark modes [33], therefore providing very detailed information about the particles and the nanostructures.

The fields around tiny particles, generated by swift electrons, can also induce forces acting on them. These phenomena cause the nanoparticle motion and can be employed as a tool for manipulation at nanoscale [7], [10], [54]. Because of the resolution of electron microscopes, these "electron tweezers" can be much more accurate than conventional techniques used for this purpose [53]. However, it shows up that the nature of the forces is not only attractive with respect to the beam as one would expect intuitively, but in some cases there can exist repulsion between the electron beam and the nanoparticle [7], [47], [21]. The aim of this work is to explain the ambiguous nature of the forces acting on plasmonic nanoparticles.

In the first chapter we introduce fundamental quantities related to the electromagnetic field and provide a basis to develop the different parts of the thesis. In the next two chapters, we focus on electron energy loss spectroscopy and the different numerical approaches that are often used to calculate electron energy loss spectra and maps of induced fields in metal particles.

In the fourth chapter we deal with the approach developed by García de Abajo [20] leading to an analytical expressions for the fields induced by electrons near spherical particles. We then show the resonance modes in frequency domain and compare our results with numerical calculations. Then we apply a Fourier transformation to calculate the time dependence of the electromagnetic fields and reveal the evolution of the fields in different regimes of time. Within the last chapter, the time dependence of integrated Maxwell stress tensor will be expressed, trying to understand the fundamental principles leading to nanoparticle motion. Unraveling the complex dynamics induced by fast electron beams might provide a tool to manipulate matter in the nanoscale.

1. Electromagnetic fields

In this chapter we start with the theory of electromagnetic fields as we need to introduce the relevant quantities, the formalism and setting the basis for the following chapters. SI units are used throughout this chapter. Conversion to Gaussian units can be found e.g. in [32].

1.1. Maxwell's equations and material relationships

Electromagnetic fields can be expressed by means of four fundamental equations named after the Scottish mathematical physicist James Clerk Maxwell. The form of these equations that we use nowadays was introduced by Oliver Heaviside.

   The first equation is also called Gauss's law and it connects the electric displacement $\mathbf{D}$ with the density of free charge ρ_F [32], [52]:

$$\nabla \cdot \mathbf{D} = \rho_F, \qquad \oiint_{\partial V} \mathbf{D} \cdot \mathrm{d}\mathbf{S} = \iiint_V \rho_F \mathrm{d}V. \tag{1.1}$$

An equivalent equation, which holds for the magnetic field $\mathbf{B}$, establishes that there exists no magnetic monopole in nature:

$$\nabla \cdot \mathbf{B} = 0, \qquad \oiint_{\partial V} \mathbf{B} \cdot \mathrm{d}\mathbf{S} = 0. \tag{1.2}$$

The third equation is Faraday's law of induction which shows that the change of the magnetic field $\mathbf{B}$ with time gives rise to an electric field $\mathbf{E}$

$$\nabla \times \mathbf{E} = -\frac{\partial \mathbf{B}}{\partial t}, \qquad \oint_{\partial S} \mathbf{E} \cdot \mathrm{d}\mathbf{s} = -\frac{\mathrm{d}}{\mathrm{d}t} \iint_S \mathbf{B} \cdot \mathrm{d}\mathbf{S}, \tag{1.3}$$

and similarly Ampére's law with Maxwell's displacement current shows that we can expect magnetizing field $\mathbf{H}$ in the presence of free current density $\mathbf{J}_F$ or when the electric displacement $\mathbf{D}$ is changing with time:

$$\nabla \times \mathbf{H} = \mathbf{J}_F + \frac{\partial \mathbf{D}}{\partial t}, \qquad \oint_{\partial S} \mathbf{H} \cdot \mathrm{d}\mathbf{s} = \iint_S \mathbf{J}_F \cdot \mathrm{d}\mathbf{S} + \frac{\mathrm{d}}{\mathrm{d}t} \iint_S \mathbf{D} \cdot \mathrm{d}\mathbf{S}. \tag{1.4}$$

   In equations (1.1)–(1.3) We presented the "macroscopic" set of Maxwell's equations and showed both the differential and the integral form which are suitable for different purposes. The equivalence of these two forms can be derived from the divergence theorem [Eqs. (1.1) and (1.2)] and Stokes' theorem [Eqs. (1.3) and (1.4)].

   The relationship between $\mathbf{E}$ and $\mathbf{D}$ can be written as

$$\mathbf{D} = \varepsilon_0 \mathbf{E} + \mathbf{P}, \tag{1.5}$$

where $\mathbf{P}$ is the polarization of the material and ε_0 is the electric permittivity of vacuum, while for vectors related to magnetic fields

$$\mathbf{H} = \frac{\mathbf{B}}{\mu_0} - \mathbf{M} \tag{1.6}$$

holds. μ_0 is the magnetic permeability of vacuum and $\mathbf{M}$ the magnetization of material. Both $\mathbf{P}$ and $\mathbf{M}$ express an average dipole moment per unit volume, electric in the case of polarization or magnetic when we refer to magnetization.

If we write the total charge density (ρ) as the sum of free (ρ_F) and bounded (ρ_B) charges and the current density ($\mathbf{J}$) as the sum of free ($\mathbf{J}_F$) and bounded ($\mathbf{J}_B$) current densities, respectively,

$$\rho = \rho_F + \rho_B, \qquad (1.7) \qquad\qquad \mathbf{J} = \mathbf{J}_F + \mathbf{J}_B \qquad (1.8)$$

and plug Eqs. (1.5), (1.6), (1.7) and (1.8) into Eqs. (1.1) and (1.4), we obtain the following relationships for bound charge and current densities:

$$\nabla \cdot \mathbf{P} = -\rho_B, \qquad (1.9) \qquad\qquad \mathbf{J}_B = \nabla \times \mathbf{M} + \frac{\partial \mathbf{P}}{\partial t}. \qquad (1.10)$$

If we further apply the divergence operator to equation (1.4), apply that $\nabla \cdot \nabla \times \mathbf{V} = 0$ and use Eqs. (1.7), (1.8), (1.9) and (1.10), the continuity equation is revealed:

$$\nabla \cdot \mathbf{J} + \frac{\partial \rho}{\partial t} = 0. \qquad (1.11)$$

In linear, homogeneous and non-magnetic media other two important relationships hold, namely

$$\mathbf{D} = \varepsilon \mathbf{E} \qquad (1.12)$$

and

$$\mathbf{B} = \mu \mathbf{H}, \qquad (1.13)$$

where ε stands for electric permittivity and μ for magnetic permeability of the material and thus describe its properties. When we compare Eqs. (1.12) and (1.13) with Eqs. (1.5) and (1.6), we obtain the expressions for the polarization and magnetization:

$$\mathbf{P} = \varepsilon_0 \chi_E \mathbf{E}, \qquad (1.14) \qquad\qquad \mathbf{M} = \chi_M \mathbf{H}, \qquad (1.15)$$

where χ_E is electric susceptibility and χ_M magnetic susceptibility defined via

$$\chi_E = \frac{\varepsilon}{\varepsilon_0} - 1 = \varepsilon_r - 1, \qquad (1.16) \qquad\qquad \chi_M = \frac{\mu}{\mu_0} - 1 = \mu_r - 1. \qquad (1.17)$$

To complete material relationships, we mention the generalized Ohm's law in differential form for linear media without dispersion in time and space:

$$\mathbf{J} = \sigma \mathbf{E}, \qquad (1.18)$$

with σ denoting the conductivity of the material. If we consider non-locality in time and space, the right-hand sides of Eqs. (1.12) and (1.18) have to be replaced by the convolution:

$$\mathbf{D}(\mathbf{r},t) = \iiiint \mathrm{d}t' \mathrm{d}\mathbf{r}' \varepsilon(\mathbf{r}-\mathbf{r}',t-t')\mathbf{E}(\mathbf{r}',t') \qquad \mathbf{J}(\mathbf{r},t) = \iiiint \mathrm{d}t' \mathrm{d}\mathbf{r}' \sigma(\mathbf{r}-\mathbf{r}',t-t')\mathbf{E}(\mathbf{r}',t'), \quad (1.19)$$

where we integrate over the whole space and at all times. Previous expressions are recovered, when the response functions ε and σ are proportional to a delta distribution (see Appendix A), which is

fulfilled for a local response. We can also see that the response functions in Eq. (1.19) depend only on the differences of position vectors $(\mathbf{r} - \mathbf{r}')$ and time $(t - t')$. This is due to the homogeneity of the system.

1.2. Wave equation

If we apply the curl on Faraday's and Ampére-Maxwell's law in the absence of charges and currents and use the vector identity $\nabla \times \mathbf{V} = \nabla(\nabla \cdot \mathbf{V}) - \nabla^2 \mathbf{V}$, we obtain

$$\nabla(\nabla \cdot \mathbf{E}) - \nabla^2 \mathbf{E} = -\nabla \times \left(\tfrac{\partial \mathbf{B}}{\partial t}\right), \tag{1.20}$$

$$\nabla(\nabla \cdot \mathbf{H}) - \nabla^2 \mathbf{H} = \nabla \times \left(\tfrac{\partial \mathbf{D}}{\partial t}\right). \tag{1.21}$$

In Eq. (1.20) we can substitute $\mathbf{B}$ as in Eq. (1.13) and Eq. (1.12) can be used in Eq. (1.21) to replace $\mathbf{D}$ by $\mathbf{E}$. If $\nabla \varepsilon = 0$ and $\nabla \mu = 0$ hold, the first terms on the left-hand sides of Eqs. (1.20) and (1.21) dissapear, and after exchange of derivatives on the right-hand sides we finally obtain:

$$\left(\nabla^2 - \varepsilon\mu\frac{\partial^2}{\partial t^2}\right) \left\{ \begin{array}{c} \mathbf{E} \\ \mathbf{H} \end{array} \right\} = \mathbf{0}. \tag{1.22}$$

This type of equation is commonly called the wave equation because it represents a wave moving with phase velocity $v = 1/\sqrt{\varepsilon\mu}$ in the case of Eq. (1.22). When the solution of Eq. (1.22) can be expressed as a product of two functions, the first of them related only to space variables and the second being harmonic-time-dependent (more precisely $\mathbf{E}(\mathbf{r}, t) = \mathbf{E}_0(\mathbf{r})\exp(-\mathrm{i}\omega t)$ and $\mathbf{H}(\mathbf{r}, t) = \mathbf{H}_0(\mathbf{r})\exp(-\mathrm{i}\omega t)$, where ω is angular frequency), by plugging this form into Eq. (1.22), we obtain Helmholtz equation [35]:

$$\left(\nabla^2 + k^2\right) \left\{ \begin{array}{c} \mathbf{E} \\ \mathbf{H} \end{array} \right\} = \mathbf{0}, \tag{1.23}$$

where $k \equiv \sqrt{\varepsilon\mu\omega^2}$ is the magnitude of the wave vector.

1.3. Fourier transform of Maxwell's equations and the wave equation

When we perform a Fourier transform (see related part in Appendix A) on the differential form of Maxwell's equations and use the identities for Fourier transform of derivatives with respect to time and space variables (A9), we obtain the following transformed set of equations:

$$\mathrm{i}\mathbf{k} \cdot \mathbf{D}(\mathbf{k}, \omega) = \rho_\mathrm{F}(\mathbf{k}, \omega), \tag{1.24}$$

$$\mathrm{i}\mathbf{k} \cdot \mathbf{B}(\mathbf{k}, \omega) = 0, \tag{1.25}$$

$$\mathrm{i}\mathbf{k} \times \mathbf{E}(\mathbf{k}, \omega) = \mathrm{i}\omega\mathbf{B}(\mathbf{k}, \omega), \tag{1.26}$$

$$\mathrm{i}\mathbf{k} \times \mathbf{H}(\mathbf{k}, \omega) = \mathbf{J}_\mathrm{F}(\mathbf{k}, \omega) - \mathrm{i}\omega\mathbf{D}(\mathbf{k}, \omega). \tag{1.27}$$

Exploiting the properties of convolution (A10) and its definition (A11), the constitutive relations of Eqs. (1.5), (1.6) and the generalized Ohm's law (1.18) can be rewritten in $(\mathbf{k}, \omega)$ space as:

$$\mathbf{D}(\mathbf{k}, \omega) = \varepsilon(\mathbf{k}, \omega)\mathbf{E}(\mathbf{k}, \omega), \tag{1.28}$$

$$\mathbf{B}(\mathbf{k}, \omega) = \mu(\mathbf{k}, \omega)\mathbf{H}(\mathbf{k}, \omega), \tag{1.29}$$

$$\mathbf{J}(\mathbf{k}, \omega) = \sigma(\mathbf{k}, \omega)\mathbf{E}(\mathbf{k}, \omega). \tag{1.30}$$

The wave equation (1.22) can be transformed into form (for non-magnetic material with $\mu_\mathrm{r} = 1$)

$$\left(k^2 - \varepsilon_\mathrm{r}(\mathbf{k}, \omega)\frac{\omega^2}{c^2}\right) \left\{ \begin{array}{c} \mathbf{E}(\mathbf{k}, \omega) \\ \mathbf{H}(\mathbf{k}, \omega) \end{array} \right\} = \mathbf{0}, \tag{1.31}$$

where the equality for the speed of light in vacuum $c = 1/\sqrt{\varepsilon_0 \mu_0}$ was used. The expression for $\varepsilon_\mathrm{r}(\mathbf{k}, \omega)$ can be obtained when we substitute Eqs. (1.14), (1.16) and (1.10) into Eq. (1.30). Under the assumption of no magnetization and no free currents in the material, we obtain:

$$\varepsilon_\mathrm{r}(\mathbf{k}, \omega) = 1 + \mathrm{i}\frac{\sigma(\mathbf{k}, \omega)}{\omega\varepsilon_0}. \tag{1.32}$$

1.4. Poynting's theorem and energy of electromagnetic fields

The work done by the electromagnetic fields in a finite volume V can be expressed with use of Eq. (1.4) as [32]:

$$\iiint\limits_V \mathbf{J}_\mathrm{F} \cdot \mathbf{E} \, \mathrm{d}V = \iiint\limits_V \left[\mathbf{E} \cdot (\nabla \times \mathbf{H}) - \mathbf{E} \cdot \frac{\partial \mathbf{D}}{\partial t} \right] \mathrm{d}V. \tag{1.33}$$

After applying the equality $\nabla \cdot (\mathbf{E} \times \mathbf{H}) = \mathbf{H} \cdot (\nabla \times \mathbf{E}) - \mathbf{E} \cdot (\nabla \times \mathbf{H})$ and substituting of Faraday's law in Eq. (1.3), we modify Eq. (1.33) into the form

$$\iiint\limits_V \mathbf{J}_\mathrm{F} \cdot \mathbf{E} \, \mathrm{d}V = -\iiint\limits_V \left[\nabla \cdot (\mathbf{E} \times \mathbf{H}) + \mathbf{E} \cdot \frac{\partial \mathbf{D}}{\partial t} + \mathbf{H} \cdot \frac{\partial \mathbf{B}}{\partial t} \right] \mathrm{d}V. \tag{1.34}$$

We introduce now the density of total energy w:

$$w = \frac{1}{2}(\mathbf{E} \cdot \mathbf{D} + \mathbf{B} \cdot \mathbf{H}) \tag{1.35}$$

and Eq. (1.34) then becomes

$$-\iiint\limits_V \mathbf{J}_\mathrm{F} \cdot \mathbf{E} \mathrm{d}V = \iiint\limits_V \left[\nabla \cdot (\mathbf{E} \times \mathbf{H}) + \frac{\partial w}{\partial t} \right] \mathrm{d}V. \tag{1.36}$$

Eq. (1.36) can be written in the differential form as:

$$\frac{\partial w}{\partial t} + \nabla \cdot \mathbf{S} = -\mathbf{J}_\mathrm{F} \cdot \mathbf{E}. \tag{1.37}$$

The vector quantity $\mathbf{S} \equiv \mathbf{E} \times \mathbf{H}$ is called Poynting's vector and represents the energy flow. Equation (1.37) can be therefore understood as an energy conservation law.

1.5. Maxwell stress tensor

In the case of a particle with charge q moving with velocity $\mathbf{v}$ in an electromagnetic field, the Lorentz force

$$\mathbf{F}_{\mathrm{L}} = q(\mathbf{E} + \mathbf{v} \times \mathbf{B}), \tag{1.38}$$

will act on the particle. This relationship can be rewritten for the case of the vacuum environment as

$$\frac{\mathrm{d}\mathbf{p}_{\mathrm{mech}}}{\mathrm{d}t} = \iiint\limits_{V} (\rho\mathbf{E} + \mathbf{J} \times \mathbf{B})\mathrm{d}V = \iiint\limits_{V} \varepsilon_0 \left[\mathbf{E}(\nabla \cdot \mathbf{E}) + \mathbf{B} \times \frac{\partial \mathbf{E}}{\partial t} - c^2 \mathbf{B} \times (\nabla \times \mathbf{B}) \right] \mathrm{d}V, \tag{1.39}$$

where we substituted the relationships for ρ and $\mathbf{J}$, being $\mathbf{p}_{\mathrm{mech}}$ the mechanical momentum. To continue with the treatment of the integrand in Eq. (1.39), we add there $c^2\mathbf{B}(\nabla \cdot \mathbf{B})$ which is equal to zero [see Eq. (1.2)] and does not change the value of the integrand. Moreover we apply the equality

$$\mathbf{B} \times \frac{\partial \mathbf{E}}{\partial t} = -\frac{\partial}{\partial t}(\mathbf{E} \times \mathbf{B}) + \mathbf{E} \times \frac{\partial \mathbf{B}}{\partial t} = -\frac{\partial}{\partial t}(\mathbf{E} \times \mathbf{B}) - \mathbf{E} \times (\nabla \times \mathbf{E}), \tag{1.40}$$

and obtain

$$\frac{\mathrm{d}\mathbf{p}_{\mathrm{mech}}}{\mathrm{d}t} + \frac{\mathrm{d}}{\mathrm{d}t}\varepsilon_0 \iiint\limits_{V} (\mathbf{E}\times\mathbf{B})\mathrm{d}V = \varepsilon_0 \iiint\limits_{V} \left[\mathbf{E}(\nabla \cdot \mathbf{E}) - \mathbf{E} \times (\nabla \times \mathbf{E}) + c^2\mathbf{B}(\nabla \cdot \mathbf{B}) - c^2\mathbf{B} \times (\nabla \times \mathbf{B}) \right] \mathrm{d}V. \tag{1.41}$$

In the second term on the left-hand side we can recognize the Poynting's vector. Therefore Eq. (1.41) becomes

$$\frac{\mathrm{d}\mathbf{p}_{\mathrm{mech}}}{\mathrm{d}t} + \frac{1}{c^2}\frac{\mathrm{d}}{\mathrm{d}t} \iiint\limits_{V} \mathbf{S}\mathrm{d}V = \varepsilon_0 \iiint\limits_{V} \left[\mathbf{E}(\nabla \cdot \mathbf{E}) - \mathbf{E} \times (\nabla \times \mathbf{E}) + c^2\mathbf{B}(\nabla \cdot \mathbf{B}) - c^2\mathbf{B} \times (\nabla \times \mathbf{B}) \right] \mathrm{d}V. \tag{1.42}$$

As the volume integral containing Poynting's vector represents the momentum of the electromagnetic field, it should be possible to rewrite the integrand on the right hand side of (1.42) in terms of the divergence of some quantity and to transform the volume integral into a surface integral. The integrand is vectorial, therefore we have to introduce the divergence of a tensor of the second rank. This tensor dyadic is called Maxwell stress tensor and is defined as [32], [42]:

$$\overleftrightarrow{\mathbf{T}} = \varepsilon_0 \left(\mathbf{E}\mathbf{E} + c^2\mathbf{B}\mathbf{B} - \frac{1}{2}\overleftrightarrow{\mathbf{I}}(E^2 + c^2B^2) \right), \tag{1.43}$$

where $\overleftrightarrow{\mathbf{I}}$ is unit dyadic, or via its components

$$T_{ij} = \varepsilon_0 \left[E_i E_j + c^2 B_i B_j - \frac{1}{2}\delta_{ij}(E^2 + c^2B^2) \right]. \tag{1.44}$$

Now we can write the final form of Eq. (1.42):

$$\frac{\mathrm{d}}{\mathrm{d}t}(\mathbf{p}_{\text{mech}} + \mathbf{p}_{\text{field}}) = \iiint\limits_V \left(\rho\mathbf{E} + \frac{1}{c}\mathbf{J} \times \mathbf{B}\right)\mathrm{d}V + \frac{1}{c^2}\frac{\mathrm{d}}{\mathrm{d}t}\iiint\limits_V (\mathbf{E} \times \mathbf{H})\mathrm{d}V$$

$$= \iiint\limits_V \nabla \cdot \overleftrightarrow{\mathbf{T}}\mathrm{d}V = \oiint\limits_S \overleftrightarrow{\mathbf{T}} \cdot \mathbf{n}\mathrm{d}S, \tag{1.45}$$

where $\mathbf{n}$ is the unit vector oriented from interior to exterior of a closed surface S. Therefore $\overleftrightarrow{\mathbf{T}} \cdot \mathbf{n}$ is the normal flow of momentum per unit area outside of the volume enclosed by S.

1.6. Vector and scalar potentials

Now we will introduce potentials connected with the electric and magnetic fields. If we look at Eq. (1.2) and realize that the divergence of the curl of any vector is zero, we can introduce the vector potential $\mathbf{A}$ [32], [36]:

$$\mathbf{B} = \nabla \times \mathbf{A}. \tag{1.46}$$

We can continue by substituting Eq. (1.46) into Eq. (1.3):

$$\nabla \times \left(\mathbf{E} + \frac{\partial \mathbf{A}}{\partial t}\right) = 0. \tag{1.47}$$

There is another identity which says that the curl of the gradient of any scalar function vanishes, therefore we can define a scalar potential Φ that fulfills:

$$\mathbf{E} + \frac{\partial \mathbf{A}}{\partial t} = -\nabla\Phi. \tag{1.48}$$

If we apply $\nabla\cdot$ to Eq. (1.48), we can write it as

$$\nabla^2\Phi + \frac{\partial}{\partial t}(\nabla \cdot \mathbf{A}) = -\frac{\rho}{\varepsilon_0}. \tag{1.49}$$

Now we express Eq. (1.4) by means of the potentials:

$$\nabla^2\mathbf{A} - \frac{1}{c^2}\frac{\partial^2 \mathbf{A}}{\partial t^2} - \nabla\left(\nabla \cdot \mathbf{A} + \frac{1}{c^2}\frac{\partial \Phi}{\partial t}\right) = -\mu_0\mathbf{J}. \tag{1.50}$$

To continue with the treatment of Eqs. (1.49) and (1.50), we realize that the definition of vector potential in Eq. (1.46) allows us to add there the gradient of some scalar function Λ without changing $\mathbf{B}$. The scalar potential must be then transformed, too. Explicitly:

$$\mathbf{A} \to \mathbf{A}' = \mathbf{A} + \nabla\Lambda, \qquad \Phi \to \Phi' = \Phi - \frac{\partial \Lambda}{\partial t}. \tag{1.51}$$

This property enables us to choose a set of potentials satisfying the Lorenz calibration condition

$$\nabla \cdot \mathbf{A} + \frac{1}{c^2}\frac{\partial \Phi}{\partial t} = 0 \tag{1.52}$$

and to obtain two inhomogeneous wave equations for the potentials

$$\nabla^2\Phi - \frac{1}{c^2}\frac{\partial^2\Phi}{\partial t^2} = -\frac{\rho}{\varepsilon_0}, \qquad \nabla^2\mathbf{A} - \frac{1}{c^2}\frac{\partial^2\mathbf{A}}{\partial t^2} = -\mu_0\mathbf{J}. \tag{1.53}$$

If there is no change of magnetic field with time, the time derivative of the vector potential divergence in Eq. (1.49) vanishes and we obtain Poisson's equation, which is often used for computations of electrostatic problems

$$\nabla^2\Phi = -\frac{\rho}{\varepsilon_0}. \tag{1.54}$$

It is sometimes convenient to have Eq. (1.53) expressed in terms of free sources. In a non-magnetic material ($\mu_{\mathrm{r}} = 1$), Eq. (1.53) becomes

$$\nabla^2\Phi - \varepsilon_{\mathrm{r}}\frac{1}{c^2}\frac{\partial^2\Phi}{\partial t^2} = -\frac{\rho_{\mathrm{F}}}{\varepsilon}, \qquad \nabla^2\mathbf{A} - \varepsilon_{\mathrm{r}}\frac{1}{c^2}\frac{\partial^2\mathbf{A}}{\partial t^2} = -\mu_0\mathbf{J}_{\mathrm{F}}. \tag{1.55}$$

If we perform the transformation of Eq. (1.55) to Fourier space, we obtain:

$$\left[k^2 - \frac{\omega^2}{c^2}\varepsilon_{\mathrm{r}}(\omega)\right]\Phi(\mathbf{k},\omega) = \frac{\rho_{\mathrm{F}}}{\varepsilon(\omega)}, \qquad \left[k^2 - \frac{\omega^2}{c^2}\varepsilon_{\mathrm{r}}(\omega)\right]\mathbf{A}(\mathbf{k},\omega) = \mu_0\mathbf{J}_{\mathrm{F}}(\mathbf{k},\omega). \tag{1.56}$$

The scalar and vector potentials are very useful in dealing with problems related to the electromagnetic fields. In the following chapters we are going to use them to find the fields produced by fast electrons and we also exploit them in calculations of electron energy loss.

2. Electron energy loss spectroscopy

In this chapter, we are going to provide a brief introduction to electron energy loss spectroscopy. For this purpose we perform the computation of the field produced by moving relativistic electrons and then we present the classical dielectric formalism used for analysing of the electron energy loss spectra. In the following sections, we also introduce energy loss probabilities for bulk, surface and localized plasmon excitations.

2.1. Field of a moving electron

The moving electron can be treated as a charge density $\rho(\mathbf{r}, t)$ localized in space

$$\rho(\mathbf{r}, t) = -e\delta(\mathbf{r} - \mathbf{r}_0 - \mathbf{v}t), \tag{2.1}$$

where e stands for the elementary charge of the electron, $\mathbf{r}$ is the position vector, $\mathbf{r}_0$ is the vector of reference position of the electron, $\mathbf{v}$ is the velocity of the particle and t is the time elapsed from the beginning of the movement. Therefore we can mark $\mathbf{r}_t = \mathbf{r}_0 + \mathbf{v}t$ as the current position of the particle with respect to the origin. We can also calculate the charge density in Fourier space, where we exploit the properties of the delta distribution:

$$\rho(\mathbf{k}, \omega) = -e(2\pi)^3 \exp\left(i\frac{\omega \mathbf{r}_0 \cdot \mathbf{v}}{v^2}\right) \delta(\omega - \mathbf{k} \cdot \mathbf{v}). \tag{2.2}$$

The previous expression of the the charge density in Eq. (2.2) is useful when we substitute it into transformed wave equations for the electromagnetic potentials according to Eq. (1.56). Then in Fourier space we obtain [22],[32]:

$$\Phi(\mathbf{k}, \omega) = \frac{-e(2\pi)^3}{\varepsilon(\omega)} \frac{\exp\left(i\frac{\omega \mathbf{r}_0 \cdot \mathbf{v}}{v^2}\right) \delta(\omega - \mathbf{k} \cdot \mathbf{v})}{k^2 - \frac{\omega^2}{c^2}\varepsilon_r(\omega)} \qquad \text{and} \qquad \mathbf{A}(\mathbf{k}, \omega) = \varepsilon_r(\omega)\frac{\mathbf{v}}{c^2}\Phi(\mathbf{k}, \omega). \tag{2.3}$$

From Eq. (2.3) it is easy to express the electric and magnetic fields [with knowledge of Eqs. (1.46) and (1.48)]:

$$\mathbf{E}(\mathbf{k}, \omega) = i\left[\frac{\omega \varepsilon_r(\omega)}{c}\frac{\mathbf{v}}{c} - \mathbf{k}\right]\Phi(\mathbf{k}, \omega) \qquad \text{and} \qquad \mathbf{B}(\mathbf{k}, \omega) = i\varepsilon_r(\omega)\mathbf{k} \times \frac{\mathbf{v}}{c^2}\Phi(\mathbf{k}, \omega). \tag{2.4}$$

To obtain the electric field in real space, we will continue with the inverse Fourier transformation according to

$$\mathbf{E}(\mathbf{r}, \omega) = \frac{1}{(2\pi)^3} \iiint \mathbf{E}(\mathbf{k}, \omega)\exp(i\mathbf{k} \cdot \mathbf{r})\mathrm{d}^3k. \tag{2.5}$$

We expect an electron moving in positive z direction parallel to the axis, therefore we consider $\mathbf{v} = (0, 0, v)$, we choose the observation point $\mathbf{r} = (0, y, 0)$ (i.e. the point in which we want to calculate the fields) and the initial position of the electron $\mathbf{r}_0 = (x_0, y_0, -z_0)$. Eq. (2.5) is then simplified when it is written in its Cartesian components E_1, E_2 and E_3:

$$E_1(\omega) = \frac{ie \exp\left(-i\omega\frac{z_0}{v}\right)}{\varepsilon(\omega)v} \iiint\limits_{-\infty}^{\infty} \frac{k_1 \exp(ik_2 y)\delta\left(k_3 - \frac{\omega}{v}\right)}{k^2 - \frac{\omega^2}{c^2}\varepsilon_r(\omega)} \mathrm{d}k_1 \mathrm{d}k_2 \mathrm{d}k_3, \tag{2.6}$$

$$E_2(\omega) = \frac{ie \exp\left(-i\omega\frac{z_0}{v}\right)}{\varepsilon(\omega)v} \iiint\limits_{-\infty}^{\infty} \frac{k_2 \exp(ik_2 y)\delta\left(k_3 - \frac{\omega}{v}\right)}{k^2 - \frac{\omega^2}{c^2}\varepsilon_r(\omega)} \mathrm{d}k_1 \mathrm{d}k_2 \mathrm{d}k_3, \tag{2.7}$$

$$E_3(\omega) = -\frac{ie \exp\left(-i\omega\frac{z_0}{v}\right)}{\varepsilon(\omega)v} \iiint\limits_{-\infty}^{\infty} \left[\frac{\omega\varepsilon_r(\omega)v}{c^2} - k_3\right] \frac{\exp(ik_2 y)\delta\left(k_3 - \frac{\omega}{v}\right)}{k^2 - \frac{\omega^2}{c^2}\varepsilon_r(\omega)} \mathrm{d}k_1 \mathrm{d}k_2 \mathrm{d}k_3, \tag{2.8}$$

where we introduced the Cartesian components of the wave vector $\mathbf{k} = (k_1, k_2, k_3)$ and the electric field $\mathbf{E} = (E_1, E_2, E_3)$. The integration over k_3 can be done easily, obtaining

$$E_1(\omega) = \frac{ie \exp\left(-i\omega\frac{z_0}{v}\right)}{\varepsilon(\omega)v} \iint\limits_{-\infty}^{\infty} \frac{k_1 \exp(ik_2 y)}{k_1^2 + k_2^2 + \lambda^2} \mathrm{d}k_1 \mathrm{d}k_2, \tag{2.9}$$

$$E_2(\omega) = \frac{ie \exp\left(-i\omega\frac{z_0}{v}\right)}{\varepsilon(\omega)v} \iint\limits_{-\infty}^{\infty} \frac{k_2 \exp(ik_2 y)}{k_1^2 + k_2^2 + \lambda^2} \mathrm{d}k_1 \mathrm{d}k_2, \tag{2.10}$$

$$E_3(\omega) = -\frac{ie \exp\left(-i\omega\frac{z_0}{v}\right)}{\varepsilon(\omega)v} \iint\limits_{-\infty}^{\infty} \left[\frac{\omega\varepsilon_r(\omega)v}{c^2} - \frac{\omega}{v}\right] \frac{\exp(ik_2 y)}{k_1^2 + k_2^2 + \lambda^2} \mathrm{d}k_1 \mathrm{d}k_2, \tag{2.11}$$

with use of

$$\lambda^2 = \frac{\omega^2}{v^2} - \frac{\omega^2\varepsilon_r(\omega)}{c^2} = \frac{\omega^2}{v^2}[1 - \beta^2\varepsilon_r(\omega)], \tag{2.12}$$

where $\beta = v/c$.

We can also recognize that after integration over k_1, E_1 vanishes as the integrand is an odd function. For further simplification we apply

$$\int\limits_{-\infty}^{\infty} \frac{1}{k_1^2 + k_2^2 + \lambda^2} \mathrm{d}k_1 = \frac{\pi}{\sqrt{k_2^2 + \lambda^2}}, \tag{2.13}$$

and expressions for E_2 and E_3 become

$$E_2(\omega) = \frac{ie\pi \exp\left(-i\omega\frac{z_0}{v}\right)}{\varepsilon(\omega)v} \int\limits_{-\infty}^{\infty} \frac{k_2 \exp(ik_2 y)}{\sqrt{k_2^2 + \lambda^2}} \mathrm{d}k_2, \tag{2.14}$$

$$E_3(\omega) = -\frac{ie\pi \exp\left(-i\omega\frac{z_0}{v}\right)}{\varepsilon(\omega)v} \int\limits_{-\infty}^{\infty} \left[\frac{\omega\varepsilon_r(\omega)v}{c^2} - \frac{\omega}{v}\right] \frac{\exp(ik_2 y)}{\sqrt{k_2^2 + \lambda^2}} \mathrm{d}k_2. \tag{2.15}$$

First we solve Eq. (2.15) realizing that there appears a representation of a modified Bessel function of the second kind according to the relationship [4]

$$K_\nu(xz) = \frac{\Gamma(\nu + \frac{1}{2})(2z)^\nu}{\sqrt{\pi}x^\nu} \int\limits_0^\infty \frac{\cos(xt)\mathrm{d}t}{(t^2 + z^2)^{\nu + \frac{1}{2}}}, \tag{2.16}$$

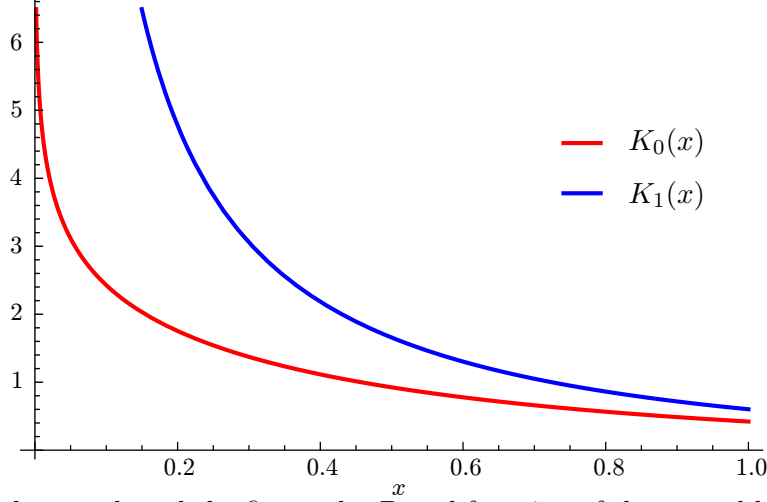Figure 2.1: Plot of the zeroth and the first order Bessel function of the second kind. Both functions are divergent for $x \to 0$.

where $\Gamma(x)$ is Euler gamma function and $\nu = 0$ in the case of Eq. (2.15). The Bessel functions of the second kind corresponding to the zeroth and the first order are plotted in figure 2.1. With use of the former expression we obtain:

$$
\begin{aligned}
E_3(\omega) &= -\frac{\mathrm{i}e2\pi \exp\left(-\mathrm{i}\omega\frac{z_0}{v}\right)}{\varepsilon(\omega)v} \left[\frac{\omega\varepsilon_\mathrm{r}(\omega)v}{c^2} - \frac{\omega}{v}\right] K_0(\lambda y) \\
&= \frac{\mathrm{i}e2\pi \exp\left(-\mathrm{i}\omega\frac{z_0}{v}\right)\omega}{\varepsilon(\omega)v^2} \left[1 - \varepsilon_\mathrm{r}(\omega)\beta^2\right] K_0(\lambda y).
\end{aligned}
\tag{2.17}
$$

Now we have to deal with Eq. (2.14). We see that integrand is similar to the previous case except for an additional k_2. Here we exploit the relationship $K_0'(z) = -K_1(z)$ [4] and change the order of integration and differentiation, obtaining:

$$
\begin{aligned}
E_2(\omega) &= \frac{\mathrm{i}e\pi \exp\left(-\mathrm{i}\omega\frac{z_0}{v}\right)}{\varepsilon(\omega)v} \int\limits_{-\infty}^\infty \frac{\mathrm{d}}{\mathrm{d}y}\left(\frac{\exp(\mathrm{i}k_2 y)}{\mathrm{i}\sqrt{k_2^2 + \lambda^2}}\right) \mathrm{d}k_2 \\
&= \frac{e2\pi \exp\left(-\mathrm{i}\omega\frac{z_0}{v}\right)}{\varepsilon(\omega)v} \frac{\mathrm{d}}{\mathrm{d}y}\left(\int\limits_0^\infty \frac{\cos(k_2 y)}{\sqrt{k_2^2 + \lambda^2}}\mathrm{d}k_2\right) \\
&= \frac{-e2\pi \exp\left(-\mathrm{i}\omega\frac{z_0}{v}\right)\lambda}{\varepsilon(\omega)v} K_1(\lambda y).
\end{aligned}
\tag{2.18}
$$

To compute the magnetic field, it is possible to use Eq. (2.3). We see that there can appear B_1 or B_2 (with our choice of velocity vector), but during integration only B_1 remains:

15

$$B_1(\omega) = \frac{-iev\exp\left(-i\omega\frac{z_0}{v}\right)}{c^2\varepsilon_0} \iiint\limits_{-\infty}^{\infty} \frac{k_2 v\exp(ik_2 y)\delta(\omega - k_3 v)}{k^2 - \frac{\omega^2}{c^2}\varepsilon(\omega)} dk_1 dk_2 dk_3$$

$$= \frac{-iev\exp\left(-i\omega\frac{z_0}{v}\right)}{c^2\varepsilon_0} \iint\limits_{-\infty}^{\infty} \frac{k_2\exp(ik_2 y)}{k_1^2 + k_2^2 + \lambda^2} dk_1 dk_2$$

$$= \frac{-iev\pi\exp\left(-i\omega\frac{z_0}{v}\right)}{c^2\varepsilon_0} \int\limits_{-\infty}^{\infty} \frac{k_2\exp(ik_2 y)}{\sqrt{k_2^2 + \lambda^2}} dk_2$$

$$= \frac{ev2\pi\lambda}{c^2\varepsilon_0}\exp\left(-i\omega\frac{z_0}{v}\right) K_1(\lambda y).$$

(2.19)

The results for the fields that we have obtained could be naturally expressed by employing cylindrical coordinates. If the electron's trajectory follows the z axis [i.e. $(x_0, y_0) = (0,0)$], in a cylindrical coordinate system there exists an electric field given by the radial component and the component parallel to the z axis [$\mathbf{E}(\mathbf{r}) = (E_R, 0, E_z)$] and a magnetic field with one component which is the azimuthal component [$\mathbf{H}(\mathbf{r}) = (0, H_\phi, 0)$]. This holds except for the points along the trajectory of the electron, for which a singularity appears as can be observed in figure 2.1.

2.2. Classical dielectric formalism

In the previous section, we obtained the expressions for the electric and magnetic fields produced by fast electrons in infinite space. These fields give us the first insight into our problem.

Calculations of the electric and magnetic fields in realistic geometries are much more complex because in cases of our interest, the electron can move near targets with different shapes and composition. When passing close to or through matter, the fields produced by the electron polarize matter, producing "induced" fields $\mathbf{E}^{ind}$ that act back on the electron causing its energy loss, which can be treated with help of classical electrodynamics. This so-called dielectric approach was probably for the first time used by Fermi [17] in the content of charges interacting with matter, who calculated stopping power for fast charges moving in different materials.

The problem of energy loss can also be understood in a different way. From the point of view of the electrons of the target, the field produced by the moving electron can be treated as a perturbation which can cause transitions from occupied to unoccupied levels. In other words, electrons of the target gain energy and momentum to the detriment of the probe.

Using the first approach, the total energy loss ΔE can be computed by integrating the scalar product of the force stopping the electron and its unit trajectory [22], [48]

$$\Delta E = e \int\limits_{-\infty}^{\infty} \mathbf{E}_{ind}(\mathbf{r}', t) \cdot \frac{d\mathbf{r}'}{dt} dt = e \int\limits_{-\infty}^{\infty} \mathbf{v} \cdot \mathbf{E}_{ind}(\mathbf{r}', t) dt.$$

(2.20)

Employing the Rayleigh-Parseval theorem (A14) to deal with a real function, we can express the energy loss as [22]:

$$\Delta E = \int\limits_{0}^{\infty} \hbar\omega\Gamma_{EELS}(\omega)d\omega,$$

(2.21)

where

$$\Gamma_{\text{EELS}}(\omega) = \frac{e}{\pi\hbar\omega} \int\limits_{-\infty}^{\infty} \text{Re}\left[\mathbf{v}\cdot\mathbf{E}^{\text{ind}}(\mathbf{r}',\omega)\exp(-\mathrm{i}\omega t)\right] \mathrm{d}t \tag{2.22}$$

is the so-called electron energy loss probability which can be directly measured in EELS experiments and where $\hbar$ is the reduced Planck's constant. We thus only need to compute the induced field acting back on the electron. This has been done for many different geometries in a variety of situations, e.g. for electrons going parallel or perpendicular to infinite planar interfaces, penetrating thin films or passing near isolated or supported particles of different shapes. An overview can be found in references [22] or [49]. There were also various approaches dealing with dispersive media or relativistic descriptions, which is needed for accurate computations. These corrections can play an important role especially in cases of high initial energies of electrons, bigger targets and when the trajectories of electrons are very close to the targets.

2.3. Bulk loss probability

When we consider a relativistic electron moving in bulk material, the loss probability can be expressed as [22]:

$$\Gamma_{\text{bulk}}(\omega) = \frac{e^2 L}{\pi\hbar v^2}\text{Im}\left\{\left(\frac{v^2}{c^2} - \frac{1}{\varepsilon_{\text{r}}(\omega)}\right)\ln\left(\frac{q_{\text{c}} - (\omega/c)^2\varepsilon_{\text{r}}(\omega)}{(\omega/v)^2 - (\omega/c)^2\varepsilon_{\text{r}}(\omega)}\right)\right\}, \tag{2.23}$$

where L is length of trajectory that electron passed through material and where we assumed a local response represented by $\varepsilon_{\text{r}}(\omega)$ (independent of the wave vector). This result also contains the so-called cutoff q_{c}, which is included because of the momentum conservation law and is connected with the experimental setup, where this cutoff is given by the aperture of the microscope spectrometer (ϕ_{out} is the half-aperture collection angle):

$$\hbar q_{\text{c}} \approx \sqrt{(m_{\text{e}}v\phi_{\text{out}})^2 + (\hbar\omega v)^2}. \tag{2.24}$$

The retarded bulk loss probability in Eq. (2.23) can be easily modified to obtain the nonretarded equation by considering $c \to \infty$, as

$$\Gamma_{\text{bulk}}^{\text{NR}}(\omega) = \frac{2e^2 L}{\pi\hbar v^2}\text{Im}\left\{-\frac{1}{\varepsilon_{\text{r}}(\omega)}\right\}\ln(q_{\text{c}}v/\omega). \tag{2.25}$$

From Eq. (2.25) we can directly see that probability will be large around the maximum of $\text{Im}\{-1/\varepsilon_{\text{r}}\}$. If we assume a Drude-like response ε_{r} to describe the local response of a metal with plasma frequency ω_{p} (see Appendix B), we find out that the peak of bulk loss is given at $\omega = \omega_{\text{p}}$, which is the eigenfrequency of bulk plasma oscillations. The position of the peak will be slightly modified by the logarithm dependence. The bulk loss probability per unit path length calculated for an electron of energy $120\,\text{keV}$ travelling in aluminium is plotted by the red dashed line in figure 2.2.

2.4. Surface modes

The case of an electron moving along or penetrating a planar surface also deserves attention, because of the possible excitations of surface modes [37], [15].

When an electron is travelling in vacuum parallel to an interface with medium characterized by a dielectric function $\varepsilon_{\mathrm{r}}(\omega)$, at constant distance b, the loss probability within a nonretarded approximation is found to be [26]:

$$\Gamma_{\mathrm{planar}}^{\mathrm{NR}}(\omega) = \frac{4e^2 L}{\pi \hbar v^2} K_0 \left(\frac{2\omega b}{v} \right) \mathrm{Im} \left[-\frac{1}{1 + \varepsilon_{\mathrm{r}}(\omega)} \right]. \tag{2.26}$$

We can consider the more general situation of an electron moving in a medium with dielectric function $\varepsilon_{\mathrm{r,A}}(\omega)$ parallel to the interface with another material described by $\varepsilon_{\mathrm{r,B}}(\omega)$. We obtain in this case [26]:

$$\Gamma_{\mathrm{planar}}^{\mathrm{NR}}(\omega) = \frac{2e^2 L}{\pi \hbar v^2} \left\{ \ln \left(\frac{q_c v}{\omega} \right) \mathrm{Im} \left[-\frac{1}{\varepsilon_{\mathrm{r,A}}} \right] + K_0 \left(\frac{2\omega b}{v} \right) \left[\mathrm{Im} \left[-\frac{2}{\varepsilon_{\mathrm{r,A}} + \varepsilon_{\mathrm{r,B}}} \right] - \mathrm{Im} \left[-\frac{1}{\varepsilon_{\mathrm{r,A}}} \right] \right] \right\}. \tag{2.27}$$

The first term in the curly brackets is nothing but bulk loss corresponding to the media where electron is moving, while the second term is related to the interface. We can recognize there a modification of Eq. (2.26) and an additional term, which is responsible for the so-called "Begrenzungs-Effekt" (due to the excitation of surface modes, bulk oscillations are reduced). This can be clearly resolved in figure 2.2, where we plot the direct bulk term and the second "surface" term (marked as $\Gamma_{\mathrm{Begrenzungs}}/L$) separately for the case of an electron travelling in aluminium near the interface with vacuum. In the plot two peaks can be seen: the first one situated very close to a value of $\hbar\omega_{\mathrm{p}}/\sqrt{2}$ corresponds to the surface plasmon excited at the aluminium-vacuum interface, while the second one with approximate energy of $\hbar\omega_{\mathrm{p}}$ is related to the bulk plasmon, as we saw in previous section. If we reduced the distance of electron's trajectory from the interface, we would observe an increase of the surface peak intensity at the expense of the bulk peak.
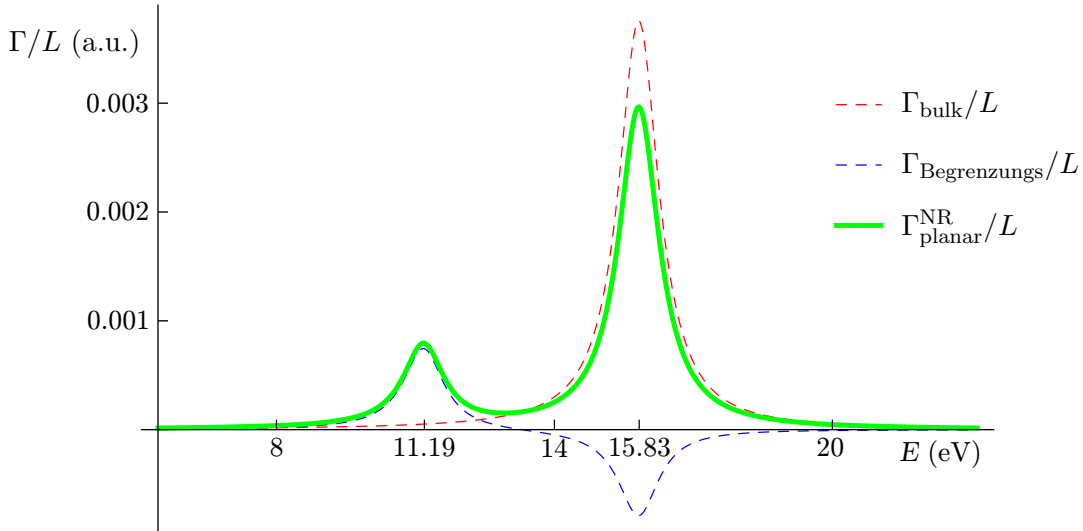

Figure 2.2: Energy loss probability per unit path length Γ/L with a split of the terms contained in Eq. (2.27))(Γ is expressed in atomic units, where $e = m_{\mathrm{e}} = \hbar = 1$). Γ_{bulk}/L represents the first term in the curly brackets (red dashed line), $\Gamma_{\mathrm{Begrenzungs}}/L$ is related to the second term (blue dashed line) and the total loss probability per unit length is denoted as $\Gamma_{\mathrm{planar}}^{\mathrm{NR}}/L$ (green solid line). This plot corresponds to an electron of energy $120\,\mathrm{keV}$ travelling in aluminium at a distance $b = 2\,\mathrm{nm}$ from the interface. $\varepsilon_{\mathrm{r,A}}(\omega)$ is represented by a Drude dielectric function with parameters from table B.1, $\varepsilon_{\mathrm{r,B}} = 1$ is taken to be vacuum and we considered a cutoff $q_{\mathrm{c}} = 0.4\,\mathrm{a.u.}$

2.5. Localized modes

From the experimental point of view, both bulk and surface losses are important, because we can utilize them to determine properties of our sample and its composition. However, in reality materials can show a more complex structure and samples can consist of many components or can have various shapes. If we deal with the metallic particles, we can observe excitation of so-called localized plasmon modes that represent natural oscillations of electron gas localized at the object.

Small particles can be of different shapes, but the spherical geometry provides a good canonical example. The complete nonretarded solution including possibility of higher-order mode excitation was firstly published by Ferrell and Echenique [18]. After solving Poisson's equation and matching boundary conditions with the Fourier components of the fields, they were able to calculate the induced field and obtained the following expression for the energy loss probability:

$$\Gamma_{\text{EELS}}^{\text{NR}}(\omega) = \frac{4e^2}{\pi\hbar v^2} \sum_{n=1}^{\infty} \sum_{m=-n}^{n} \frac{(\omega/v)^{2n}}{(n-m)!(n+m)!} K_m^2\left(\frac{\omega b}{v}\right) \text{Im}\left[a^{2n+1}\frac{n\varepsilon_{\text{r}}(\omega)-n}{n\varepsilon_{\text{r}}(\omega)+n+1}\right], \qquad (2.28)$$

which holds for sphere situated in vacuum and where we assume $v/c \ll 1$ and $ka \ll 1$. b is the distance of the electron trajectory from the centre of the sphere with radius a and dielectric function $\varepsilon_{\text{r}}(\omega)$. The expression in square brackets is the nonretarded multipolar polarizability. For the case $\omega a/v \ll 1$ the most significant contribution comes from $n=1$ term and we can then use the dipole approximation:

$$\Gamma_{\text{EELS}}^{\text{NR,dip}}(\omega) = \frac{4e^2\omega^2}{\pi\hbar v^4}\text{Im}\left[a^3\frac{\varepsilon_{\text{r}}(\omega)-1}{\varepsilon_{\text{r}}(\omega)+2}\right]\left[K_0^2\left(\frac{\omega b}{v}\right) + K_1^2\left(\frac{\omega b}{v}\right)\right]. \qquad (2.29)$$

In figure 2.3, the loss probability calculated according to Eq. (2.28) is plotted for a small silver sphere with radius $a = 1\,\text{nm}$ and electrons of energy $120\,\text{keV}$ passing at an impact parameter $b = 1.5\,\text{nm}$. As the sphere is very small, the nonretarded approximation should work well in this case. We also labelled the position of the first four peaks corresponding to modes $n = 1-4$ that can be identified easily. If we plotted the energy loss probability within the dipole approximation, only the first peak would appear.
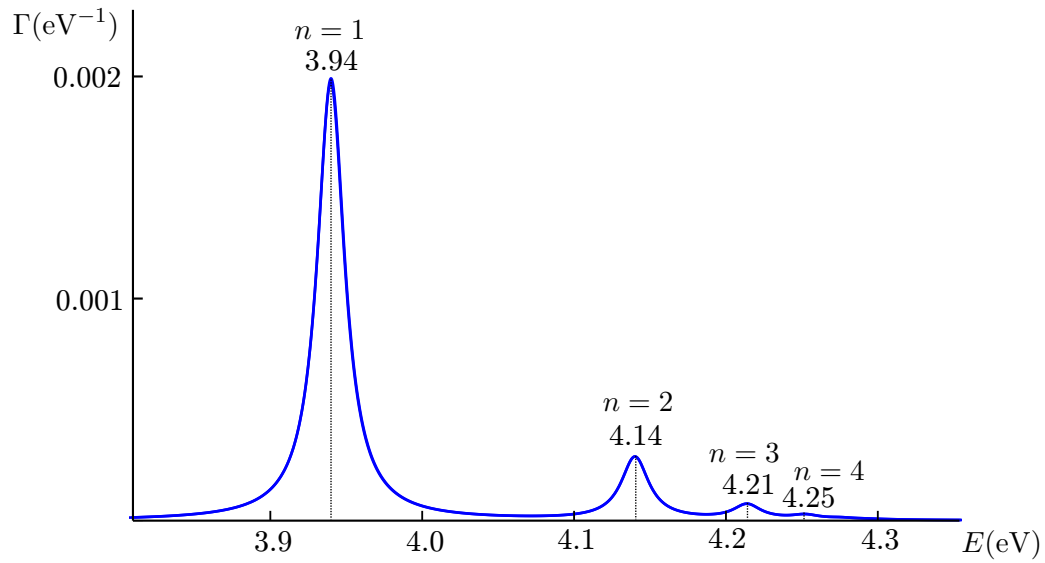
Figure 2.3: Electron energy loss probability per unit energy Γ obtained for a silver sphere of radius $a = 1\,\text{nm}$, impact parameter $b = 1.5\,\text{nm}$, measured from the centre of the sphere, and energy of electrons of $120\,\text{keV}$. Silver was modelled by a Drude dielectric function defined in Appendix B with parameters from table B.1. Energies of peaks related to the first four modes are marked.

3. Numerical approaches

There exist a few numerical approaches enabling us to calculate the response of an arbitrarily shaped structure to an external field. We mention here three main methods that can be used for electron energy loss calculations – the boundary element method (BEM), the discrete dipole approximation (DDA) and the finite-difference in time-domain (FDTD) approach.

3.1. Boundary element method

The boundary element (or charge) method is widely used in electron energy loss spectroscopy as we can incorporate there naturally the fields produced by moving electrons represented by its vector and scalar potentials [24]. This approach can be used in the nonretarded limit, where Poisson's equation [23] is solved numerically, or a full-retarded computation can be also performed using the whole set of Maxwell's equations [25].

   The core of this method consists in solving self-consistently the surface integrals involving charges and currents, situated on the arbitrarily shaped interface between different dielectrics, for a given external source. To introduce the non-retarded approach, we will start with the wave equations for scalar and vector potentials in Eq. (1.53), which represent the set of Maxwell's equations. If we consider these equations in ω-space, for nonmagnetic materials we obtain

$$(\nabla^2 + k^2\varepsilon_{\mathrm{r}})\Phi = -(\rho_{\mathrm{F}}/\varepsilon + \mathbf{D}\cdot\nabla\frac{1}{\varepsilon_{\mathrm{r}}}), \qquad (\nabla^2 + k^2\varepsilon_{\mathrm{r}})\mathbf{A} = -\mu_0(\mathbf{J}_{\mathrm{F}} - \mathrm{i}\omega\Phi\nabla\varepsilon), \tag{3.1}$$

where in addition to the terms corresponding to external charges and currents, other contributions related to the gradient of the dielectric function appear. As the discontinuity of the dielectric function appears at the interface between two media, these terms are nonzero only at the interface and represent additional boundary surface charges and currents. However, they can not be related to real interface charges and currents in a general case [25].
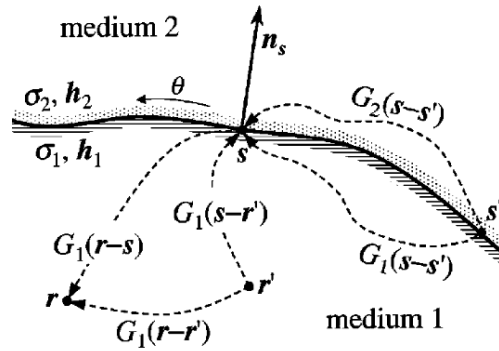

Figure 3.1: Geometric representation of an arbitrarily shaped interface separating medium 1 and 2. Scheme reproduced from [25].

   If we adopt the geometry, which is depicted in figure 3.1 [25], we can employ the Green's function $G_j = \exp(\mathrm{i}k_j r)/r$ of the wave equation (see Appendix A) to write the solutions of Eq. (3.1) that vanish at infinity as

$$\left\{ \begin{array}{c} \Phi(\mathbf{r}) \\ \mathbf{A}(\mathbf{r}) \end{array} \right\} = \int \mathrm{d}\mathbf{r}' G_j(|\mathbf{r}-\mathbf{r}'|) \left\{ \begin{array}{c} \rho_{\mathrm{F}}(\mathbf{r}')/\varepsilon_j \\ \mu_0\mathbf{J}_{\mathrm{F}}(\mathbf{r}') \end{array} \right\} + \int \mathrm{d}\mathbf{s} G_j(|\mathbf{r}-\mathbf{s}|) \left\{ \begin{array}{c} \sigma_j(\mathbf{s}) \\ \mathbf{h}_j(\mathbf{s}) \end{array} \right\}. \tag{3.2}$$

When we examine the form of Eq. (3.2), we find out that the first integral on the right-hand side represents the solutions everywhere in the space except at the interface. At the interface, the second integral becomes important since it both compensates the discontinuity of the Green's function and includes the effects of boundary charges σ_j and currents $\mathbf{h}_j$. We then apply boundary conditions requiring continuity of potentials at the interfaces between two media ($j = 1$ and $j = 2$) and obtain

$$G_1\sigma_1 - G_2\sigma_2 = -(\Phi_1^\mathrm{e} - \Phi_2^\mathrm{e}) \qquad \text{and} \qquad G_1\mathbf{h}_1 - G_2\mathbf{h}_2 = -(\mathbf{A}_1^\mathrm{e} - \mathbf{A}_2^\mathrm{e}), \tag{3.3}$$

where equivalent boundary sources read

$$\Phi_j^\mathrm{e}(\mathbf{s}) = \frac{1}{\varepsilon_j} \int \mathrm{d}\mathbf{r}' G_j(|\mathbf{s} - \mathbf{r}'|)\rho_\mathrm{F}(\mathbf{r}') \tag{3.4}$$

and

$$\mathbf{A}_j^\mathrm{e}(\mathbf{s}) = \mu_0 \int \mathrm{d}\mathbf{r}' G_j(|\mathbf{s} - \mathbf{r}'|)\mathbf{J}_\mathrm{F}(\mathbf{r}'). \tag{3.5}$$

Now we employ the condition of continuity of both the normal derivative of the tangential vector potential and the tangential derivatives of all components of the vector potential, which holds for nonmagnetic material. This leads to another set of equations:

$$H_1\mathbf{h}_1 - H_2\mathbf{h}_2 - \mathrm{i}k\mathbf{n}_s(G_1\varepsilon_1\sigma_1 - G_2\varepsilon_2\sigma_2) = \alpha, \tag{3.6}$$

$$H_1\varepsilon_1\sigma_1 - H_2\varepsilon_2\sigma_2 - \mathrm{i}k\mathbf{n}_s \cdot (G_1\varepsilon_1\mathbf{h}_1 - G_2\varepsilon_2\mathbf{h}_2) = D^\mathrm{e}, \tag{3.7}$$

where H_j is the normal derivative of G_j and

$$\alpha = (\mathbf{n}_s \cdot \nabla_\mathbf{s})(\mathbf{A}_2^\mathrm{e} - \mathbf{A}_1^\mathrm{e}) + \mathrm{i}k\mathbf{n}_s(\varepsilon_1\Phi_1^\mathrm{e} - \varepsilon_2\Phi_2^\mathrm{e}), \tag{3.8}$$

$$D^\mathrm{e} = \mathbf{n}_s \cdot [\varepsilon_1(\mathrm{i}k\mathbf{A}_1^\mathrm{e} - \nabla_\mathbf{s}\Phi_1^\mathrm{e}) - \varepsilon_2(\mathrm{i}k\mathbf{A}_2^\mathrm{e} - \nabla_\mathbf{s}\Phi_2^\mathrm{e})]. \tag{3.9}$$

We can see that D^e has the meaning of the difference of the normal displacement, which would be induced by the external source at the position of the interface in the case of a homogeneous space filled either with medium $j = 1$ or $j = 2$ [25].

From these four boundary conditions, four unknown quantities – auxiliary boundary charges and currents – can be calculated and then used for evaluation of potentials. This leads to the problem of solving a system of eight linear surface-integral equations. If we want to solve it numerically, the next step consists of discretizing the surface integral in N points to obtain a set of $8N$ linear equations.

Comparison of experimental EEL spectra with data obtained from BEM simulation can be found in figure 3.2. It is apparent that numerically calculated spectra do not overlap perfectly with experiments, where we have to deal with shape irregularities of measured particles and constraints given by the resolution of the experimental technique. However, with this approach we can nicely reproduce the energies of the main peaks and reveal possible modes that can be excited.

In the following chapter, MNPBEM toolbox will be used for comparison with analytically computed fields, particularly the implementation for EELS calculations [31],[30]. This toolbox is used within the MATLAB software [3].
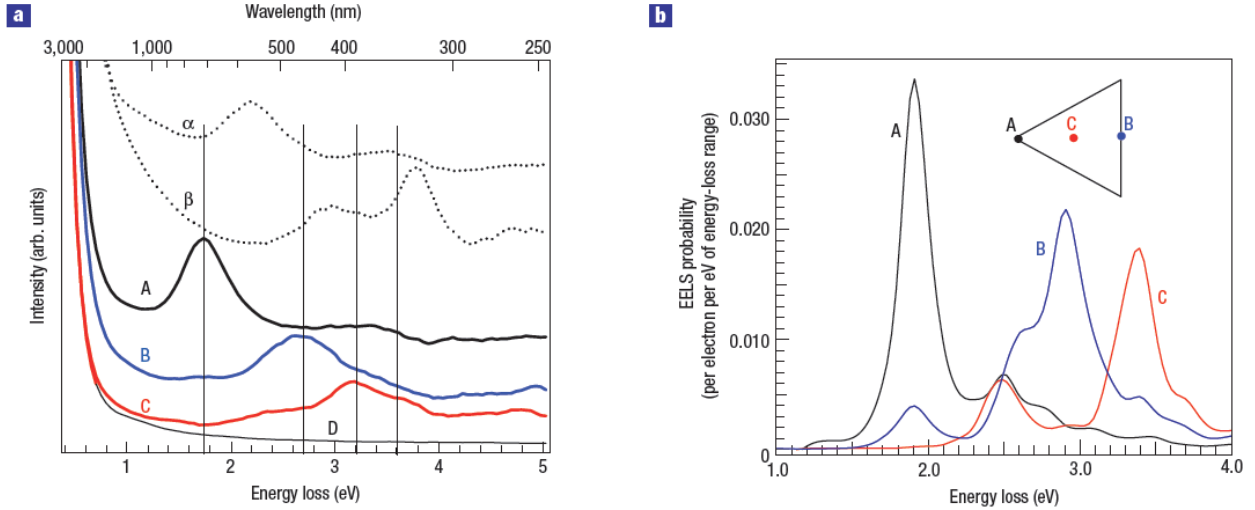
Figure 3.2: Comparison of experimental deconvoluted EEL spectra in a) with BEM calculations in b) reproduced from [41]. Measured structure had a shape of equilateral silver nanoprism with 78-nm-long sides and spectra were measured for three different positions of electron beam (A, B, C) as we can see in the inset of part b). In part a) containing measured data it is possible to observe spectra D corresponding to energy loss of the mica substrate that was proven to have no influence on EEL spectra of the particle. Energies of the peaks correspond to excitation of different modes in the nanoparticle and are quite well reproduced by the simulated spectra in b).

3.2. Discrete dipole approximation

Another possible approach is to use the discrete dipole approximation (DDA), which was developed in 1980s for calculations of scattering by interstellar graphite grains [13]. It is used especially in cases, where scattering of a plane wave is sought, but it is possible to modify this approach for electron energy loss calculations.

The main idea of the DDA is to model the particle by set of N interacting dipoles situated at specified positions $\mathbf{r}_j$, where $j = 1, 2, ..., N$. We then assign a polarizability α_j to each element whose dipole moment can be expressed as [13]

$$\mathbf{p}(\mathbf{r}_j) = \alpha_j \mathbf{E}(\mathbf{r}_j), \tag{3.10}$$

where $\mathbf{E}(\mathbf{r}_j)$ is the field at position $\mathbf{r}_j$. This field consists of an applied external field and a field coming from the other $N - 1$ dipoles

$$\mathbf{E}(\mathbf{r}_j) = \mathbf{E}^{\text{ext}}(\mathbf{r}_j) + \sum_{k \neq j}^{N} \mathbf{A}_{jk} \mathbf{p}_k. \tag{3.11}$$

$\mathbf{A}_{jk}$ represents the 3×3 dipole interaction matrix with elements:

$$\mathbf{A}_{jk} = \frac{\exp(\mathrm{i}kr_{jk})}{r_{jk}} \left[k^2 \left(\mathbf{I} - \frac{\mathbf{r}_{jk}\mathbf{r}_{jk}}{r_{jk}^2} \right) - \frac{1 - \mathrm{i}kr_{jk}}{r_{jk}^2} \left(\mathbf{I} - 3\frac{\mathbf{r}_{jk}\mathbf{r}_{jk}}{r_{jk}^2} \right) \right], \tag{3.12}$$

where $\mathbf{r}_{jk} = \mathbf{r}_j - \mathbf{r}_k$ and $r_{jk} = |\mathbf{r}_{jk}|$. Eq. (3.11) can be rewritten as

$$\mathbf{p}(\mathbf{r}_j) = \alpha_j \left(\mathbf{E}^{\text{ext}}(\mathbf{r}_j) + \sum_{k \neq j}^{N} \mathbf{A}_{jk} \mathbf{p}_k \right), \tag{3.13}$$

which is the $3N \times 3N$ system of equations that can be solved numerically to get $\mathbf{p}(\mathbf{r}_j)$ for a given external field.
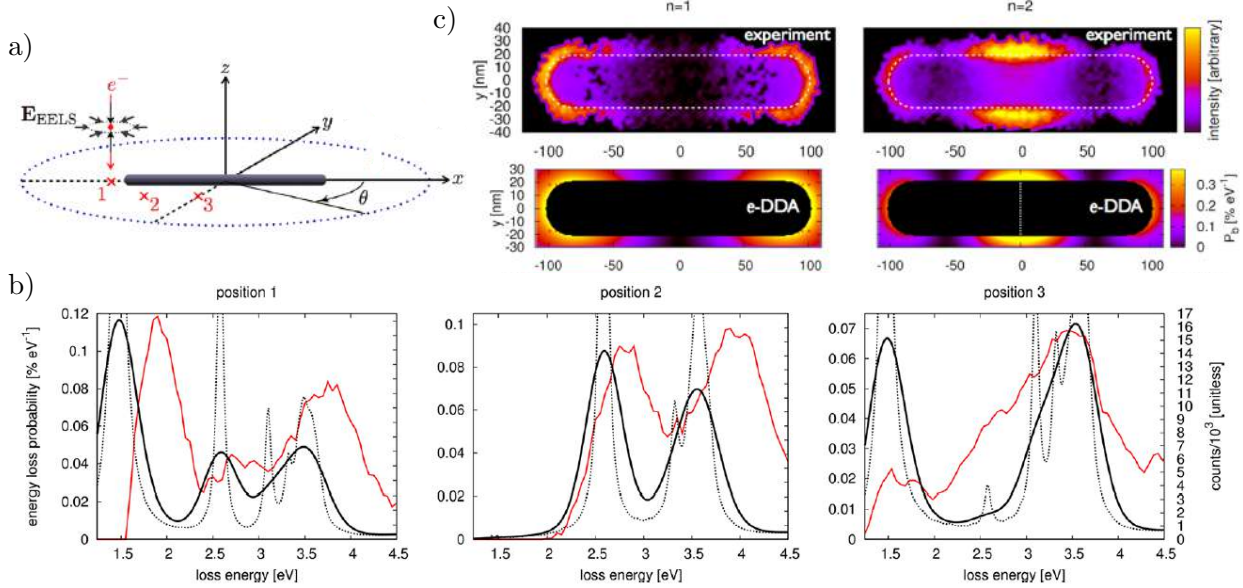

Figure 3.3: Comparison of experimental data with DDA calculations [8]. In part a) there is a scheme of measurement, for a silver nanorod of length 200 nm and width 40 nm situated on amorphous SiN$_{\text{x}}$ substrate. EEL spectra were measured for three marked position of the beam. Comparison of experimental (red line) and calculated data (dotted black line) convoluted by a Gaussian function (solid black line) for these three situations can be found in part b), where we can see that for each position of the beam different modes can be excited. If we scan the sample and record EEL spectra in each scanned position, we can plot EELS maps visualizing the loss probability related to a particular energy. In this case, the probability of loosing energy 1.5 eV corresponding to the first bright mode ($n = 1$) and 2.6 eV related to the first dark mode ($n = 2$), which can not be excited optically, is shown in c). The upper picture is the experimentally measured EELS map and the lower one is the simulated map by the DDA approach.

This approach can be applied in the case of an external field produced by the electron, where we can use the results from section 2.1. We also have to define the polarizability of the elements. For this purpose, Clausius-Mossotti relation is mostly used [27]

$$\alpha_j^{\text{C-M}} = \frac{3V}{4} \frac{\varepsilon_j - 1}{\varepsilon_j + 2}, \tag{3.14}$$

where V is volume of element and ε_j is dielectric function at position $\mathbf{r}_j$. Once we calculate all the dipole moments $\mathbf{p}(\mathbf{r}_j)$, we can obtain the total loss probability [27]

$$\Gamma(\omega) = \frac{1}{\pi \hbar^2} \sum_{j=1}^{N} \text{Im} \left[\mathbf{E}^{\text{ext}}(\mathbf{r}_j) \cdot \mathbf{p}(\mathbf{r}_j) \right]. \tag{3.15}$$

A direct application of this method was introduced e.g. in [27], where an attempt to include the effect of the substrate was made, or in [28] together with an improvement of the DDA approach by employing the eigenvector expansion method. Comparison with the experiment was introduced in [8], whereas quite good agreement was obtained as we can see from figure 3.3.

3.3. Finite-difference time-domain

Another possibility for numerical evaluation of the energy loss is to use the finite-difference in time-domain (FDTD) method. Within this method we study the time development of the fields obtained by discretization of Maxwell's equations. In electrodynamics, FDTD is widely used to deal with problems including scattering of light, but in the case of interaction of electrons with particles, the approaches mentioned in previous sections are usually employed. Nevertheless, in [11] it was shown that it is possible to obtain electron energy loss spectra by this approach, using FDTD Lumerical Solutions [2]. Moreover, the simulated spectra were in good agreement with experimental results.

The electron beam was modelled by a series of dipoles with phase delay related to the electron velocity localized along its trajectory. This unfortunately raises a few problems – e.g. additional radiation produced due to the sudden appearance and disappearance of the electron as we simulate only a finite part of the path. Because of that a reference simulation has to be performed [1].
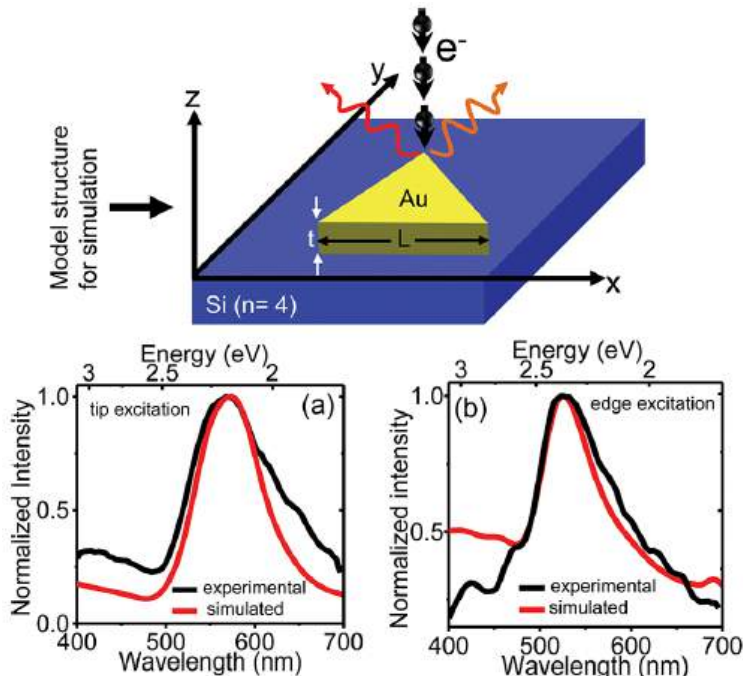

Figure 3.4: Comparison of measured EEL spectra with spectra simulated by FDTD software published in [11]. In the upper part of the figure we can see a scheme of the configuration: a gold nanoprism was situated on Si substrate and the electron beam was modelled by a set of dipoles. Spectra are shown for tip excitation (corresponds to the beam position A in figure 3.2) and edge excitation (beam position B in figure 3.2). For both situations numerically calculated data reproduce almost perfectly the measured loss probability.

4. Interaction of spherical particles with an electron beam

The beginning of this chapter is devoted to the derivation of analytical expressions for the interaction of spherical particles with fast electrons published in [20]. We then compare energy losses and fields calculated analytically with those obtained numerically from MNPBEM. Expressing the fields in frequency domain is the starting point for the following chapters, where we will continue with transformations to real time.

4.1. Multipole expansion of the field produced by fast electron

To obtain the analytical solution of the field produced by spherical particles due to presence of an electron moving nearby, we express the incident external field in a way suitable to the spherical geometry of our problem. We will follow the solution published in [20] using atomic units ($e = m_e = \hbar = 1$).

We assume the electron moving in the positive z direction [$\mathbf{v} = (0, 0, v)$] with impact position expressed in cylindrical coordinates $\mathbf{r}_0 = (b, \phi_0, z_0)$ as sketched in figure 4.1.
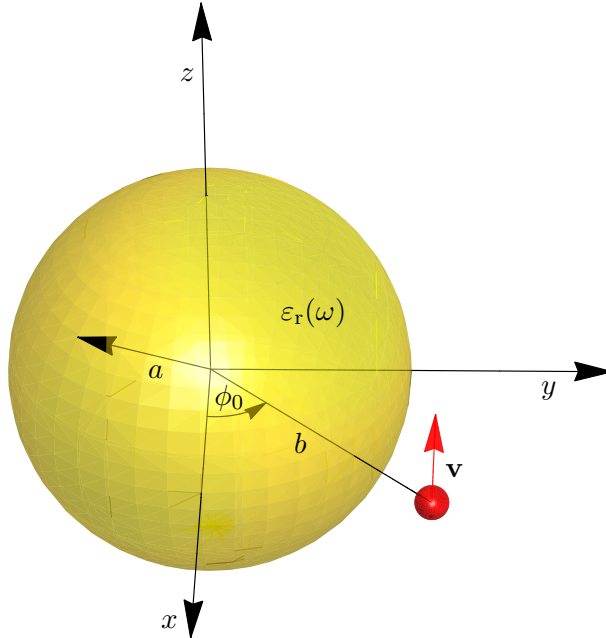

Figure 4.1: Scheme of a metal sphere with dielectric function $\varepsilon_{\mathrm{r}}(\omega)$ and electron with velocity $\mathbf{v}$ (plotted as small red sphere) moving nearby. Current position of depicted electron is $\mathbf{r}_{\mathrm{t}} = (b, \phi_0, 0)$ with respect to the sphere centered at the origin of the coordinate system.

We first recall the equation for the electric field expressed in terms of the scalar and vector potentials in real space as shown in Eq. (2.4) and rewrite the incident external field as

$$\mathbf{E}^{\mathrm{ext}}(\mathbf{r}) = \left(\nabla - \frac{\mathrm{i}k\mathbf{v}}{c} \right) \int G_0(\mathbf{r} - \mathbf{r}_{\mathrm{t}}) \exp(\mathrm{i}\omega t) \mathrm{d}t, \tag{4.1}$$

where we introduce the Green's function of the wave equation

4.1. MULTIPOLE EXPANSION OF THE FIELD PRODUCED BY FAST ELECTRON

$$G_0(\mathbf{r} - \mathbf{r}_t) = \frac{\exp(ik|\mathbf{r} - \mathbf{r}_t|)}{|\mathbf{r} - \mathbf{r}_t|} \tag{4.2}$$

and where $\mathbf{r}_t = \mathbf{r}_0 + \mathbf{v}t$ is the position of the trajectory of the electron. $k = \omega/c$ is the magnitude of the wave vector in vacuum.

The Green's function in Eq. (4.2) in free space can be expanded in terms of multipoles. If we consider an external trajectory and positions $\mathbf{r}$ near the surface when $r < r_t$, the Green's function can be expanded as

$$G_0(\mathbf{r}, \mathbf{r}_t) = 4\pi k \sum_{n=0}^{\infty} \sum_{m=-n}^{n} j_n(kr) h_n^{(+)}(kr_t) Y_{n,m}(\Omega_\mathbf{r}) Y_{n,m}^*(\Omega_{\mathbf{r}_t}), \tag{4.3}$$

where $h_n^{(+)}(x) = i h_n^{(1)}(x)$, $h_n^{(1)}(x)$ is the spherical Hankel function of the first kind, $(r, \Omega_\mathbf{r})$ and $(r_t, \Omega_{\mathbf{r}_t})$ are the spherical coordinates of $\mathbf{r}$ and $\mathbf{r}_t$. General solution of this problem can be found in [40]. We have to divide the solution in four different cases related to all possible configurations (calculation of the fields inside the sphere for external trajectory, field outside for internal trajectory etc.) [5].

Now we can substitute Eq. (4.3) into Eq. (4.1) and obtain

$$\mathbf{E}^{\text{ext}}(\mathbf{r}) = \left(\nabla - \frac{ik\mathbf{v}}{c}\right) \sum_{n=0}^{\infty} \sum_{m=-n}^{n} j_n(kr) Y_{n,m}(\Omega_\mathbf{r}) \phi_{n,m}, \tag{4.4}$$

where $j_n(x)$ is the spherical Bessel function of the first kind, $\phi_{n,m}$ is expressed as

$$\phi_{n,m} = 4\pi k \int h_n^{(+)}(kr_t) Y_{n,m}^*(\Omega_{\mathbf{r}_t}) dt \tag{4.5}$$

and the spherical harmonics $Y_{n,m}(r, \Omega_\mathbf{r})$ are defined as

$$Y_{n,m}(r, \theta, \phi) = \sqrt{\frac{2n+1}{4\pi} \frac{(n-m)!}{(n+m)!}} P_n^m(\cos\theta) \exp(im\phi) = \alpha_{n,m} P_n^m(\cos\theta) \exp(im\phi), \tag{4.6}$$

where $P_n^m(\cos\theta)$ are the associated Legendre polynomials.

It is possible to solve the integral in Eq. (4.5) analytically. Now we label

$$M_{n,m}(\mathbf{r}_0) = \int h_n^{(+)}(k|\mathbf{r}_0 + \mathbf{v}t|) Y_{n,m}^*(\Omega_{\mathbf{r}_0+\mathbf{v}t}) \exp(i\omega t) dt. \tag{4.7}$$

In our case we assumed $\mathbf{v}$ parallel to the z axis, $M_{n,m}(\mathbf{r}_0)$ can be therefore expressed as

$$M_{n,m}(\mathbf{r}_0) = M_{n,m}(b, 0, 0) \exp(-im\phi_0) \exp(-i\omega z_0/v) \tag{4.8}$$

and morover

$$M_{n,-m}(b, 0, 0) = (-1)^m M_{n,m}(b, 0, 0) \tag{4.9}$$

holds. For this reason we can consider $m \geq 0$ and $\phi_0 = z_0 = 0$. We first transform the retarded Green's function in Eq. (4.2)

$$\int \frac{\exp(ik|\mathbf{r} - (b, 0, vt)|)}{|\mathbf{r} - (b, 0, vt)|} \exp(i\omega t) dt = \frac{2}{v} K_0\left(\frac{\omega}{v\gamma}\sqrt{(x-b)^2 + y^2}\right) \exp(i\omega z/v), \tag{4.10}$$

where $\gamma = 1/\sqrt{1 - \beta^2}$ is the Lorentz contraction factor, and recall Eq. (4.3) to obtain

$$4\pi k \sum_{n=0}^{\infty} \sum_{m=-n}^{n} j_n(kr)Y_{n,m}(\Omega_{\mathbf{r}})M_{n,m}(b,0,0) = \frac{2}{v}K_0\left(\frac{\omega}{v\gamma}\sqrt{(x-b)^2+y^2}\right)\exp(\mathrm{i}\omega z/v). \qquad (4.11)$$

Now we multiply both sides of Eq. (4.11) by $Y_{n,m}^*(\Omega_{\mathbf{r}})$, integrate over $\Omega_{\mathbf{r}} = (\theta, \phi)$ and thanks to the orthogonality of the spherical harmonics we obtain

$$M_{n,m}(b,0,0) = \frac{1}{2\pi kv}\frac{1}{j_n(kr)}\int Y_{n,m}^*(\Omega_{\mathbf{r}})K_0\left(\frac{\omega}{v\gamma}\sqrt{(x-b)^2+y^2}\right)\exp(\mathrm{i}\omega z/v)\mathrm{d}\Omega_{\mathbf{r}}. \qquad (4.12)$$

If we further use the relationship

$$\int_{-\pi}^{\pi} \exp(-\mathrm{i}m\phi)K_0\left(\frac{\omega}{v\gamma}\sqrt{(x-b)^2+y^2}\right)\mathrm{d}\phi = 2\pi I_m\left(\frac{\omega R}{v\gamma}\right)K_m\left(\frac{\omega b}{v\gamma}\right), \qquad (4.13)$$

where $R = \sqrt{x^2+y^2}$ and where $\exp(-\mathrm{i}m\phi)$ comes from the spherical harmonics, we can perform the integration over ϕ, and only the integral over θ remains:

$$M_{n,m}(b,0,0) = \frac{\alpha_{n,m}}{kvj_n(kr)}K_m\left(\frac{\omega b}{v\gamma}\right)\int_{-1}^{1} I_m\left(\frac{\omega R}{v\gamma}\right)\exp(\mathrm{i}\omega z/v)P_n^m(\mu)\mathrm{d}\mu. \qquad (4.14)$$

In Eq. (4.14) we used the substitution $\mu = \cos(\theta)$ and the transformation from spherical to cylindrical coordinates $(R = r\sqrt{1-\mu^2}, z = r\mu)$. Now we take the limit $kr \to 0$, $j_n(kr) \to (kr)^l/(2l+1)!!$, which must be compensated by the vanishing integral. Considering this limit, we use Taylor expansion of the modified Bessel function and the exponential function

$$I_m(z) = \left(\frac{1}{2}z\right)^m \sum_{k=0}^{\infty} \frac{\left(\frac{1}{4}z^2\right)^k}{k!\Gamma(m+k+1)} \qquad \text{and} \qquad \exp(z) = \sum_{k=0}^{\infty} \frac{z^k}{k!}. \qquad (4.15)$$

These expansions can be substituted in the integral contained in Eq. (4.14) to obtain

$$\int\limits_{-1}^{1} \mathrm{d}\mu\, I_m\left(\frac{\omega R}{v\gamma}\right) \exp(\mathrm{i}\omega z/v) P_n^m(\mu)$$

$$= \int\limits_{-1}^{1} \mathrm{d}\mu \left(\frac{1}{2}\frac{\omega\sqrt{1-\mu^2}r}{v\gamma}\right)^m \sum_{k=0}^{\infty} \frac{\left(\frac{1}{4}(1-\mu^2)\right)^k \left(\frac{\omega r}{v\gamma}\right)^{2k}}{k!\Gamma(m+k+1)} \sum_{o=0}^{\infty} \frac{\left(\mathrm{i}\omega\frac{z}{v}\right)^o}{o!} \mu^o P_n^m(\mu)$$

$$= \int\limits_{-1}^{1} \mathrm{d}\mu \sum_{p=0}^{\infty}\sum_{q=0}^{p} \left(\frac{1}{2\gamma}\right)^{m+2q} \left(\frac{\omega r}{v}\right)^{m+2q} \left(\frac{\omega r}{v}\right)^{p-q} (1-\mu^2)^{\frac{m+2q}{2}} \frac{\mu^{p-q}}{(p-q)!} \frac{\mathrm{i}^{p-q} P_n^m(\mu)}{q!\Gamma(m+q+1)}$$

$$= \int\limits_{-1}^{1} \mathrm{d}\mu \sum_{q=0}^{\infty}\sum_{p=q}^{\infty} \left(\frac{1}{2\gamma}\right)^{m+2q} \left(\frac{\omega r}{v}\right)^{m+2q} \left(\frac{\omega r}{v}\right)^{p-q} (1-\mu^2)^{\frac{m+2q}{2}} \frac{\mu^{p-q}}{(p-q)!} \frac{\mathrm{i}^{p-q} P_n^m(\mu)}{q!\Gamma(m+q+1)}$$

$$= \int\limits_{-1}^{1} \mathrm{d}\mu \sum_{j=m}^{\infty}\sum_{p=\frac{j-m}{2}}^{\infty} \left(\frac{1}{2\gamma}\right)^{j} \left(\frac{\omega r}{v}\right)^{j} \left(\frac{\omega r}{v}\right)^{p-\frac{j-m}{2}} (1-\mu^2)^{\frac{j}{2}} \frac{\mu^{p-\frac{j-m}{2}}}{(p-\frac{j-m}{2})!} \frac{\mathrm{i}^{p-\frac{j-m}{2}} P_n^m(\mu)}{\left(\frac{j-m}{2}\right)!\left(\frac{j+m}{2}\right)!}$$

$$= \int\limits_{-1}^{1} \mathrm{d}\mu \sum_{j=m}^{\infty}\sum_{s=j}^{\infty} \left(\frac{1}{2\gamma}\right)^{j} \left(\frac{\omega r}{v}\right)^{s} (1-\mu^2)^{\frac{j}{2}} \frac{\mu^{s-j}}{(s-j)!} \frac{\mathrm{i}^{s-j} P_n^m(\mu)}{\left(\frac{j-m}{2}\right)!\left(\frac{j+m}{2}\right)!}$$

$$= \sum_{j=m}^{\infty}\sum_{s=j}^{\infty} \left(\frac{1}{2\gamma}\right)^{j} \left(\frac{\omega r}{v}\right)^{s} \frac{\mathrm{i}^{s-j}}{(s-j)!\left(\frac{j-m}{2}\right)!\left(\frac{j+m}{2}\right)!} \int\limits_{-1}^{1} \mathrm{d}\mu\, \mu^{s-j}(1-\mu^2)^{\frac{j}{2}} P_n^m(\mu). \qquad (4.16)$$

In Eq. (4.16) we used rules for discrete convolution, change of variables and we also reversed the order of summation and integration. The sum over j is restricted to even $j + m$ integers. Now we label

$$I_{i_1,i_2}^{n,m} = \int\limits_{-1}^{1} \mu^{i_2}(1-\mu^2)^{\frac{i_1}{2}} P_n^m(\mu)\mathrm{d}\mu. \qquad (4.17)$$

To evaluate Eq. (4.17) for different n, m, we can utilize recurrence relationships for the associated Legendre polynomials

$$(n-m)P_n^m(\mu) = (2n-1)\mu P_{n-1}^m(\mu) - (n+m-1)P_{n-2}^m(\mu). \qquad (4.18)$$

If we insert this relation into Eq. (4.17), we obtain similar relation for $I_{i_1,i_2}^{n,m}$ with index $n > m$

$$(n-m)I_{i_1,i_2}^{n,m} = (2n-1)I_{i_1,i_2+1}^{n-1,m} - (n+m-1)I_{i_1,i_2}^{n-2,m}. \qquad (4.19)$$

Starting values of the recurrence are

$$I_{i_1,i_2}^{m-1,m} = 0 \qquad (4.20)$$

and

$$I_{i_1,i_2}^{m,m} = \begin{cases} (-1)^m(2m-1)!!B\left(\frac{i_1+m+2}{2},\frac{i_2+1}{2}\right), & \text{if } i_2 \text{ is even} \\ 0, & \text{if } i_2 \text{ is odd,} \end{cases} \qquad (4.21)$$

where $B(x, y)$ is the beta function. This can be derived from the starting values of recurrence related to the associated Legendre polynomials

$$P_m^m(\mu) = (-1)^m (2m-1)!! (1-\mu^2)^{m/2}, \tag{4.22}$$

which can be inserted into Eq. (4.17):

$$I_{i_1,i_2}^{m,m} = (-1)^m (2m-1)!! \int_{-1}^{1} \mu^{i_2} (1-\mu^2)^{\frac{i_1+m}{2}} \mathrm{d}\mu. \tag{4.23}$$

After realizing that $B(x, y) = 2 \int_0^{\pi/2} \mathrm{d}\theta \, (\sin\theta)^{2x-1}(\cos\theta)^{2y-1}$ and performing the substitution $\mu = \cos\theta$, we easily obtain Eq. (4.21). We can also find out that $I_{j,s-j}^{l,m} = 0$ for $s < n$ and $j \geq m$, therefore only one summation over j is needed in (4.16). The final expression for $M_{n,m}(b, 0, 0)$ then reads

$$M_{n,m}(b,0,0) = \int \exp(\mathrm{i}\omega t) h_l^{(+)} \left[k|(b,0,vt)| \right] Y_{l,m} \left[\Omega_{(b,0,vt)} \right] \mathrm{d}t = \frac{A_{n,m}^+}{\omega} K_m \left(\frac{\omega b}{v\gamma} \right), \tag{4.24}$$

where

$$A_{n,m}^+ = \frac{1}{\beta^{n+1}} \sum_{j=m}^{n} \frac{\mathrm{i}^{n-j}\alpha_{n,m}(2n+1)!!}{\gamma^j 2^j (n-j)![(j-m)/2]![(j+m)/2]!} I_{j,n-j}^{n,m}. \tag{4.25}$$

The expression for $\phi_{n,m}$ can be also recovered:

$$\phi_{n,m} = 4\pi k \frac{A_{n,m}^+}{\omega} K_m \left(\frac{\omega b}{v\gamma} \right) \exp(-\mathrm{i}m\varphi_0 - \mathrm{i}\omega z_0/v). \tag{4.26}$$

Now we introduce electric and magnetic scalar functions

$$\psi^{\mathrm{M},\eta} = \frac{1}{\mathrm{L}^2} \mathbf{L} \cdot \mathbf{E}^\eta \qquad \psi^{\mathrm{E},\eta} = \frac{-\mathrm{i}k}{\mathrm{L}^2 \nabla^2} (\mathbf{L} \times \nabla) \cdot \mathbf{E}^\eta, \tag{4.27}$$

where $\mathbf{L} = -\mathrm{i}\mathbf{r} \times \nabla$ is the orbital angular-momentum operator and superscript $^\eta$ can stand either for $^{\mathrm{ext}}$ or $^{\mathrm{ind}}$, denoting the external and induced fields, respectively. The fields can be reversely expressed from the scalar functions

$$\mathbf{E}^\eta = \mathbf{L}\psi^{\mathrm{M},\eta} - \frac{\mathrm{i}}{k}\nabla \times \mathbf{L}\psi^{\mathrm{E},\eta}, \tag{4.28}$$

$$\mathbf{B}^\eta = -\mathbf{L}\psi^{\mathrm{E},\eta} - \frac{\mathrm{i}}{k}\nabla \times \mathbf{L}\psi^{\mathrm{M},\eta\,1}. \tag{4.29}$$

When we insert our external electric field in Eq. (4.4) with Eq. (4.26) into Eq. (4.27) and make some manipulation with the operators $\mathbf{L}\cdot$ and $\mathbf{L} \times \nabla$, which is outlined in [20], we find out that the scalar functions must take the

---

[1]In this definition the Gaussian system, where $\mathbf{E}$ and $\mathbf{B}$ have the same dimension, has been adopted. To obtain the expression for $\mathbf{B}$ in SI units, the right-hand side of the equation has to be divided by $c = 1/\alpha = 137$ in atomic units. Therefore, if we want to convert the magnetic field from our definition to SI units, we have to multiply its value in a.u. by $\hbar/(ea_0^2c) = 1.716 \cdot 10^3$ T. The electric field in SI units can be obtained from a multiplication by $e/(4\pi\varepsilon_0 a_0^2) = 5.142 \cdot 10^{11}$ V/m, where a_0 is Bohr's radius.

$$\psi^{\mathrm{M,ext}}(\mathbf{r}) = \sum_{n=1}^{\infty} \sum_{m=-n}^{n} \mathrm{i}^n j_n(kr) Y_{n,m}(\Omega_{\mathbf{r}}) \psi_{n,m}^{\mathrm{M,ext}}, \tag{4.30}$$

$$\psi^{\mathrm{E,ext}}(\mathbf{r}) = \sum_{n=1}^{\infty} \sum_{m=-n}^{n} \mathrm{i}^n j_n(kr) Y_{n,m}(\Omega_{\mathbf{r}}) \psi_{n,m}^{\mathrm{E,ext}}, \tag{4.31}$$

with coefficients

$$\psi_{n,m}^{\mathrm{M,ext}} = \frac{-4\pi \mathrm{i}^{1-n} k v}{c^2} \frac{m A_{n,m}^+}{n(n+1)} K_m\left(\frac{\omega b}{v\gamma}\right) \exp(-\mathrm{i}m\varphi_0 - \mathrm{i}\omega z_0/v), \tag{4.32}$$

$$\psi_{n,m}^{\mathrm{E,ext}} = \frac{-2\pi \mathrm{i}^{1-n} k}{c\gamma} \frac{B_{n,m}}{n(n+1)} K_m\left(\frac{\omega b}{v\gamma}\right) \exp(-\mathrm{i}m\varphi_0 - \mathrm{i}\omega z_0/v), \tag{4.33}$$

where $B_{n,m}$ is defined as

$$B_{n,m} = A_{n,m+1}^+ \sqrt{(n+m+1)(n-m)} - A_{n,m-1}^+ \sqrt{(n-m+1)(n+m)}. \tag{4.34}$$

4.2. External fields

With the use of the previous expressions it is possible now to directly calculate the electric and magnetic fields by substituting the scalar function in Eqs. (4.30) and (4.31) together with the expansion coefficients to Eqs. (4.28) and (4.29), respectively:

$$\mathbf{E}^{\mathrm{ext}} = -\mathrm{i}\mathbf{r} \times \nabla\psi^{\mathrm{M,ext}} - \frac{1}{k}\nabla \times \left(\mathbf{r} \times \nabla\psi^{\mathrm{E,ext}}\right) \qquad \mathbf{B}^{\mathrm{ext}} = \mathrm{i}\mathbf{r} \times \nabla\psi^{\mathrm{E,ext}} - \frac{1}{k}\nabla \times \left(\mathbf{r} \times \nabla\psi^{\mathrm{M,ext}}\right). \tag{4.35}$$

The most convenient way to compute particular components of the fields outside a spherical particle is to use the spherical coordinate system [2]. We take $\mathbf{r} = (r, 0, 0)$, change the order of summation and differentiation and perform the required operations:

$$\begin{aligned}
\nabla\psi^{\kappa,\mathrm{ext}} = \mathbf{e}_r \sum_{n=1}^{\infty} \sum_{m=-n}^{n} & \psi_{n,m}^{\kappa,\mathrm{ext}} \mathrm{i}^n Y_{n,m}(\theta,\phi) \frac{\partial j_n(kr)}{\partial r} \\
+ \mathbf{e}_\theta \sum_{n=1}^{\infty} \sum_{m=-n}^{n} & \psi_{n,m}^{\kappa,\mathrm{ext}} \frac{1}{r} \mathrm{i}^n j_n(kr) \frac{\partial Y_{n,m}(\theta,\phi)}{\partial \theta} \\
+ \mathbf{e}_\phi \sum_{n=1}^{\infty} \sum_{m=-n}^{n} & \psi_{n,m}^{\kappa,\mathrm{ext}} \frac{1}{r\sin\theta} \mathrm{i}^n j_n(kr) \frac{\partial Y_{n,m}(\theta,\phi)}{\partial \phi},
\end{aligned} \tag{4.36}$$

$$\begin{aligned}
\mathbf{r} \times \nabla\psi^{\kappa,\mathrm{ext}} = -\mathbf{e}_\theta \sum_{n=1}^{\infty} \sum_{m=-n}^{n} & \psi_{n,m}^{\kappa,\mathrm{ext}} \frac{1}{\sin\theta} \mathrm{i}^n j_n(kr) \frac{\partial Y_{n,m}(\theta,\phi)}{\partial \phi} \\
+ \mathbf{e}_\phi \sum_{n=1}^{\infty} \sum_{m=-n}^{n} & \psi_{n,m}^{\kappa,\mathrm{ext}} \mathrm{i}^n j_n(kr) \frac{\partial Y_{n,m}(\theta,\phi)}{\partial \theta},
\end{aligned} \tag{4.37}$$

---

[2]Gradient of a scalar function $f = f(r,\theta,\phi)$ in the spherical coordinates is expressed as $\nabla f = \mathbf{e}_r \frac{\partial f}{\partial r} + \mathbf{e}_\theta \frac{1}{r} \frac{\partial f}{\partial \theta} + \mathbf{e}_\phi \frac{1}{r\sin\theta} \frac{\partial f}{\partial \phi}$, curl or a vector function $\mathbf{u} = (u_r(r,\theta,\phi), u_\theta(r,\theta,\phi), u_\phi(r,\theta,\phi))$ can be computed via $\nabla \times \mathbf{u} = \mathbf{e}_r \frac{1}{r\sin\theta}\left[\frac{\partial}{\partial\theta}(u_\phi\sin\theta) - \frac{\partial u_\theta}{\partial\phi}\right] + \mathbf{e}_\theta \frac{1}{r}\left[\frac{1}{\sin\theta}\frac{\partial u_r}{\partial\phi} - \frac{\partial}{\partial r}(ru_\phi)\right] + \mathbf{e}_\phi \frac{1}{r}\left[\frac{\partial}{\partial r}(ru_\theta) - \frac{\partial u_r}{\partial\theta}\right].$

$$\nabla \times (\mathbf{r} \times \nabla \psi^{\kappa,\text{ext}}) = \mathbf{e}_r \sum_{n=1}^{\infty} \sum_{m=-n}^{n} \psi_{n,m}^{\kappa,\text{ext}} \frac{1}{r\sin\theta} \left[\frac{\partial}{\partial \theta} \left(\sin\theta \mathrm{i}^n j_n(kr) \frac{\partial Y_{n,m}(\theta,\phi)}{\partial \theta} \right) \right.$$

$$+ \frac{\partial}{\partial \phi} \left(\frac{1}{\sin\theta} \mathrm{i}^n j_n(kr) \frac{\partial Y_{n,m}(\theta,\phi)}{\partial \phi} \right) \right]$$

$$- \mathbf{e}_\theta \sum_{n=1}^{\infty} \sum_{m=-n}^{n} \psi_{n,m}^{\kappa,\text{ext}} \frac{1}{r} \left[\frac{\partial}{\partial r} \left(r \mathrm{i}^n j_n(kr) \frac{\partial Y_{n,m}(\theta,\phi)}{\partial \theta} \right) \right]$$

$$- \mathbf{e}_\phi \sum_{n=1}^{\infty} \sum_{m=-n}^{n} \psi_{n,m}^{\kappa,\text{ext}} \frac{1}{r} \left[\frac{\partial}{\partial r} \left(\frac{r}{\sin\theta} \mathrm{i}^n j_n(kr) \frac{\partial Y_{n,m}(\theta,\phi)}{\partial \phi} \right) \right].$$

$$(4.38)$$

In the next step we have to compute the derivatives of special functions, where we use known relationships [4]:

$$\frac{\partial j_n(kr)}{\partial r} = -k j_{n+1}(kr) + \frac{n}{r} j_n(kr),$$

$$\frac{\partial h_n^{(+)}(kr)}{\partial r} = -k h_{n+1}^{(+)}(kr) + \frac{n}{r} h_n^{(+)}(kr),$$

$$\frac{\partial Y_{n,m}(\theta,\phi)}{\partial \theta} = \left[\frac{(n-m+1)}{\sin\theta} \frac{\alpha_{n,m}}{\alpha_{n+1,m}} Y_{n+1,m}(\theta,\phi) - (n+1)\frac{\cos\theta}{\sin\theta} Y_{n,m}(\theta,\phi) \right],$$

$$\frac{\partial Y_{n,m}(\theta,\phi)}{\partial \phi} = \mathrm{i} m Y_{n,m}(\theta,\phi)$$

$$(4.39)$$

and finally we can substitute Eqs. (4.37), (4.38) and (4.39) together with the relationships for the coefficients into Eq. (4.35) to get the external electric field

$$\mathbf{E}^{\text{ext}}(\mathbf{r},\omega) = \mathbf{e}_r \frac{-2\pi \mathrm{i}\omega}{c^2\gamma} \sum_{n=1}^{\infty} \sum_{m=-n}^{n} \frac{j_n(kr)}{kr} B_{n,m} K_m\left(\frac{\omega b}{v\gamma}\right) Y_{n,m}(\theta,\phi) \exp(-\mathrm{i}m\phi_0 - \mathrm{i}\omega z_0/v)$$

$$+ \mathbf{e}_\theta \left\{ \frac{4\pi \mathrm{i}\omega v}{c^3} \sum_{n=1}^{\infty} \sum_{m=-n}^{n} \frac{m^2}{n(n+1)\sin\theta} j_n(kr) A_{n,m}^+ K_m\left(\frac{\omega b}{v\gamma}\right) Y_{n,m}(\theta,\phi) \right.$$

$$+ \frac{2\pi \mathrm{i}\omega}{c^2\gamma} \sum_{n=1}^{\infty} \sum_{m=-n}^{n} \frac{B_{n,m}}{n(n+1)} K_m\left(\frac{\omega b}{v\gamma}\right) \left[(n+1)\frac{j_n(kr)}{kr} - j_{n+1}(kr) \right]$$

$$\times \left[\frac{(n+1)\cos\theta}{\sin\theta} Y_{n,m}(\theta,\phi) - \frac{(n-m+1)}{\sin\theta} \frac{\alpha_{n,m}}{\alpha_{n+1,m}} Y_{n+1,m}(\theta,\phi) \right] \right\} \exp(-\mathrm{i}m\phi_0 - \mathrm{i}\omega z_0/v)$$

$$+ \mathbf{e}_\phi \left\{ \frac{4\pi\omega v}{c^3} \sum_{n=1}^{\infty} \sum_{m=-n}^{n} \frac{m}{n(n+1)} j_n(kr) A_{n,m}^+ K_m\left(\frac{\omega b}{v\gamma}\right) \right.$$

$$\times \left[\frac{(n+1)\cos\theta}{\sin\theta} Y_{n,m}(\theta,\phi) - \frac{(n-m+1)}{\sin\theta} \frac{\alpha_{n,m}}{\alpha_{n+1,m}} Y_{n+1,m}(\theta,\phi) \right]$$

$$+ \frac{2\pi\omega}{c^2\gamma} \sum_{n=1}^{\infty} \sum_{m=-n}^{n} \frac{m}{n(n+1)\sin\theta} B_{n,m} K_m\left(\frac{\omega b}{v\gamma}\right) Y_{n,m}(\theta,\phi)$$

$$\times \left[(n+1)\frac{j_n(kr)}{kr} - j_{n+1}(kr) \right] \right\} \exp(-\mathrm{i}m\phi_0 - \mathrm{i}\omega z_0/v)$$
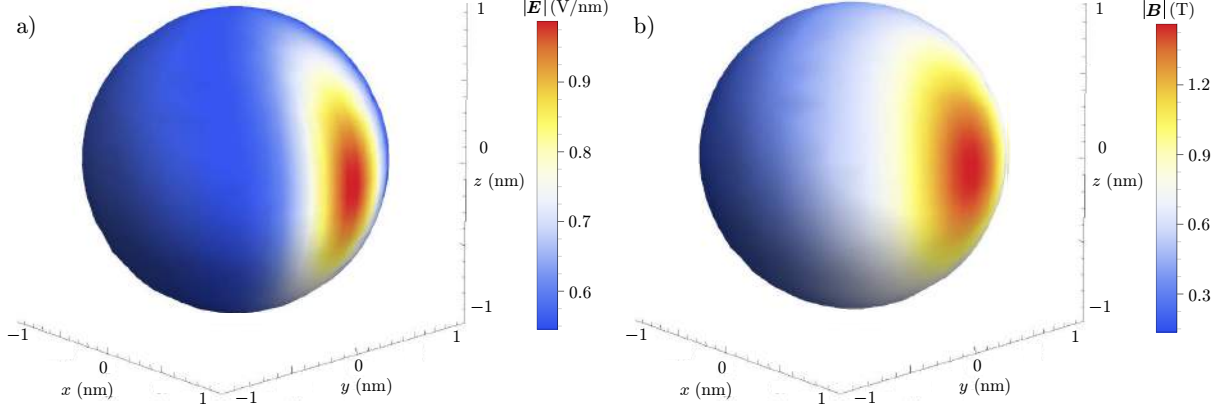
$$(4.40)$$

Figure 4.2: External electric field a) and external magnetic field b) produced by a moving electron of energy $120\,\mathrm{keV}$. Calculation was performed for a sphere of radius $a = 1\,\mathrm{nm}$, impact parameter $b = 1.5\,\mathrm{nm}$ and angle $\phi_0 = 0$. The external fields are plotted for energy $\hbar\omega = 3.94\,\mathrm{eV}$, which corresponds to the first peak of the nonretarded EEL spectra in figure 2.3 calculated for a sphere of the same size. The maximum index of summation was taken to be $n_{\mathrm{max}} = 10$.

and magnetic field

$$
\begin{aligned}
\mathbf{B}^{\mathrm{ext}}(\mathbf{r}, \omega) = {} & \mathbf{e}_r \frac{-4\pi\mathrm{i}\omega v}{c^3} \sum_{n=1}^{\infty} \sum_{m=-n}^{n} m \frac{j_n(kr)}{kr} A_{n,m}^+ K_m\left(\frac{\omega b}{v\gamma}\right) Y_{n,m}(\theta, \phi) \exp(-\mathrm{i}m\phi_0 - \mathrm{i}\omega z_0/v) \\
& + \mathbf{e}_\theta \left\{ \frac{-2\pi\mathrm{i}\omega}{c^2\gamma} \sum_{n=1}^{\infty} \sum_{m=-n}^{n} \frac{m}{n(n+1)\sin\theta} j_n(kr) B_{n,m} K_m\left(\frac{\omega b}{v\gamma}\right) Y_{n,m}(\theta, \phi) \right. \\
& + \frac{4\pi\mathrm{i}\omega v}{c^3} \sum_{n=1}^{\infty} \sum_{m=-n}^{n} \frac{m}{n(n+1)} A_{n,m}^+ K_m\left(\frac{\omega b}{v\gamma}\right) \left[(n+1)\frac{j_n(kr)}{kr} - j_{n+1}(kr)\right] \\
& \times \left[\frac{(n+1)\cos\theta}{\sin\theta} Y_{n,m}(\theta, \phi) - \frac{(n-m+1)}{\sin\theta} \frac{\alpha_{n,m}}{\alpha_{n+1,m}} Y_{n+1,m}(\theta, \phi) \right] \Bigg\} \exp(-\mathrm{i}m\phi_0 - \mathrm{i}\omega z_0/v) \\
& - \mathbf{e}_\phi \left\{ \frac{2\pi\omega}{c^2\gamma} \sum_{n=1}^{\infty} \sum_{m=-n}^{n} \frac{B_{n,m}}{n(n+1)} j_n(kr) K_m\left(\frac{\omega b}{v\gamma}\right) \right. \\
& \times \left[\frac{(n+1)\cos\theta}{\sin\theta} Y_{n,m}(\theta, \phi) - \frac{(n-m+1)}{\sin\theta} \frac{\alpha_{n,m}}{\alpha_{n+1,m}} Y_{n+1,m}(\theta, \phi) \right] \\
& - \frac{4\pi\omega v}{c^3} \sum_{n=1}^{\infty} \sum_{m=-n}^{n} \frac{m^2}{n(n+1)\sin\theta} A_{n,m}^+ K_m\left(\frac{\omega b}{v\gamma}\right) Y_{n,m}(\theta, \phi) \\
& \times \left[(n+1)\frac{j_n(kr)}{kr} - j_{n+1}(kr)\right] \Bigg\} \exp(-\mathrm{i}m\phi_0 - \mathrm{i}\omega z_0/v).
\end{aligned}
$$

$$(4.41)$$

The external fields for $n_{\mathrm{max}} = 10$ and the energy related to the first peak in the electron energy loss spectra of figure 2.3 calculated from Eq. (4.40) and Eq. (4.41) are depicted in figure 4.2.

4.3. Induced fields outside the particle

We analyse now the fields that are induced due to the presence of the sphere situated near electron's trajectory. To obtain these fields, we apply the boundary conditions requiring continuity of ψ^{M}, $\epsilon\psi^{\mathrm{E}}$, $\partial\psi^{\mathrm{M}}/\partial r$ and $(1 + r\partial/\partial r)\psi^{\mathrm{E}}$. The fields induced outside the sphere can be expressed as

$$\psi^{\mathrm{M,ind}}(\mathbf{r}) = \sum_{n=1}^{\infty} \sum_{m=-n}^{n} \mathrm{i}^n h_n^{(+)}(kr) Y_{n,m}(\Omega_{\mathbf{r}}) \psi_{n,m}^{\mathrm{M,ind}}, \tag{4.42}$$

$$\psi^{\mathrm{E,ind}}(\mathbf{r}) = \sum_{n=1}^{\infty} \sum_{m=-n}^{n} \mathrm{i}^n h_n^{(+)}(kr) Y_{n,m}(\Omega_{\mathbf{r}}) \psi_{n,m}^{\mathrm{E,ind}}, \tag{4.43}$$

where the coefficients of the induced fields are connected with those for external fields via

$$\psi_{n,m}^{\mathrm{M,ind}} = t_n^{\mathrm{M}} \psi_{n,m}^{\mathrm{M,ext}}, \tag{4.44}$$

$$\psi_{n,m}^{\mathrm{E,ind}} = t_n^{\mathrm{E}} \psi_{n,m}^{\mathrm{E,ext}}. \tag{4.45}$$

The coefficients t_n^{M} and t_n^{E} are the coefficients from Mie theory [39], [9]. We can rewrite them for the case of a non-magnetic sphere (when $\mu_{\mathrm{in}} = \mu = \mu_0$) as

$$t_n^{\mathrm{M}} = \frac{-j_n(ka)[k_{\mathrm{in}}aj_n(k_{\mathrm{in}}a)]' + j_n(k_{\mathrm{in}}a)[kaj_n(ka)]'}{h_n^+(ka)[k_{\mathrm{in}}aj_n(k_{\mathrm{in}}a)]' - j_n(k_{\mathrm{in}}a)[kah_n^+(ka)]'}, \tag{4.46}$$

$$t_n^{\mathrm{E}} = \frac{-j_n(ka)[k_{\mathrm{in}}aj_n(k_{\mathrm{in}}a)]' + \varepsilon_{\mathrm{r}}j_n(k_{\mathrm{in}}a)[kaj_n(ka)]'}{h_n^+(ka)[k_{\mathrm{in}}aj_n(k_{\mathrm{in}}a)]' - \varepsilon_{\mathrm{r}}j_n(k_{\mathrm{in}}a)[kah_n^+(ka)]'}, \tag{4.47}$$

where $k_{\mathrm{in}} = \varepsilon_{\mathrm{r}}\omega/c$ is magnitude of the wave vector inside the sphere. Knowing the coefficients we can easily modify the incident fields produced by the moving electron and get the induced fields just by exchanging $h_n^{(1)} \to -\mathrm{i}j_n$ (due to requirement of finiteness of the fields inside) and including the Mie coefficients in Eqs. (4.46) and (4.47). We can thus find the induced fields outside the sphere:

$$\mathbf{E}^{\text{ind}}(\mathbf{r}, \omega) = \mathbf{e}_r \frac{2\pi\omega}{c^2\gamma} \sum_{n=1}^{\infty} \sum_{m=-n}^{n} t_n^{\text{E}} \frac{h_n^{(1)}(kr)}{kr} B_{n,m} K_m\left(\frac{\omega b}{v\gamma}\right) Y_{n,m}(\theta, \phi) \exp(-\text{i}m\phi_0 - \text{i}\omega z_0/v)$$

$$- \mathbf{e}_\theta \left\{ \frac{4\pi\omega v}{c^3} \sum_{n=1}^{\infty} \sum_{m=-n}^{n} \frac{t_n^{\text{M}} m^2}{n(n+1)\sin\theta} h_n^{(1)}(kr) A_{n,m}^+ K_m\left(\frac{\omega b}{v\gamma}\right) Y_{n,m}(\theta, \phi) \right.$$

$$+ \frac{2\pi\omega}{c^2\gamma} \sum_{n=1}^{\infty} \sum_{m=-n}^{n} \frac{t_n^{\text{E}}}{n(n+1)} B_{n,m} K_m\left(\frac{\omega b}{v\gamma}\right) \left[(n+1)\frac{h_n^{(1)}(kr)}{kr} - h_{n+1}^{(1)}(kr) \right]$$

$$\times \left. \left[\frac{(n+1)\cos\theta}{\sin\theta} Y_{n,m}(\theta, \phi) - \frac{(n-m+1)}{\sin\theta} \frac{\alpha_{n,m}}{\alpha_{n+1,m}} Y_{n+1,m}(\theta, \phi) \right] \right\} \exp(-\text{i}m\phi_0 - \text{i}\omega z_0/v)$$

$$+ \mathbf{e}_\phi \left\{ \frac{4\pi\text{i}\omega v}{c^3} \sum_{n=1}^{\infty} \sum_{m=-n}^{n} \frac{t_n^{\text{M}} m}{n(n+1)} h_n^{(1)}(kr) A_{n,m}^+ K_m\left(\frac{\omega b}{v\gamma}\right) \right.$$

$$\times \left[\frac{(n+1)\cos\theta}{\sin\theta} Y_{n,m}(\theta, \phi) - \frac{(n-m+1)}{\sin\theta} \frac{\alpha_{n,m}}{\alpha_{n+1,m}} Y_{n+1,m}(\theta, \phi) \right]$$

$$+ \frac{2\pi\text{i}\omega}{c^2\gamma} \sum_{n=1}^{\infty} \sum_{m=-n}^{n} \frac{t_n^{\text{E}} m}{n(n+1)\sin\theta} B_{n,m} K_m\left(\frac{\omega b}{v\gamma}\right) Y_{n,m}(\theta, \phi)$$

$$\times \left. \left[(n+1)\frac{h_n^{(1)}(kr)}{kr} - h_{n+1}^{(1)}(kr) \right] \right\} \exp(-\text{i}m\phi_0 - \text{i}\omega z_0/v),$$

$$(4.48)$$

$$\mathbf{B}^{\text{ind}}(\mathbf{r}, \omega) = \mathbf{e}_r \frac{4\pi\omega v}{c^3} \sum_{n=1}^{\infty} \sum_{m=-n}^{n} t_n^{\text{M}} m \frac{h_n^{(1)}(kr)}{kr} A_{n,m}^+ K_m\left(\frac{\omega b}{v\gamma}\right) Y_{n,m}(\theta, \phi) \exp(-\text{i}m\phi_0 - \text{i}\omega z_0/v)$$

$$+ \mathbf{e}_\theta \left\{ \frac{2\pi\omega}{c^2\gamma} \sum_{n=1}^{\infty} \sum_{m=-n}^{n} \frac{t_n^{\text{E}} m}{n(n+1)\sin\theta} h_n^{(1)}(kr) B_{n,m} K_m\left(\frac{\omega b}{v\gamma}\right) Y_{n,m}(\theta, \phi) \right.$$

$$- \frac{4\pi\omega v}{c^3} \sum_{n=1}^{\infty} \sum_{m=-n}^{n} \frac{t_n^{\text{M}} m}{n(n+1)} A_{n,m}^+ K_m\left(\frac{\omega b}{v\gamma}\right) \left[(n+1)\frac{h_n^{(1)}(kr)}{kr} - h_{n+1}^{(1)}(kr) \right]$$

$$\times \left. \left[\frac{(n+1)\cos\theta}{\sin\theta} Y_{n,m}(\theta, \phi) - \frac{(n-m+1)}{\sin\theta} \frac{\alpha_{n,m}}{\alpha_{n+1,m}} Y_{n+1,m}(\theta, \phi) \right] \right\} \exp(-\text{i}m\phi_0 - \text{i}\omega z_0/v)$$

$$- \mathbf{e}_\phi \left\{ \frac{2\pi\text{i}\omega}{c^2\gamma} \sum_{n=1}^{\infty} \sum_{m=-n}^{n} \frac{t_n^{\text{E}}}{n(n+1)} h_n^{(1)}(kr) B_{n,m} K_m\left(\frac{\omega b}{v\gamma}\right) \right.$$

$$\times \left[\frac{(n+1)\cos\theta}{\sin\theta} Y_{n,m}(\theta, \phi) - \frac{(n-m+1)}{\sin\theta} \frac{\alpha_{n,m}}{\alpha_{n+1,m}} Y_{n+1,m}(\theta, \phi) \right]$$

$$- \frac{4\pi\text{i}\omega v}{c^3} \sum_{n=1}^{\infty} \sum_{m=-n}^{n} \frac{t_n^{\text{M}} m^2}{n(n+1)\sin\theta} A_{n,m}^+ K_m\left(\frac{\omega b}{v\gamma}\right) Y_{n,m}(\theta, \phi)$$

$$\times \left. \left[(n+1)\frac{h_n^{(1)}(kr)}{kr} - h_{n+1}^{(1)}(kr) \right] \right\} \exp(-\text{i}m\phi_0 - \text{i}\omega z_0/v).$$

$$(4.49)$$

We compare the induced fields calculated analytically from Eqs. (4.48) and (4.49) with the results obtained from the MNPBEM toolbox. These comparisons for a silver sphere with radius
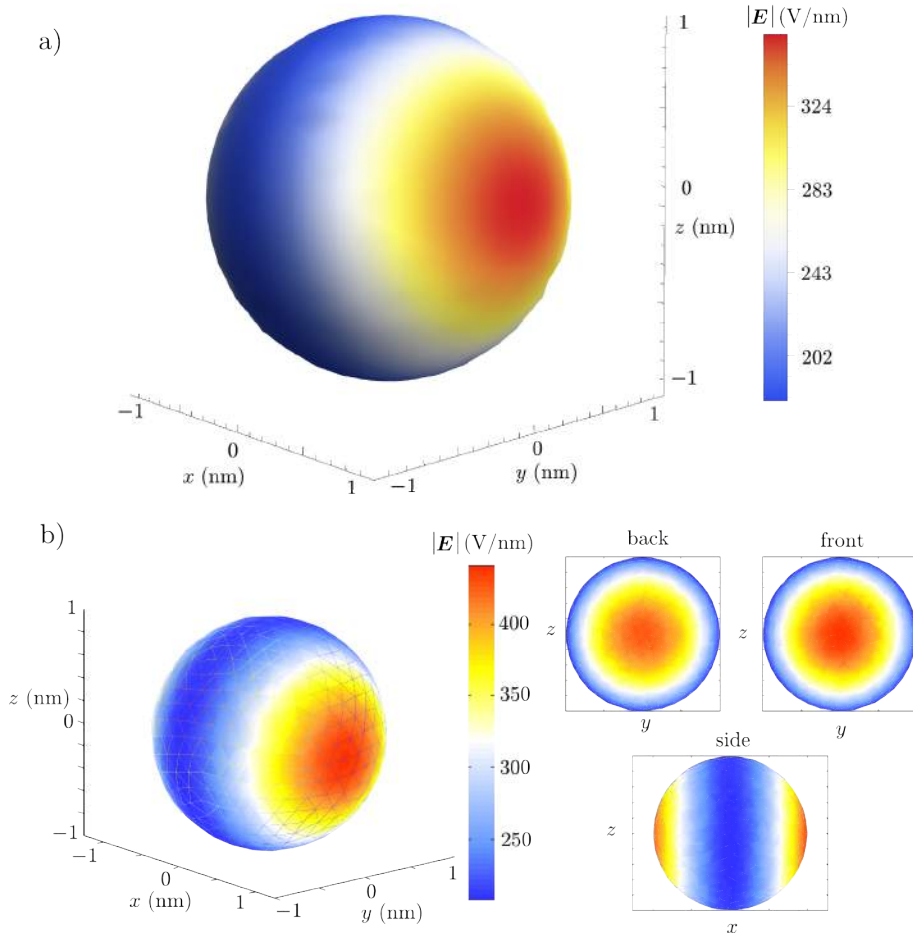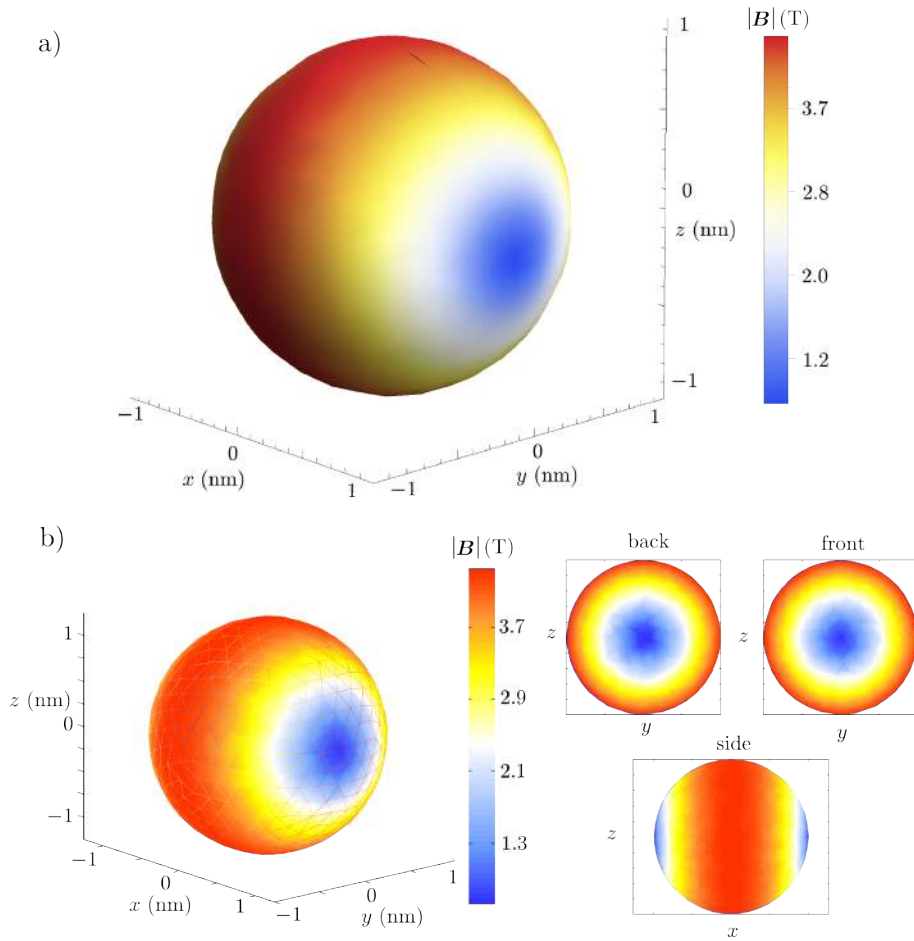
Figure 4.3: Comparison of the magnitude of the induced electric field on the surface of a silver sphere corresponding to the first mode of energy $\hbar\omega = 3.94\,\text{eV}$ computed analytically a), and numerically b) using the MNPBEM toolbox. The energy of this mode was identified in electron energy loss spectra in figure 2.3. The front side denotes the hemisphere facing the electron. Calculations were performed for a sphere radius $a = 1\,\text{nm}$, impact parameter $b = 1.5\,\text{nm}$ ($\phi_0 = 0$) and electrons of energy 120 keV. The response of silver was modelled by a Drude dielectric function with parameters from table B.1.

$a = 1\,\text{nm}$, impact parameter $b = 1.5\,\text{nm}$ and electrons of energy 120 keV can be found in figures 4.3 and 4.4 for the dipolar mode related to the first peak in the nonretarded electron energy loss spectra (figure 2.3), which, as we will show later, perfectly match the spectra obtained from the retarded approach introduced in this chapter.

Analytically expressed induced fields for higher order modes related to the second, third and fourth peak (these peaks are again labeled in figure 2.3)are depicted in figure 4.5. The Drude model was used to model the dielectric function of silver.

The total fields outside the sphere can be then expressed as a superposition of the external and induced fields

$$\mathbf{E}^{\text{out}} = \mathbf{E}^{\text{ext}} + \mathbf{E}^{\text{ind}} \qquad \text{and} \qquad \mathbf{B}^{\text{out}} = \mathbf{B}^{\text{ext}} + \mathbf{B}^{\text{ind}}. \tag{4.50}$$

Figure 4.4: Comparison of the magnitude of the induced magnetic field on the surface of a silver sphere corresponding to the first mode of energy $\hbar\omega = 3.94\,\text{eV}$ computed analytically a), and numerically b) using the MNPBEM toolbox. The energy of this mode was identified in the electron energy loss spectra in figure 2.3. The front side denotes the hemisphere facing the electron. Calculations were performed for a sphere radius $a = 1\,\text{nm}$, impact parameter $b = 1.5\,\text{nm}$ ($\phi_0 = 0$) and electrons of energy $120\,\text{keV}$. The response of silver was modelled by a Drude dielectric function with parameters from table B.1.

In the case of the electric field, the magnitude of the induced part is much larger than the magnitude of the external one. This situation is completely different for the magnetic field, where the external contribution to the total field prevails, which becomes even more evident for modes of higher energies. We demonstrate this by plotting the total fields for the first mode of energy $3.94\,\text{eV}$ in figure 4.6.

By comparison of the results in figure 4.2, a) and those in figure 4.3, we can directly see that the dominating part of the total electric field is the induced one. Magnitudes of the external [figure 4.2, b)] and induced magnetic fields (figure 4.4) are in case of the first mode similar, therefore neither external or induced part is prevailing in the total field.
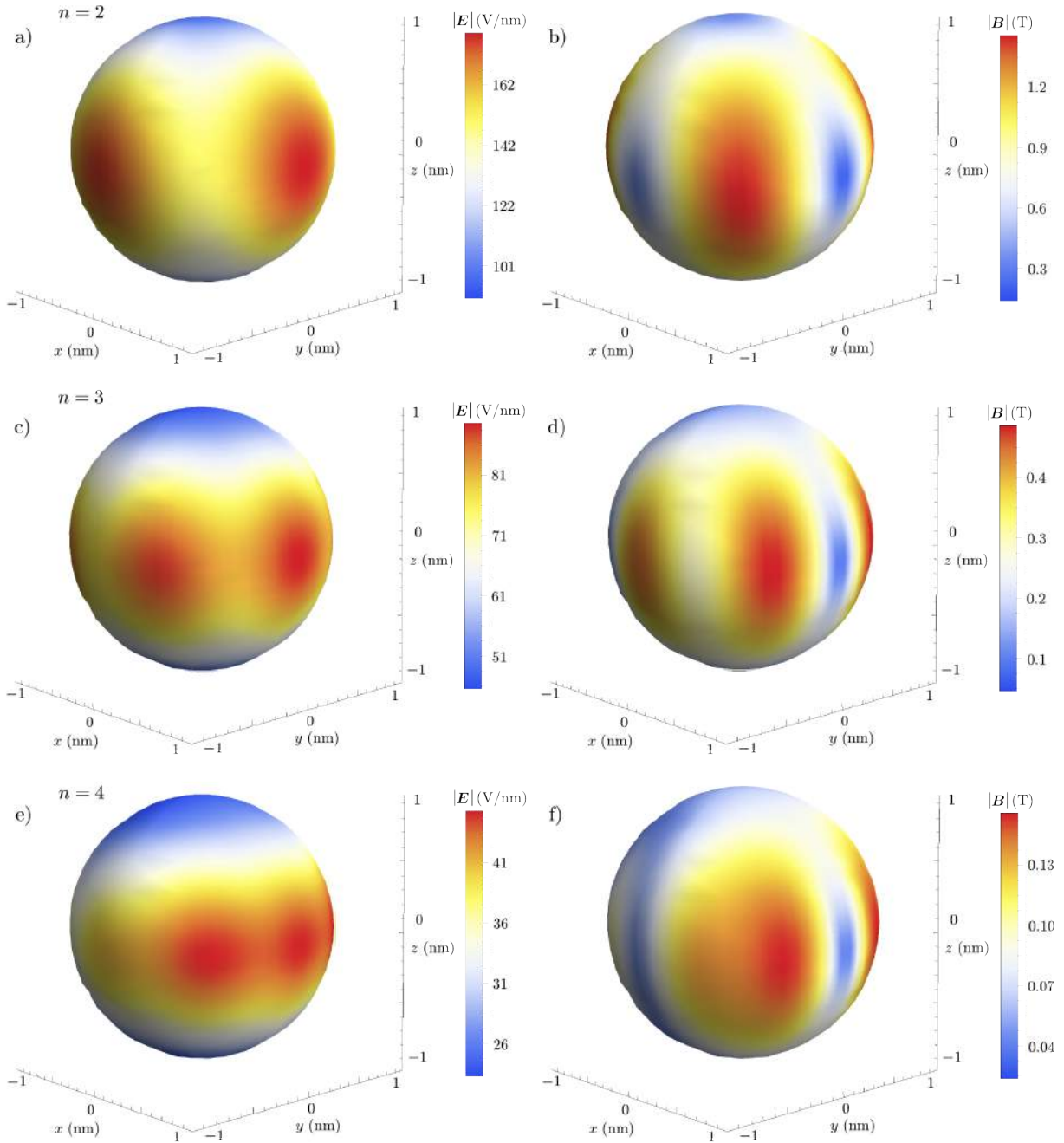
Figure 4.5: The induced fields corresponding to the higher order modes related to the marked peaks in figure 2.3. In a) electric field corresponding to the peak with energy $4.14\,\mathrm{eV}$ is depicted. Magnetic field for the same energy is visualized in b). In c) and d) we can find electric and magnetic field, respectively, plotted for the third peak of energy $4.21\,\mathrm{eV}$. Figures e) and f) are related to the last peak that can be clearly identified, whose energy is $4.25\,\mathrm{eV}$. Calculations were performed for a silver sphere with radius $a = 1\,\mathrm{nm}$, impact parameter $b = 1.5\,\mathrm{nm}$ ($\phi_0 = 0$) and electrons of energy $120\,\mathrm{keV}$. The response of silver was modelled by a Drude dielectric function with parameters from table B.1.
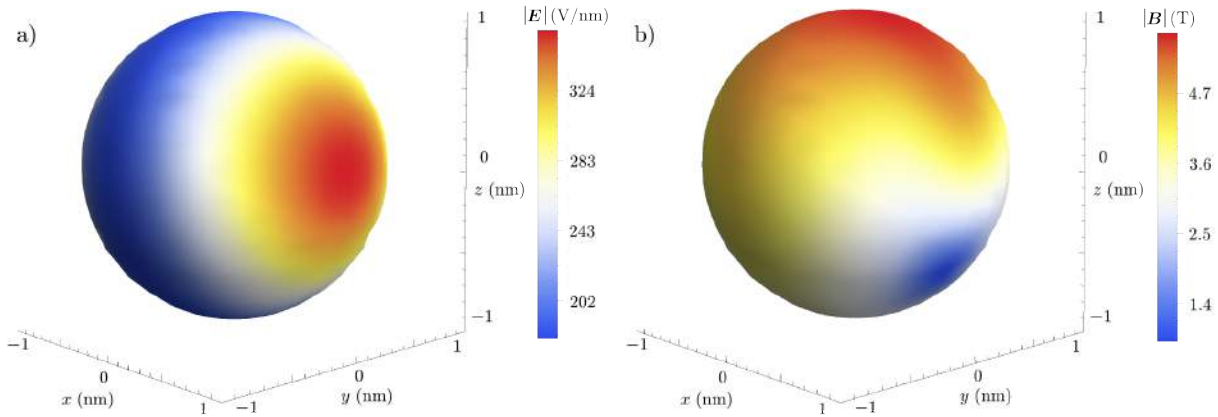
Figure 4.6: Total electric field a) and total magnetic field b) corresponding to the first mode of energy $3.94\,\text{eV}$ identified in the spectrum of figure 2.3. The fields were calculated as a superposition of incident and external fields [according to Eq. (4.50)]. By comparison with the induced fields, we can see that they dominate in the case of electric field. The total magnetic field is much more influenced by the external part. The calculation was performed for a sphere of radius $a = 1\,\text{nm}$, impact parameter $b = 1.5\,\text{nm}$ ($\phi_0 = 0$) and electrons of energy $120\,\text{keV}$.

4.4. Induced fields inside the sphere

In a way similar to the previous section, we can find the fields that are induced inside the sphere. As we require finiteness of the fields at the origin, electric and magnetic functions will be expressed with help of spherical Bessel functions as

$$\psi^{\text{M,ind,in}}(\mathbf{r}) = \sum_{n=1}^{\infty} \sum_{m=-n}^{n} \mathrm{i}^n j_n(k_{\text{in}}r) Y_{n,m}(\Omega_{\mathbf{r}}) \psi_{n,m}^{\text{M,ind,in}}, \tag{4.51}$$

$$\psi^{\text{E,ind,in}}(\mathbf{r}) = \sum_{n=1}^{\infty} \sum_{m=-n}^{n} \mathrm{i}^n j_n(k_{\text{in}}r) Y_{n,m}(\Omega_{\mathbf{r}}) \psi_{n,m}^{\text{E,ind,in}}, \tag{4.52}$$

where the coefficients of the induced field inside are again related to the coefficients of the external fields

$$\psi_{n,m}^{\text{M,ind,in}} = s_n^{\text{M}} \psi_{n,m}^{\text{M,ext}}, \tag{4.53}$$

$$\psi_{n,m}^{\text{E,ind,in}} = s_n^{\text{E}} \psi_{n,m}^{\text{E,ext}}. \tag{4.54}$$

s_n^{M} and s_n^{E} can be related to the Mie coefficients:

$$s_n^{\text{M}} = \frac{-j_n(ka)[kah_n^+(ka)]' + h_n^+(ka)[kaj_n(ka)]'}{h_n^+(ka)[k_{\text{in}}aj_n(k_{\text{in}}a)]' - j_n(k_{\text{in}}a)[kah_n^+(ka)]'}, \tag{4.55}$$

$$s_n^{\text{E}} = \frac{-j_n(ka)[kah_n^+(ka)]' + h_n^+(ka)[kaj_n(ka)]'}{h_n^+(ka)[k_{\text{in}}aj_n(k_{\text{in}}a)]' - \varepsilon_{\text{r}} j_n(k_{\text{in}}a)[kah_n^+(ka)]'}. \tag{4.56}$$

Explicit expressions for the electric field inside the sphere then read

$$
\begin{aligned}
\mathbf{E}^{\text{ind,in}}(\mathbf{r},\omega) = {} & \mathbf{e}_r \frac{-2\pi\mathrm{i}\omega}{c^2\gamma} \sum_{n=1}^{\infty} \sum_{m=-n}^{n} s_n^{\text{E}} \frac{j_n(k_{\text{in}}r)}{k_{\text{in}}r} B_{n,m} K_m\left(\frac{\omega b}{v\gamma}\right) Y_{n,m}(\theta,\phi) \exp(-\mathrm{i}m\phi_0 - \mathrm{i}\omega z_0/v) \\
& + \mathbf{e}_\theta \left\{ \frac{4\pi\mathrm{i}\omega v}{c^3} \sum_{n=1}^{\infty} \sum_{m=-n}^{n} \frac{s_n^{\text{M}} m^2}{n(n+1)\sin\theta} j_n(k_{\text{in}}r) A_{n,m}^+ K_m\left(\frac{\omega b}{v\gamma}\right) Y_{n,m}(\theta,\phi) \right. \\
& + \frac{2\pi\mathrm{i}\omega}{c^2\gamma} \sum_{n=1}^{\infty} \sum_{m=-n}^{n} \frac{s_n^{\text{E}}}{n(n+1)} B_{n,m} K_m\left(\frac{\omega b}{v\gamma}\right) \left[(n+1)\frac{j_n(k_{\text{in}}r)}{k_{\text{in}}r} - j_{n+1}(k_{\text{in}}r)\right] \\
& \times \left[\frac{(n+1)\cos\theta}{\sin\theta} Y_{n,m}(\theta,\phi) - \frac{(n-m+1)}{\sin\theta} \frac{\alpha_{n,m}}{\alpha_{n+1,m}} Y_{n+1,m}(\theta,\phi)\right] \right\} \exp(-\mathrm{i}m\phi_0 - \mathrm{i}\omega z_0/v) \\
& + \mathbf{e}_\phi \left\{ \frac{4\pi\omega v}{c^3} \sum_{n=1}^{\infty} \sum_{m=-n}^{n} \frac{s_n^{\text{M}} m}{n(n+1)} j_n(k_{\text{in}}r) A_{n,m}^+ K_m\left(\frac{\omega b}{v\gamma}\right) \right. \\
& \times \left[\frac{(n+1)\cos\theta}{\sin\theta} Y_{n,m}(\theta,\phi) - \frac{(n-m+1)}{\sin\theta} \frac{\alpha_{n,m}}{\alpha_{n+1,m}} Y_{n+1,m}(\theta,\phi)\right] \\
& + \frac{2\pi\omega}{c^2\gamma} \sum_{n=1}^{\infty} \sum_{m=-n}^{n} \frac{s_n^{\text{M}} m}{n(n+1)\sin\theta} B_{n,m} K_m\left(\frac{\omega b}{v\gamma}\right) Y_{n,m}(\theta,\phi) \\
& \times \left. \left[(n+1)\frac{j_n(k_{\text{in}}r)}{k_{\text{in}}r} - j_{n+1}(k_{\text{in}}r)\right] \right\} \exp(-\mathrm{i}m\phi_0 - \mathrm{i}\omega z_0/v).
\end{aligned}
\tag{4.57}
$$

The three components in the spherical coordinates E_r, E_θ and E_ϕ are plotted for the first two modes of energies 3.94 eV and 4.14 eV in figure 4.7.

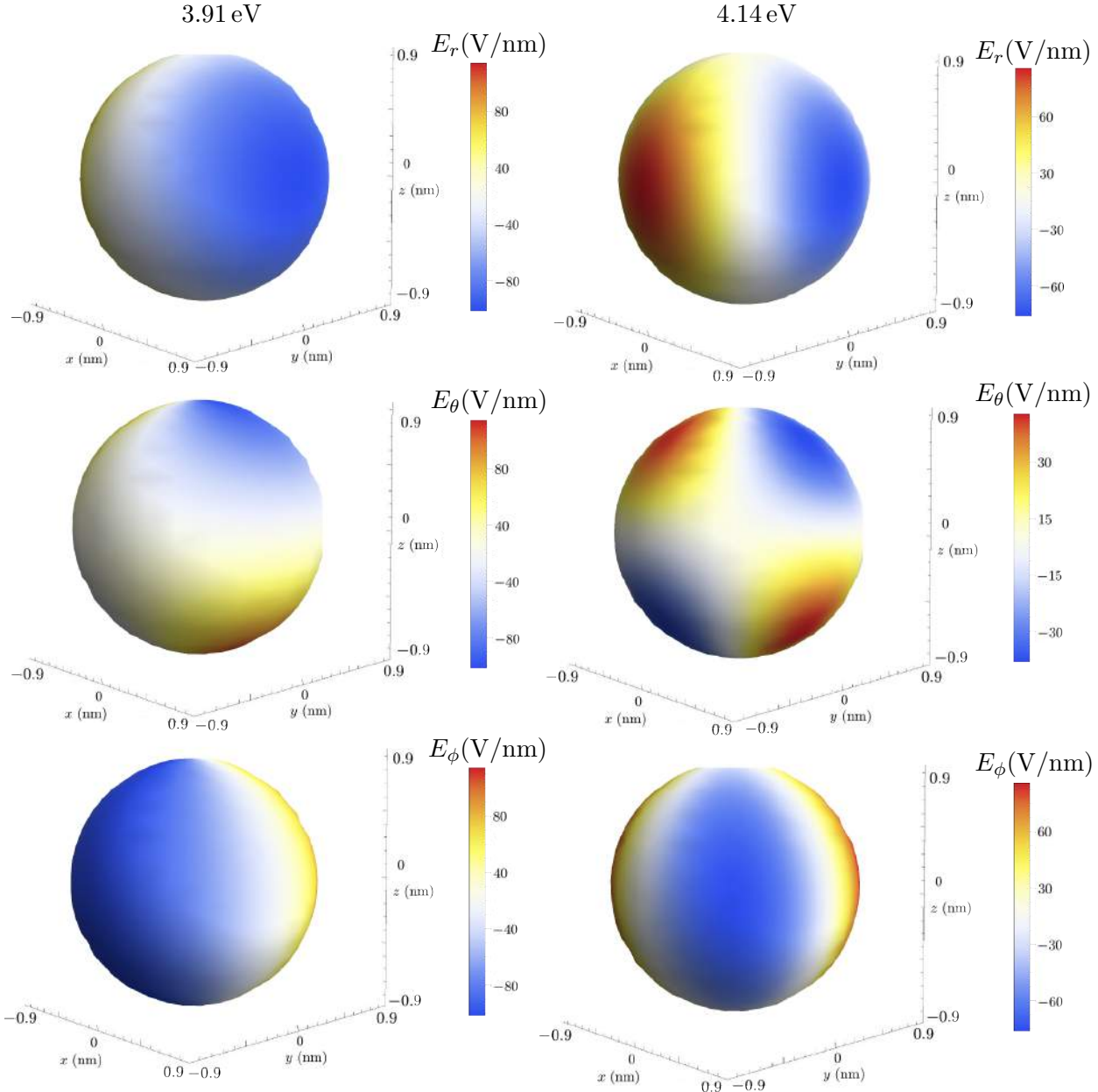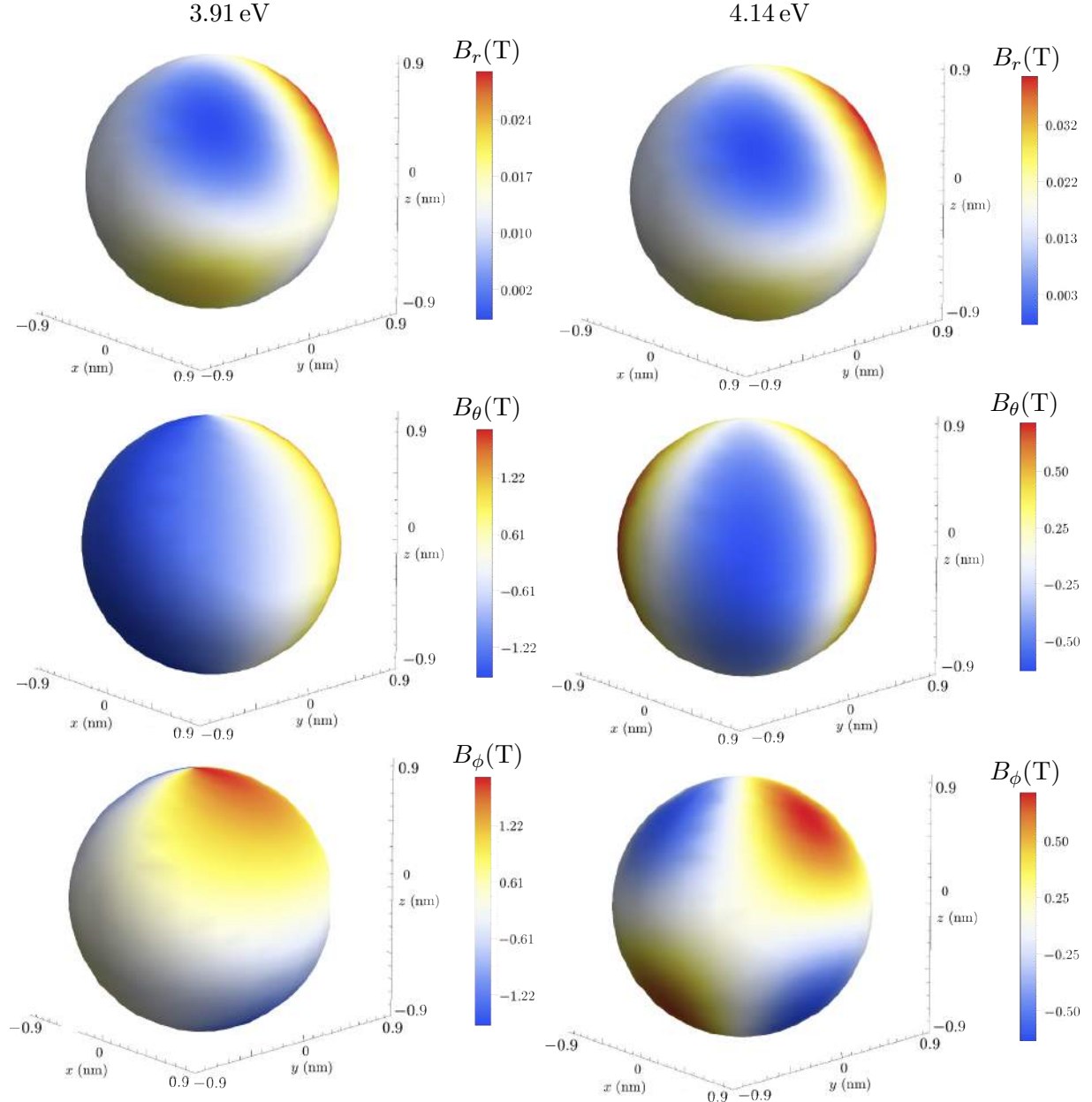
Figure 4.7: Components of the electric field $\mathbf{E} = (E_r, E_\theta, E_\phi)$ inside the sphere ($r = 0.9a = 0.9$ nm) for energies related to the first two peaks in the electron energy loss spectrum of figure 2.3: 3.94 eV (left column) and 4.14 eV (right column). We can clearly identify where the positive (red) or negative charge (blue) is accumulated.

Figure 4.8: Components of the magnetic field $\mathbf{B} = (B_r, B_\theta, B_\phi)$ inside the sphere ($r = 0.9a = 0.9\,\mathrm{nm}$) for energies related to the first two peaks in the electron energy loss spectrum of figure 2.3: $3.94\,\mathrm{eV}$ (left column) and $4.14\,\mathrm{eV}$ (right column).

The expression for the magnetic field inside the sphere is found to be

$$
\begin{aligned}
\mathbf{B}^{\mathrm{ind,in}}(\mathbf{r},\omega) = \mathbf{e}_r &\frac{-4\pi \mathrm{i}\omega v}{c^3} \sum_{n=1}^{\infty} \sum_{m=-n}^{n} s_n^{\mathrm{M}} \frac{j_n(k_{\mathrm{in}}r)}{kr} A_{n,m}^{+} K_m\left(\frac{\omega b}{v\gamma}\right) Y_{n,m}(\theta,\phi) \exp(-\mathrm{i}m\phi_0 - \mathrm{i}\omega z_0/v) \\
&+ \mathbf{e}_\theta \left\{ \frac{-2\pi \mathrm{i}\omega}{c^2\gamma} \sum_{n=1}^{\infty} \sum_{m=-n}^{n} \frac{s_n^{\mathrm{E}} m}{n(n+1)\sin\theta} j_n(k_{\mathrm{in}}r) B_{n,m} K_m\left(\frac{\omega b}{v\gamma}\right) Y_{n,m}(\theta,\phi) \right. \\
&+ \frac{4\pi \mathrm{i}\omega v}{c^3} \sum_{n=1}^{\infty} \sum_{m=-n}^{n} \frac{s_n^{\mathrm{M}} m}{n(n+1)} A_{n,m}^{+} K_m\left(\frac{\omega b}{v\gamma}\right) \left[(n+1)\frac{j_n(k_{\mathrm{in}}r)}{k_{\mathrm{in}}r} - j_{n+1}(k_{\mathrm{in}}r) \right] \\
&\times \left. \left[\frac{(n+1)\cos\theta}{\sin\theta} Y_{n,m}(\theta,\phi) - \frac{(n-m+1)}{\sin\theta} \frac{\alpha_{n,m}}{\alpha_{n+1,m}} Y_{n+1,m}(\theta,\phi) \right] \right\} \exp(-\mathrm{i}m\phi_0 - \mathrm{i}\omega z_0/v) \\
&- \mathbf{e}_\phi \left\{ \frac{2\pi\omega}{c^2\gamma} \sum_{n=1}^{\infty} \sum_{m=-n}^{n} s_n^{\mathrm{E}} \frac{B_{n,m}}{n(n+1)} j_n(k_{\mathrm{in}}r) K_m\left(\frac{\omega b}{v\gamma}\right) \right. \\
&\times \left[\frac{(n+1)\cos\theta}{\sin\theta} Y_{n,m}(\theta,\phi) - \frac{(n-m+1)}{\sin\theta} \frac{\alpha_{n,m}}{\alpha_{n+1,m}} Y_{n+1,m}(\theta,\phi) \right] \\
&- \frac{4\pi\omega v}{c^3} \sum_{n=1}^{\infty} \sum_{m=-n}^{n} \frac{s_n^{\mathrm{M}} m^2}{n(n+1)\sin\theta} A_{n,m}^{+} K_m\left(\frac{\omega b}{v\gamma}\right) Y_{n,m}(\theta,\phi) \\
&\times \left. \left[(n+1)\frac{j_n(k_{\mathrm{in}}r)}{k_{\mathrm{in}}r} - j_{n+1}(k_{\mathrm{in}}r) \right] \right\} \exp(-\mathrm{i}m\phi_0 - \mathrm{i}\omega z_0/v),
\end{aligned}
$$
(4.58)

which is plotted for the first two modes in figure 4.8.

4.5. Energy loss probability

Since we know the induced fields acting back on the moving electron, it is possible to calculate the loss probability Γ_{EELS} according to Eq. (2.22). When we substitute there the induced field, we obtain

$$
\Gamma_{\mathrm{EELS}}(\omega) = \frac{1}{\pi\omega} \int_{-\infty}^{\infty} \mathrm{Re}\left[\mathbf{v} \cdot \left(\mathbf{L}\psi^{\mathrm{M,ind}} - \frac{\mathrm{i}}{k} \nabla \times \mathbf{L}\psi^{\mathrm{E,ind}} \right) \exp(-\mathrm{i}\omega t) \right] \mathrm{d}t,
$$
(4.59)

where we used atomic units. Contribution of both magnetic and electric modes can be obtained by the appropriate substitutions that were performed in [20]. The loss probability related to the magnetic modes then reads

$$
\Gamma_{\mathrm{EELS}}^{\mathrm{M}}(\omega) = \sum_{n=1}^{\infty} \sum_{m=-n}^{n} \frac{mv}{\pi\omega^2} K_m\left(\frac{\omega b}{v\gamma}\right) \mathrm{Re}\left[(A_{n,m}^{+})^* \exp(\mathrm{i}m\phi_0 + \mathrm{i}\omega z_0/v) \mathrm{i}^{-n} \psi_{n,m}^{\mathrm{M,ind}} \right],
$$
(4.60)

while the loss probability due to the electric modes is expressed as

$$
\Gamma_{\mathrm{EELS}}^{\mathrm{E}}(\omega) = \sum_{n=1}^{\infty} \sum_{m=-n}^{n} \frac{c}{2\pi\omega^2\gamma} K_m\left(\frac{\omega b}{v\gamma}\right) \mathrm{Re}\left[(B_{n,m}^{+})^* \exp(\mathrm{i}m\phi_0 + \mathrm{i}\omega z_0/v) \mathrm{i}^{-n} \psi_{n,m}^{\mathrm{E,ind}} \right].
$$
(4.61)

Now we can write down the total loss probability in SI units:

$$\Gamma_{\text{EELS}} = \Gamma_{\text{EELS}}^{\text{M}} + \Gamma_{\text{EELS}}^{\text{E}} = \frac{e^2}{c\hbar\omega} \sum_{n=1}^{\infty} \sum_{m=-n}^{n} K_m^2 \left(\frac{\omega b}{v\gamma}\right) \left[C_{n,m}^{\text{M}} \text{Im}[t_n^{\text{M}}] + C_{n,m}^{\text{E}} \text{Im}[t_n^{\text{E}}] \right], \qquad (4.62)$$

where we define the coefficients

$$C_{n,m}^{\text{M}} = \frac{n}{n+1} \left| \frac{2mn}{c} A_{n,m}^{+} \right|^2 \qquad C_{n,m}^{\text{E}} = \frac{n}{n+1} \left| \frac{1}{\gamma} B_{n,m} \right|^2. \qquad (4.63)$$

The dependence of the loss probability on ω for an electron moving in vacuum is except of occurrence in denominator and in argument of modified Bessel function contained in coefficients t_n^{E} and t_n^{M}. It is hidden there in dielectric function, which appears in k_{in}.

In figures 4.9 and 4.10 we can compare the electron energy loss probability calculated according to the analytical relations (4.62) and (2.28) with the values obtained from the MNPBEM software. The theoretical loss functions were obtained for a maximum value of index $n_{\text{max}} = 20$. We again studied the case of a sphere with radius $a = 1\,\text{nm}$ and electron with energy $120\,\text{keV}$ moving at an impact parameter $b = 1.5\,\text{nm}$ and crossing the x axis.

In figure 4.9, EEL spectra are plotted for the silver sphere, whereas the spectrum in figure 4.10 was calculated for a sphere made of gold. In both cases the material properties were modelled by Drude dielectric function (details can be found in Appendix B) and we can see that the energy loss obtained from the retarded solution cannot be distinguished from the nonretarded one, as the sphere is very small and electromagnetic retardation does not have significant influence.

The apparent difference between the spectra calculated for silver and gold spheres is in the separation between the peaks. In the former, the first four peaks can be easily distinguished and identified. In the latter spectra, peaks corresponding to all higher order modes are hidden in the right part of the first peak. Although the highest possible number of surface elements was used for BEM calculation, we can see that the results are slightly different. This can be explained not only due to the finite discretization in the case of numerical results, which can cause deviation, but we also have to realize that our analytical calculations were made in the limit $kr \to 0$ and that we sum over a finite number of modes, $n_{\text{max}} = 20$.
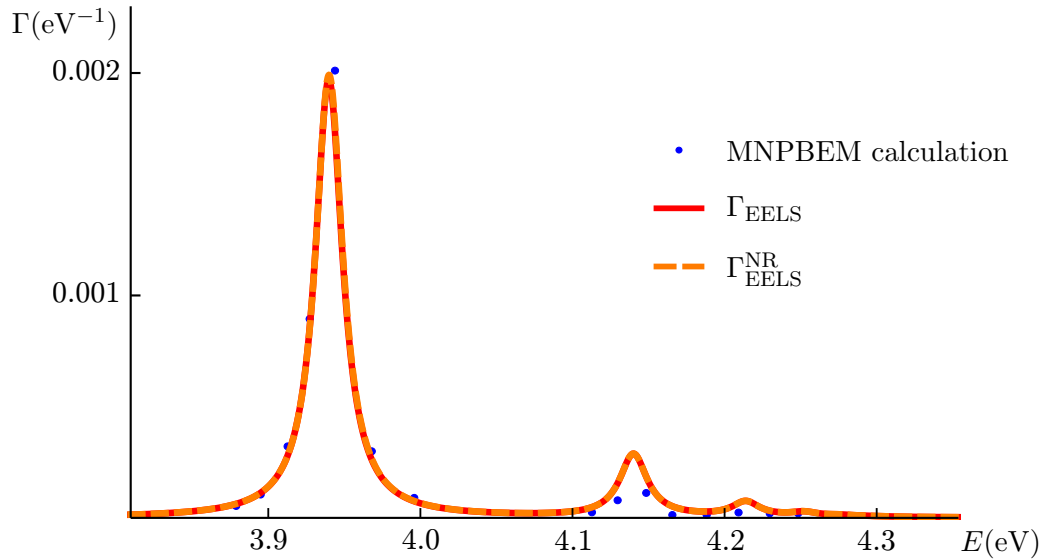
Figure 4.9: Electron energy loss calculated for a silver sphere of radius $a = 1\,\text{nm}$ and electrons with energy $120\,\text{keV}$ moving at an impact parameter $b = 1.5\,\text{nm}$ (with $\phi_0 = 0$). The red curve represents loss probability [according to Eq. (4.62)] including retardation. The orange dashed curve, which is hardly distinguishable from the retarded solution, corresponds to the nonretarded approximation [according to Eq. (2.28)]. For the MNPBEM calculation 1444 elements were used to create the surface of the sphere. Results are marked by blue points.
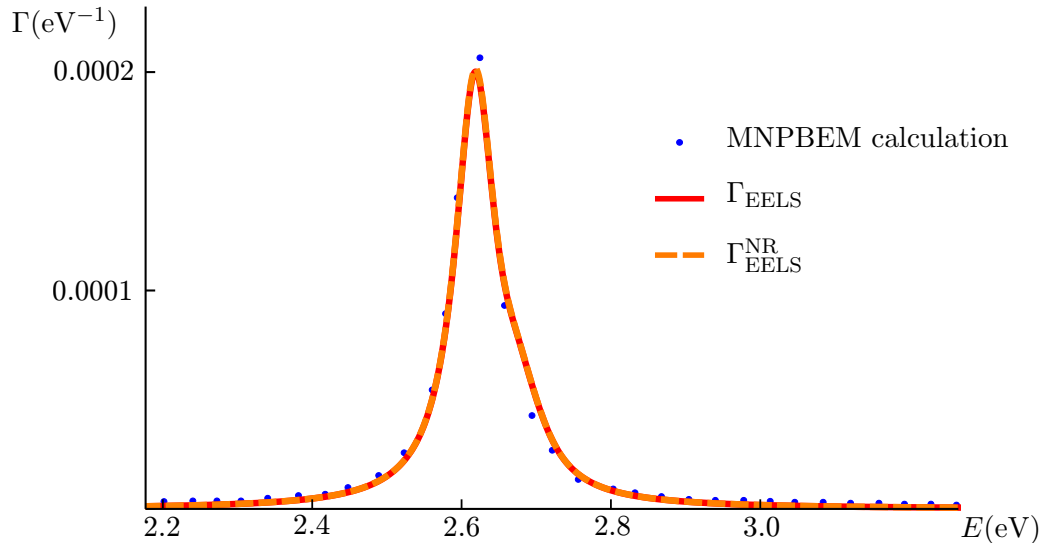
Figure 4.10: Electron energy loss calculated for a gold sphere of radius $a = 1\,\text{nm}$ and electrons with energy $120\,\text{keV}$ moving at an impact parameter $b = 1.5\,\text{nm}$ (with $\phi_0 = 0$). The red curve represents loss probability [according to Eq. (4.62)] including retardation. The orange dashed curve, which is hardly distinguishable from the retarded solution, corresponds to the nonretarded approximation [according to Eq. (2.28)]. For the MNPBEM calculation 1444 elements were used to create the surface of the sphere. Results are marked by blue points.

5. Evolution of electromagnetic fields in time domain

We present in this chapter the study of the dynamics of the electromagnetic fields as a result of the interaction with the electron. To that end, we employ the Fourier transform defined in Appendix A and use the properties of Fourier transformation of a real function. The integral transform of the fields then takes the form:

$$\mathbf{E}(\mathbf{r},t) = \frac{1}{\pi} \int_0^\infty \mathrm{Re}\left[\mathbf{E}(\mathbf{r},\omega)\exp(-\mathrm{i}\omega t)\right] \mathrm{d}\omega \qquad \text{and} \qquad \mathbf{B}(\mathbf{r},t) = \frac{1}{\pi} \int_0^\infty \mathrm{Re}\left[\mathbf{B}(\mathbf{r},\omega)\exp(-\mathrm{i}\omega t)\right] \mathrm{d}\omega. \quad (5.1)$$

The integrals in Eq. (5.1) can be calculated numerically at a particular time t in any point of space. In this case we are interested in the fields occurring just above the surface of the particle especially in times when the passing electron is in the close proximity of the particle (attoseconds) and then in times corresponding to the oscillation of localized surface plasmons (femtoseconds).

In the following we set $z_0 = 0$ and $\phi_0 = 0$, which means that in time $t = 0\,\mathrm{s}$ the electron is situated in position $\mathbf{r}_\mathrm{t}(t=0) = (b,0,0)$ (see the figure 4.1). For all calculations a very small silver sphere of radius $a = 1\,\mathrm{nm}$ was considered, we used impact parameter $b = 1.5\,\mathrm{nm}$ and assumed an electron of energy $120\,\mathrm{keV}$ (velocity $v = 0.587c$). This means that the electron is in close proximity to the nanoparticle in times corresponding to units of attoseconds. The localized plasmon response will appear in femtoseconds when the electron is relatively far from the sphere. The latter is related to the response function of the material. We use the Drude dielectric function introduced in Appendix B with parameters taken from table B.1, but we set $\varepsilon_\infty = 1$. All the following results were obtained for $n_\mathrm{max} = 5$.

5.1. Exact analytical solution for the external field

Before we start to deal with the results computed by Fourier transformation of the total fields obtained from the multipolar expansion introduced in the previous chapter, we show the exact analytical solution for the time dependent field produced by a moving electron. In section 2.1 we derived this field in frequency domain, but it is possible to obtain the expressions for the field in real time. In the rest frame of our relativistic electron, there appears only the coulombic electric field of the form

$$\mathbf{E}'(\mathbf{r}') = -\frac{e}{4\pi\varepsilon_0} \frac{(\mathbf{r}' - \mathbf{r}'_\mathrm{e})}{|\mathbf{r}' - \mathbf{r}'_\mathrm{e}|^3}, \tag{5.2}$$

where $\mathbf{r}'$ and $\mathbf{r}'_\mathrm{e}$ are positions of observation point and electron, respectively, in the electron rest frame. In the case of an electron travelling along the positive z direction, Eq. (5.2) can be transformed to laboratory rest frame with use of Cartesian coordinates $\mathbf{r} = (x,y,z)$ as

$$\mathbf{E}(\mathbf{r},t) = (E_x(\mathbf{r},t), E_y(\mathbf{r},t), E_z(\mathbf{r},t)) = -\frac{e}{4\pi\varepsilon_0} \frac{\gamma}{[x^2 + y^2 + \gamma^2(z-vt)^2]^3}(x,y,z-vt), \tag{5.3}$$

$$\mathbf{B}(\mathbf{r},t) = (B_x(\mathbf{r},t), B_y(\mathbf{r},t), B_z(\mathbf{r},t)) = \frac{e}{4\pi\varepsilon_0} \frac{\gamma^2\beta}{c\,[x^2 + y^2 + \gamma^2(z-vt)^2]^3}(y,-x,0), \tag{5.4}$$

where we can observe not only the electric, but also the magnetic field. If we assume the same geometry as in figure 4.1 and perform the change $x \to x - b$ we can then project these external fields on the spherical surface within the laboratory rest frame. It is useful to compare the result from this expressions with those obtained from time-transformed multipolar expansion in Eqs. (4.40) and (4.41), which should give the same resulting fields.

The magnitudes of the electric and the magnetic field in Eqs. (5.3) and (5.4) projected on the spherical surface with radius $r = 1 \, \mathrm{nm}$ are plotted for times $-6 \, \mathrm{as}$ and $2 \, \mathrm{as}$ in figure 5.1. We can observe that as the electron is coming closer to the sphere (its position is marked by a small red sphere with a red arrow), the magnitudes are getting larger and the patterns are also changing. In general, the pattern of the field is elliptically shaped, which is due to the influence of the Lorentz contraction factor γ.
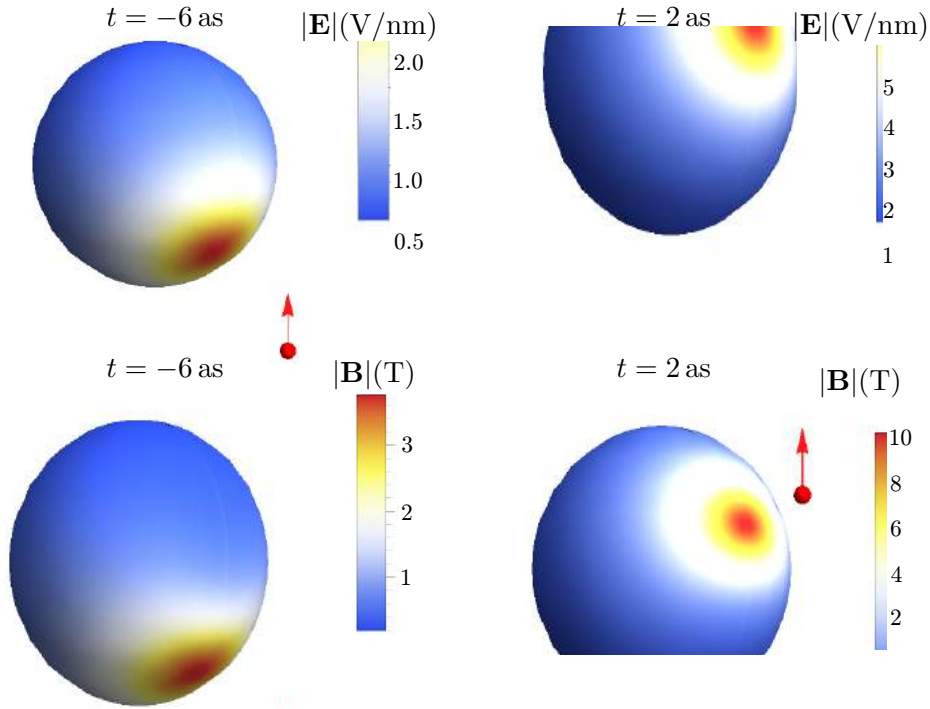
Figure 5.1: Exact analytical calculation of $|\mathbf{E}|$ (upper row) and $|\mathbf{B}|$ (lower row) produced by a moving electron projected on a spherical surface with radius $a = 1 \, \mathrm{nm}$ at times $-6 \, \mathrm{as}$ (left column) and $2 \, \mathrm{as}$ (right column). We can observe an increase in the magnitude of the fields as the electron is gets closer to the particle and also a change in patterns produced.

5.2. Fields in the attosecond regime

In attosecond times the electron is moving in close proximity to the metal sphere and the external field influencing the sphere is therefore very large. However, at this time scale the material does not have enough time to respond – when we calculate the period corresponding to the plasma frequency, for silver we get $\approx 0.5 \, \mathrm{fs}$. In attoseconds the induced fields could be only due to the response to external fields that were surrounding the particle femtoseconds before, but at those times the electron was very far and the external fields were weak. For this reason, the main contribution to the total fields on the sphere during the attosecond regime should consist of external fields.

In figure 5.2 we plot the external fields from Eqs. (4.40) and (4.41) just above the spherical surface for times -6 as and 2 as. When we compare them with the external field obtained from the exact analytical solution in figure 5.1, we can see that they are qualitatively similar and for time $t = -6$ as the magnitude of the fields fits very well. At $t = 2$ as the exactly calculated fields are more "squeezed" and their magnitude is bigger than in case of the fields calculated from the multipole expansion. This difference arises from fact that we had to use a finite number of multipoles, in this calculation $n_{\max} = 5$. Although more multipoles should be used especially for times of the closest approach of the electron to the particle, we believe that $n_{\max} = 5$ is enough to give a reasonable insight.
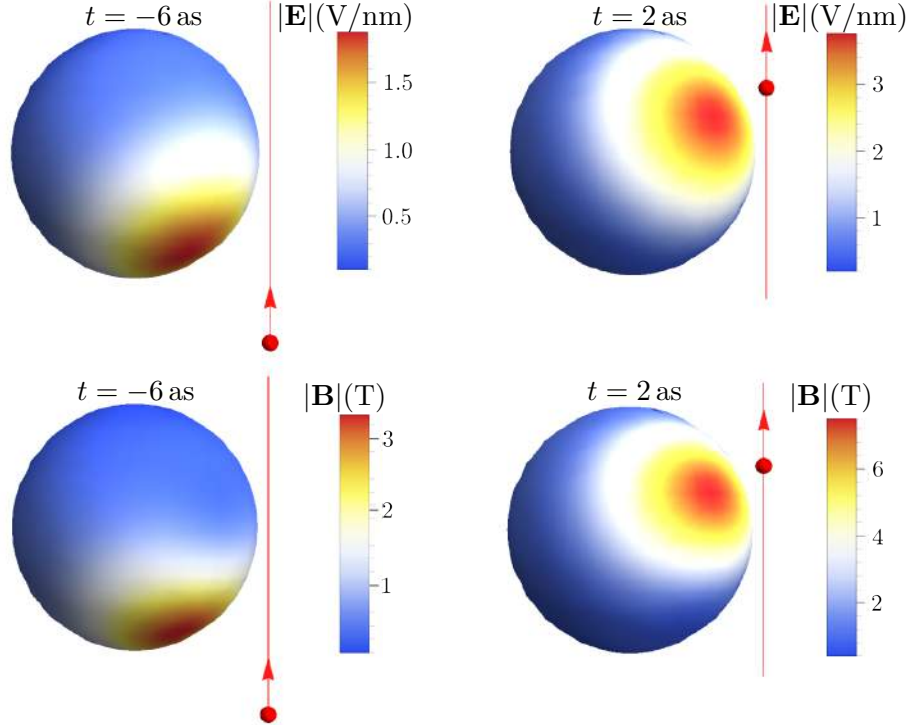
Figure 5.2: External fields expressed in Eqs. (4.40) and (4.41) obtained from the multipole expansion plotted above the surface of sphere with radius $a = 1$ nm. In the upper row, $|\mathbf{E}|$ is plotted, while in the lower row $|\mathbf{B}|$ can be seen. The fields were calculated at times -6 as (left column) and 2 as (right column).

We can compare now the external fields in figure 5.2 with the total fields from Eq. (4.50) calculated by the multipole expansion. In figure 5.3 we plot them for time sequences from -3 as to 3 as. We can clearly see that the fields follow the trajectory of electron. When we compare their magnitude for time $t = 2$ as with the external fields in figure 5.2, we can see that it is almost equal. Induced fields from Eq. (4.48) and (4.49) therefore provide only a small contribution (10^{-2} V/nm in case of the induced electric field and 10^{-3} T corresponding to the induced magnetic field) as expected because of the insufficient time for the material to respond.
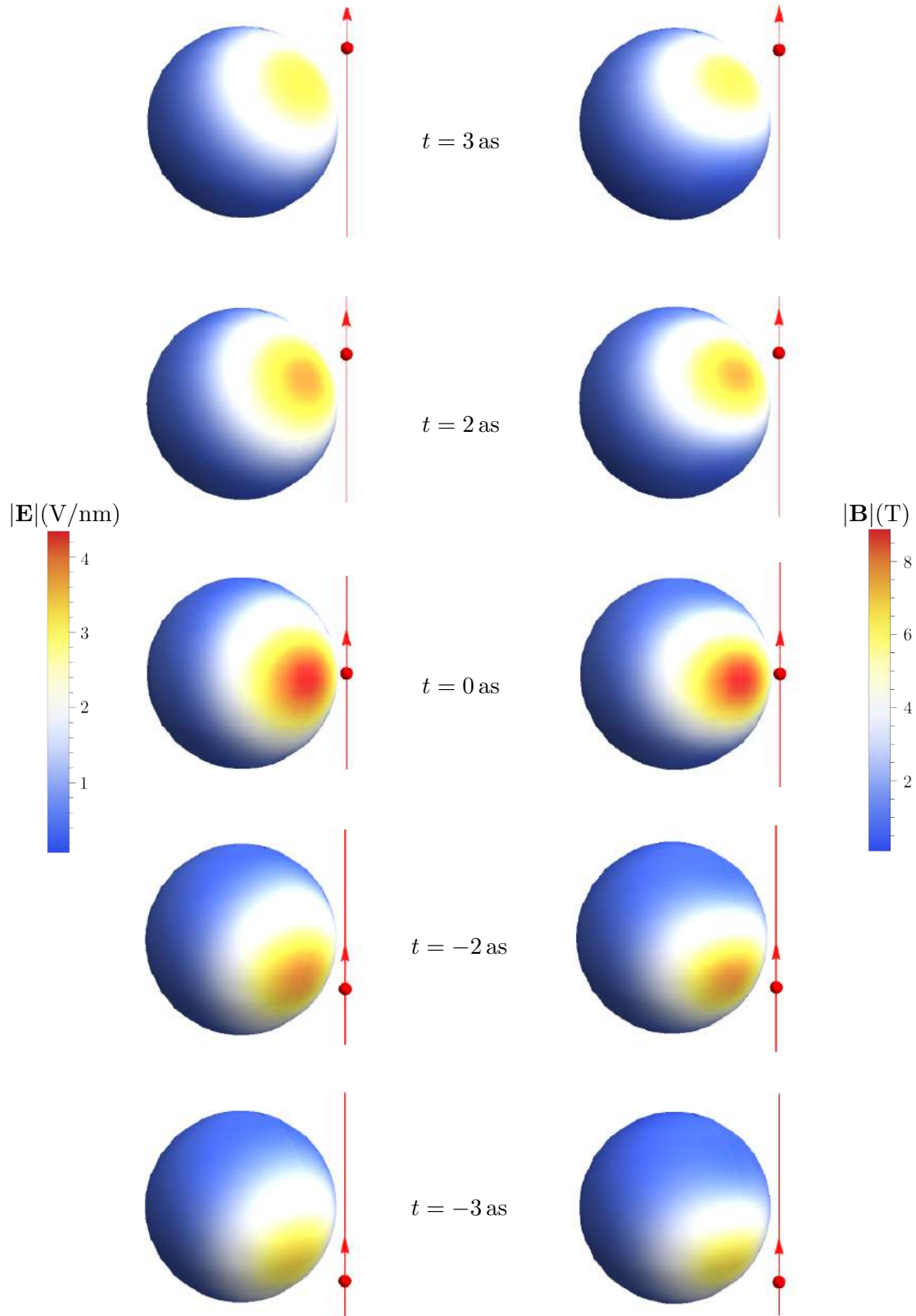
Figure 5.3: Attosecond time evolution of the total fields calculated from the multipole expansion just above the surface of the silver sphere with radius $a = 1\,\mathrm{nm}$. $|\mathbf{E}^{\mathrm{tot}}|$ is depicted in the left column, whereas in the right column $|\mathbf{B}^{\mathrm{tot}}|$ is visualized. The corresponding position of the electron at each time is marked by a small red sphere with an arrow.

5.3. Fields in the femtosecond regime

During femtoseconds after the electron flyby, the metallic sphere should respond to the strong external fields that were in its surroundings when the electron was passing by (in attoseconds). The situation is now completely different: the induced fields should be dominant, because the electron is very far and the external fields are weak. In figures 5.4 and 5.5 the electric and magnetic fields are depicted. We can see that they are weaker than in the attosecond regime, especially the magnetic field, however, the contribution of the induced parts is much larger.

We can also observe the expected oscillatory and damped character of the induced electric and magnetic field, respectively, which is typical for localized surface plasmon resonances. At some times (e.g. 0.1 fs or 0.5 fs) dipolar patterns can be observed, but a combination of higher order modes is generally present. At 6 fs it seems that quadrupolar mode is prevailing (compare with figures 4.3 and 4.4 showing the dipolar mode in frequency domain and with the plots of higher modes in figure 4.5).

$t = 0.1\,\text{fs}$

$t = 0.3\,\text{fs}$

$t = 0.5\,\text{fs}$

$t = 1.0\,\text{fs}$

$t = 1.5\,\text{fs}$

$t = 2.0\,\text{fs}$

$t = 2.5\,\text{fs}$

$t = 3.0\,\text{fs}$

$t = 3.5\,\text{fs}$

$t = 4.0\,\text{fs}$

$t = 5.0\,\text{fs}$

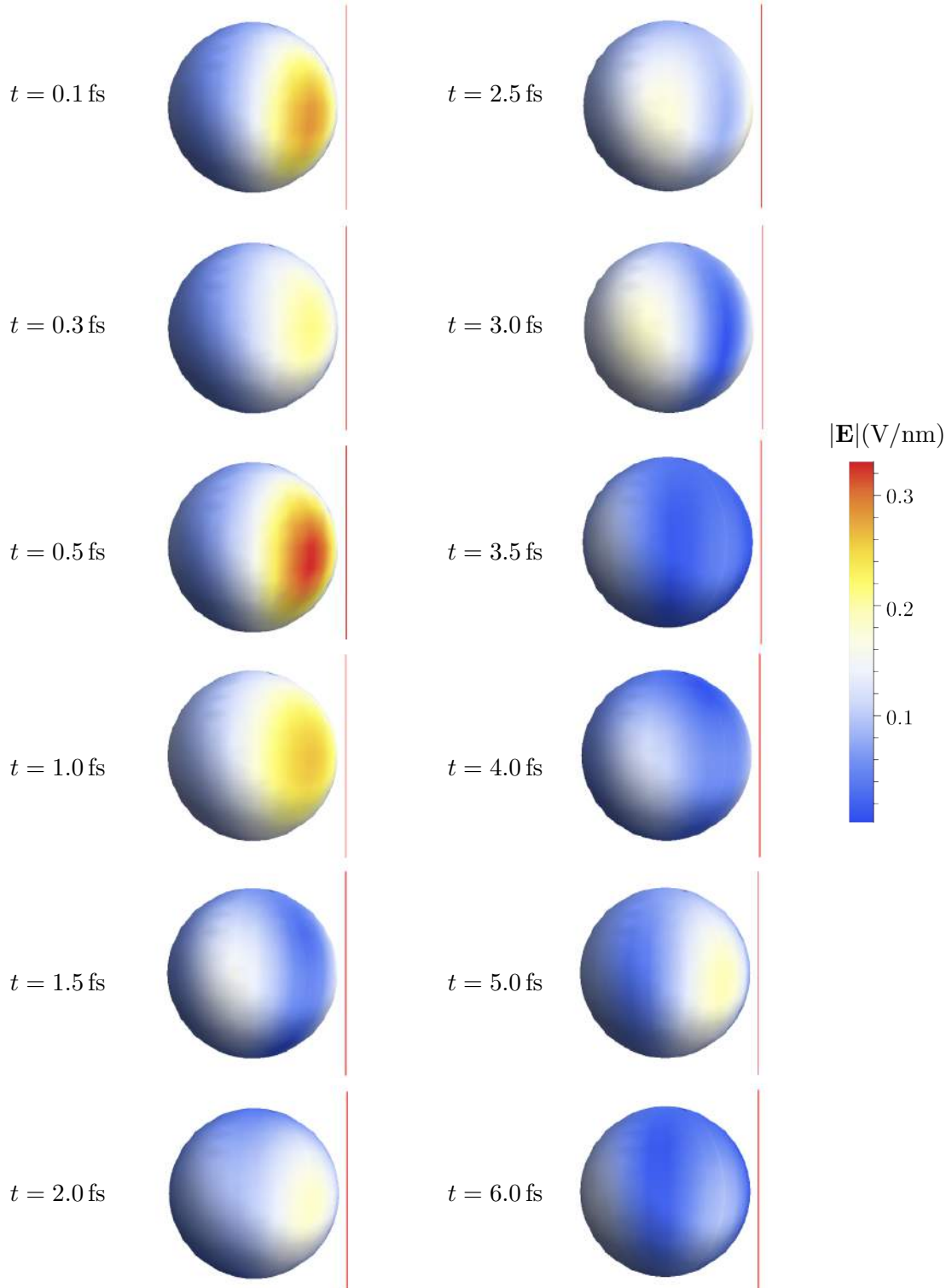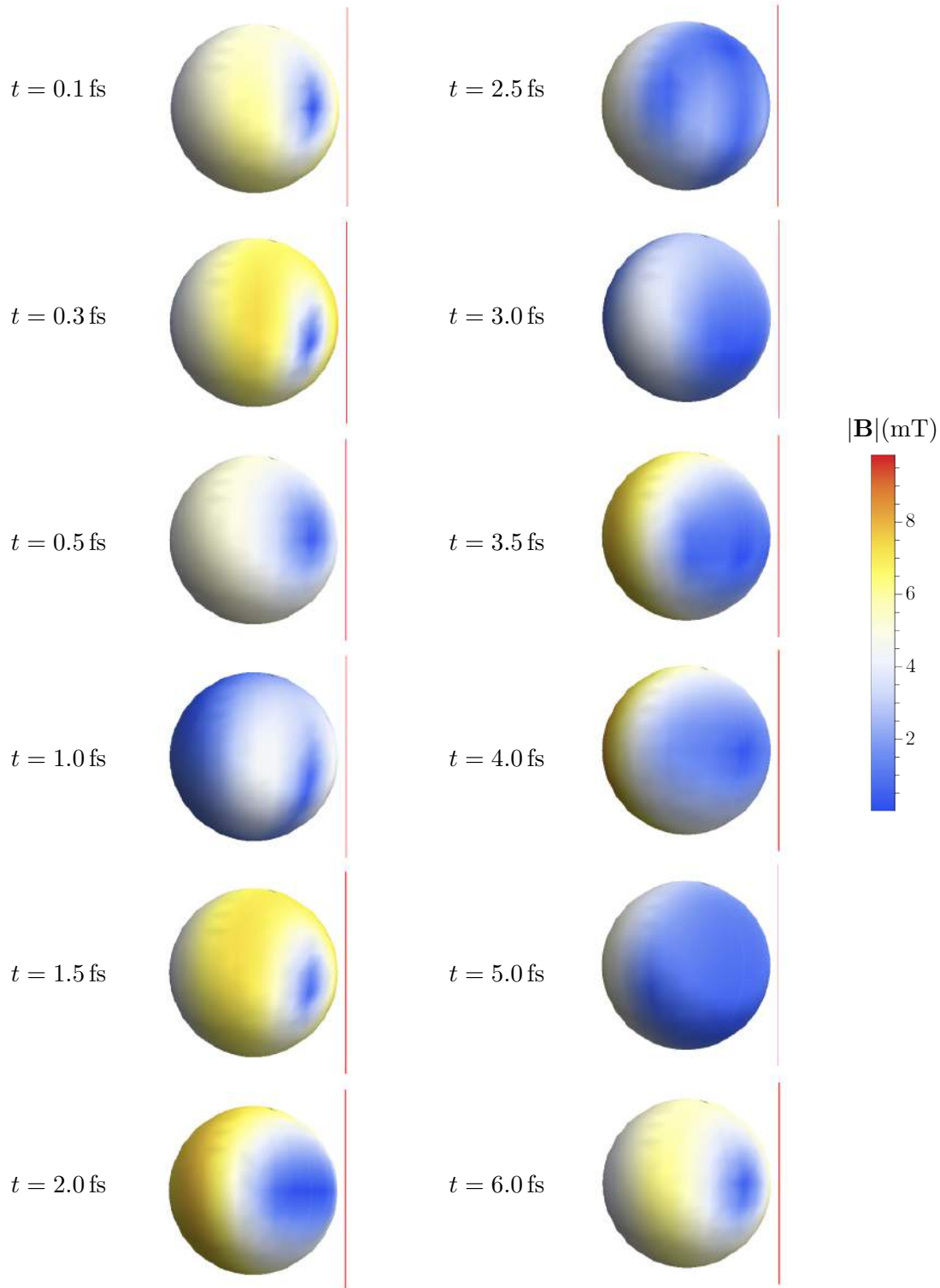$t = 6.0\,\text{fs}$

$|\mathbf{E}|(\text{V/nm})$

0.3

0.2

0.1

Figure 5.4: Evolution of electric field $|\mathbf{E}|$ during femtoseconds after the electron passed the sphere. The corresponding times are displayed on the left of each sphere. The red line represents the trajectory of the electron, which is far away from the sphere for these femtosecond times.

Figure 5.5: Evolution of magnetic field $|\mathbf{B}|$ during femtoseconds after the electron passed the sphere. The corresponding times are displayed on the left of each sphere. The red line represents the trajectory of the electron, which is far away from the sphere at the femtosecond times represented here.

6. Forces acting on a metallic sphere in time domain

The motivation of our study is connected with the phenomena depicted in figure 6.1, where we can see a sequence of scanning transmission electron microscope (STEM) images related to two different regimes of manipulation of a small spherical nanoparticle [7]. In the upper row the sphere is pulled by the electron beam, which means that it is moving towards it. The movement recorded in the lower row is completely reversed – the particle is repelled when smaller impact parameter is used. This ambiguous behaviour is not so easy to explain, because according to the image charge concept, the particle should be always attracted towards the electron. We aim to throw light on this process by exploiting the knowledge acquired on the fields from previous sections.
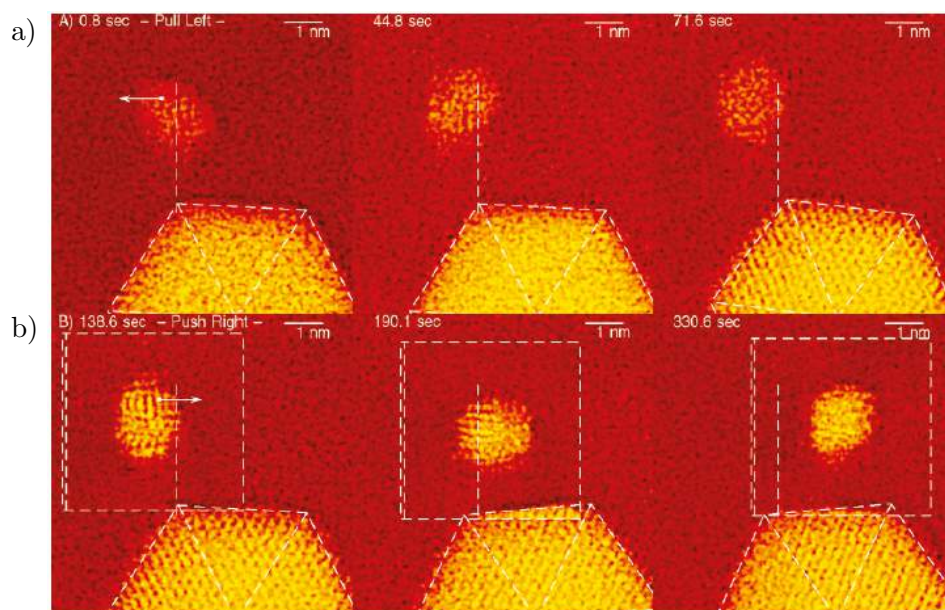

Figure 6.1: Demonstration of manipulation of a small gold nanoparticle of diameter 1.5 nm in STEM. In the upper part a) three images correspond to a "pulling" mechanism, which occurred at impact parameter $b \approx 4.5$ nm. Images labeled by b) shows "pushing" of the particle, which takes place when small impact parameters are used, $b \approx 1$ nm in this case. The time delay between the images is ≈ 40 s. Reproduced from [7].

A possible explanation of this effect was proposed in [47], where the repulsion is claimed to be connected with more effective excitation of higher order modes when the electron impact parameter is very small. On the contrary, attractive force acts on the particle in case of larger impact parameters. This is demonstrated in the inset of figure 6.2 where we can directly see the reversal of the total transversal momentum component for an impact parameter of ≈ 2 nm with respect to the sphere center. In the main part of the figure the frequency dependence of the transverse momentum component is plotted for different impact parameters with respect to the aluminium sphere of 1 nm radius.
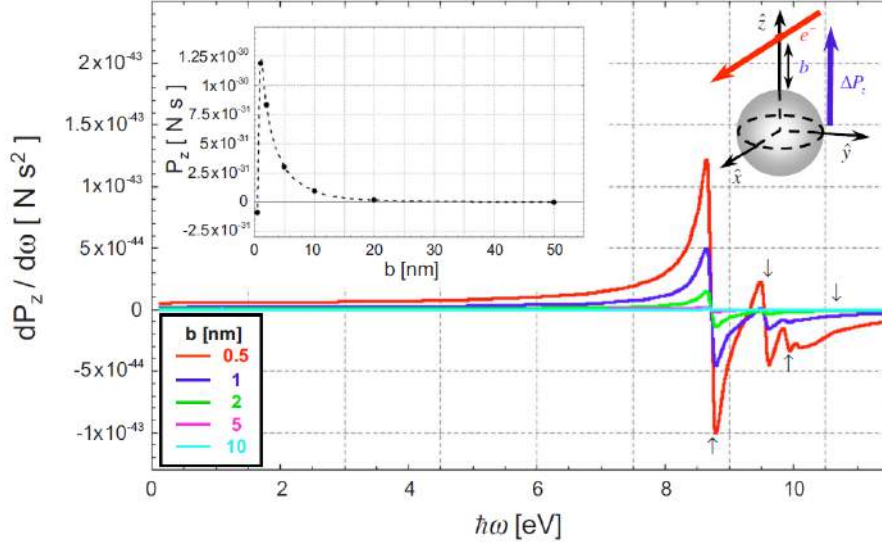
Figure 6.2: Frequency dependence of the transverse momentum component for different impact parameters for the case of a 1 nm aluminium sphere described by a Drude dielectric function. In the inset the dependence of the total force integrated over all frequencies on impact parameter is shown, where we can see reversal of the total transversal momentum component for small impact parameters. When we use impact parameters > 2 nm (measured from the sphere center), the transverse momentum corresponding to the motion in the plane parallel to the substrate is always positive and it is decaying to zero as we move the electron beam away. The plot is reproduced from ref. [47].

6.1. Numerical procedure

As we pointed out in the first chapter, the time derivative of the mechanical momentum plus the momentum of electromagnetic field can be obtained from a surface integration of Maxwell stress tensor [Eq. (1.45)]. Once we have the transformed components of the total fields outside the particle, Maxwell stress tensor Eq. (1.44) in real time can be easily calculated for a surface tightly enclosing the particle. The Fourier transform of the fields is performed numerically, therefore we calculate the fields only at particular points near the surface of the sphere and the integration is performed as a discrete summation.

First we have to construct the Maxwell stress tensor [Eq. (1.44)] containing the components of the fields outside $\mathbf{E}^{\text{out}}(\mathbf{r}, t) = (E_x(\mathbf{r}, t), E_y(\mathbf{r}, t), E_z(\mathbf{r}, t))$ and $\mathbf{B}^{\text{out}}(\mathbf{r}, t) = (B_x(\mathbf{r}, t), B_y(\mathbf{r}, t), B_z(\mathbf{r}, t))$. Then we have to perform the matrix multiplication by the normal surface element. If we split the Maxwell stress tensor in two parts $\overleftrightarrow{\mathbf{T}}_{\mathbf{E}}$ and $\overleftrightarrow{\mathbf{T}}_{\mathbf{B}}$ related to contribution of electric and magnetic fields, respectively, it can be written as

$$\overleftrightarrow{\mathbf{T}}_{\mathbf{E}} \cdot \mathbf{n}\Delta S = \Delta S \varepsilon_0 \begin{pmatrix} \frac{1}{2}(E_x^2 - E_y^2 - E_z^2) & E_x E_y & E_x E_z \\ E_y E_x & \frac{1}{2}(E_y^2 - E_x^2 - E_z^2) & E_y E_z \\ E_z E_x & E_z E_y & \frac{1}{2}(E_z^2 - E_x^2 - E_y^2) \end{pmatrix} \cdot \begin{pmatrix} \sin(\theta)\cos(\phi) \\ \sin(\theta)\sin(\phi) \\ \cos(\phi) \end{pmatrix},$$

(6.1)

$$\overleftrightarrow{\mathbf{T}}_{\mathbf{B}}\cdot\mathbf{n}\Delta S = \Delta S \varepsilon_0 c^2 \begin{pmatrix} \frac{1}{2}(B_x^2 - B_y^2 - B_z^2) & B_x B_y & B_x B_z \\ B_y B_x & \frac{1}{2}(B_y^2 - B_x^2 - B_z^2) & B_y B_z \\ B_z B_x & B_z B_y & \frac{1}{2}(B_z^2 - B_x^2 - B_y^2) \end{pmatrix} \cdot \begin{pmatrix} \sin(\theta)\cos(\phi) \\ \sin(\theta)\sin(\phi) \\ \cos(\phi) \end{pmatrix},$$

$$\tag{6.2}$$

where

$$\Delta S = r^2 \sin(\theta)\Delta\theta\Delta\phi \tag{6.3}$$

is the size of surface element at a particular point $\mathbf{r} = (r, \theta, \phi)$. We continue using spherical coordinates and thus we only have to change the field vectors from spherical to Cartesian [1]. However, the transformed vector fields still depend on the spherical coordinates. The surface integration of the tensor will be then approximated by

$$\oiint_S \overleftrightarrow{\mathbf{T}} \cdot \mathbf{n} \mathrm{d}S \approx \sum \overleftrightarrow{\mathbf{T}}_{\mathbf{E}} \cdot \mathbf{n}\Delta S + \sum \overleftrightarrow{\mathbf{T}}_{\mathbf{B}} \cdot \mathbf{n}\Delta S, \tag{6.4}$$

where we sum over the surface elements.

We can see that from Eqs. (6.1) and (6.2) we get three components. We are particularly interested in the transverse x component but we also calculate the z component (in y we obtain negligible values originated from numerical limitations).

6.2. Evolution of Maxwell stress tensor in attosecond times

In order to visualize the properties of the components from Eqs. (6.1) and (6.2), particularly where their largest values appear, we plot them again above the particle for different attosecond times. The x component is depicted in figure 6.3, while the z component can be found in figure 6.4.

In the case of the x component we can recognize that the created patterns directly follow the distribution of the fields above the surface. However, if we consider the sign, we can see mostly positive electric contribution (left column) and on contrary negative magnetic contribution (right column) of the same order of magnitude.

Electric contribution depicted in left column of figure 6.4 is prevailing in z component and takes both positive and negative sign depending on current position of electron. Magnetic contribution is smaller.

6.3. Evolution of Maxwell stress tensor in femtosecond times

In femtoseconds, electric contribution to the Maxwell stress tensor is dominant as the magnetic field is very small. Therefore, we plotted only x and z components of (6.1) in figures 6.5 and 6.6, respectively. Patterns observed in plot of x component are again closely related to the field (see 5.4) and as we can see, it is mostly positive.

z component depicted in 6.6 takes positive and negative values symmetrically. This means that after summation, we can expect very small values of total momentum time derivative.

---

[1]The transformation of the vector field $\mathbf{V} = (V_r, V_\theta, V_\phi)$ reads $V_x = V_r\sin(\theta)\cos(\phi) + V_\theta\cos(\theta)\cos(\phi) - V_\phi\sin(\phi)$, $V_y = V_r\sin(\theta)\sin(\phi) + V_\theta\cos(\theta)\sin(\phi) + V_\phi\cos(\phi)$, $V_z = V_r\cos(\theta) - V_\theta\sin(\theta)$.
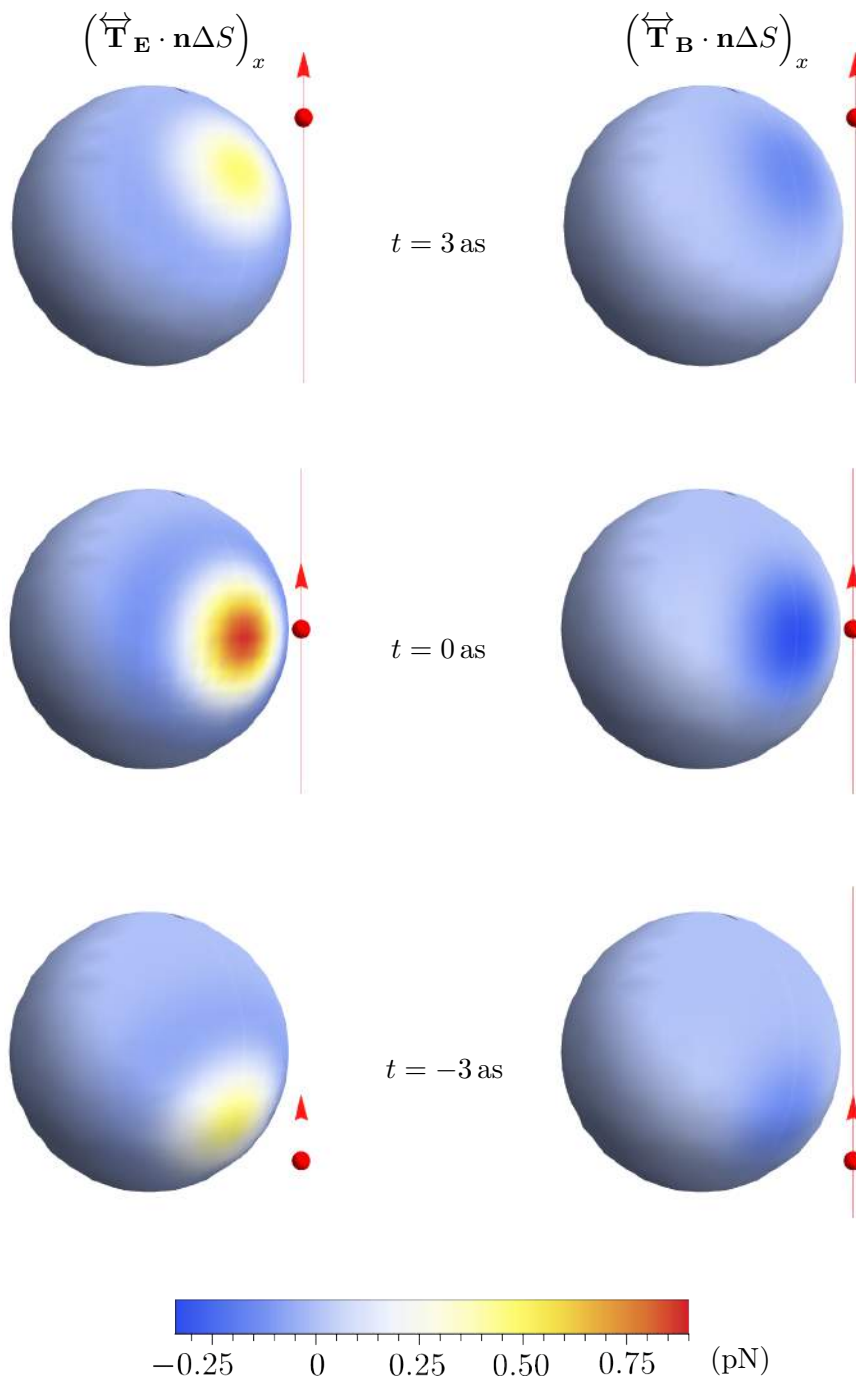
Figure 6.3: The x component of the electric part of the Maxwell stress tensor multiplied by the surface element from Eq. (6.1) (left column) and magnetic part from Eq. (6.2) (right column). Different times are displayed for each row. As we can see, the electric field contributes mainly positively, while the contribution of magnetic field is negative. Plotted patterns follow the distribution of the fields depicted in figure 5.3.
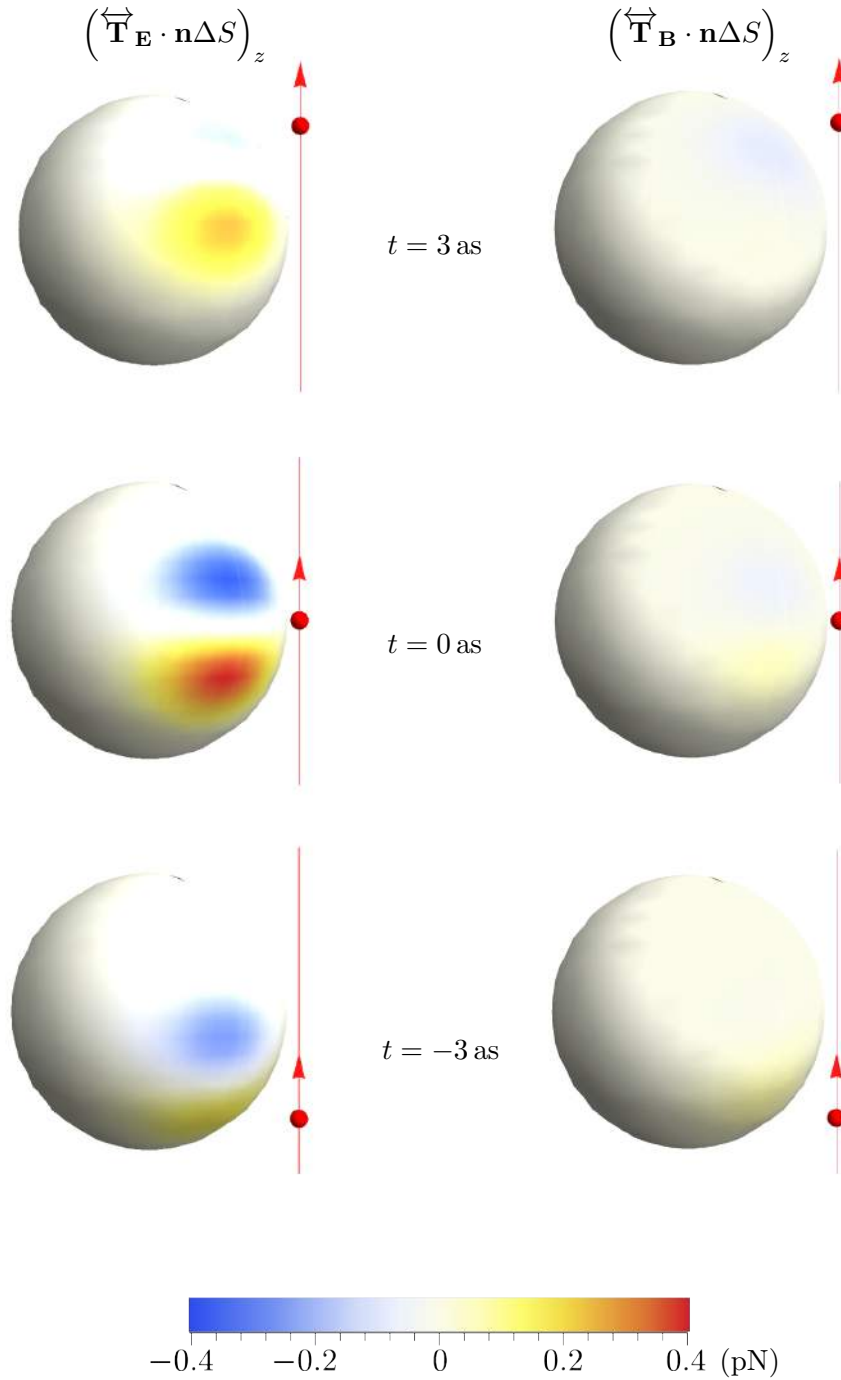
Figure 6.4: The x component of the electric part of the Maxwell stress tensor multiplied by the surface element from Eq. (6.1) (left column) and magnetic part from Eq. (6.2) (right column). Different times are displayed for each row. Contribution of the electric field is both positive and negative with the pattern depending on current position of the electron with respect to the sphere. In this case the magnetic field contributes with small values varying around zero.

$$\left(\overset{\leftrightarrow}{\mathbf{T}}_{\mathbf{E}} \cdot \mathbf{n}\Delta S\right)_x$$

$t = 0.1\,\text{fs}$

$t = 2.5\,\text{fs}$

$t = 0.3\,\text{fs}$

$t = 3.0\,\text{fs}$

$t = 0.5\,\text{fs}$

$t = 3.5\,\text{fs}$

(fN)

20

15

10

5

0

−5

$t = 1.0\,\text{fs}$

$t = 4.0\,\text{fs}$

$t = 1.5\,\text{fs}$

$t = 5.0\,\text{fs}$

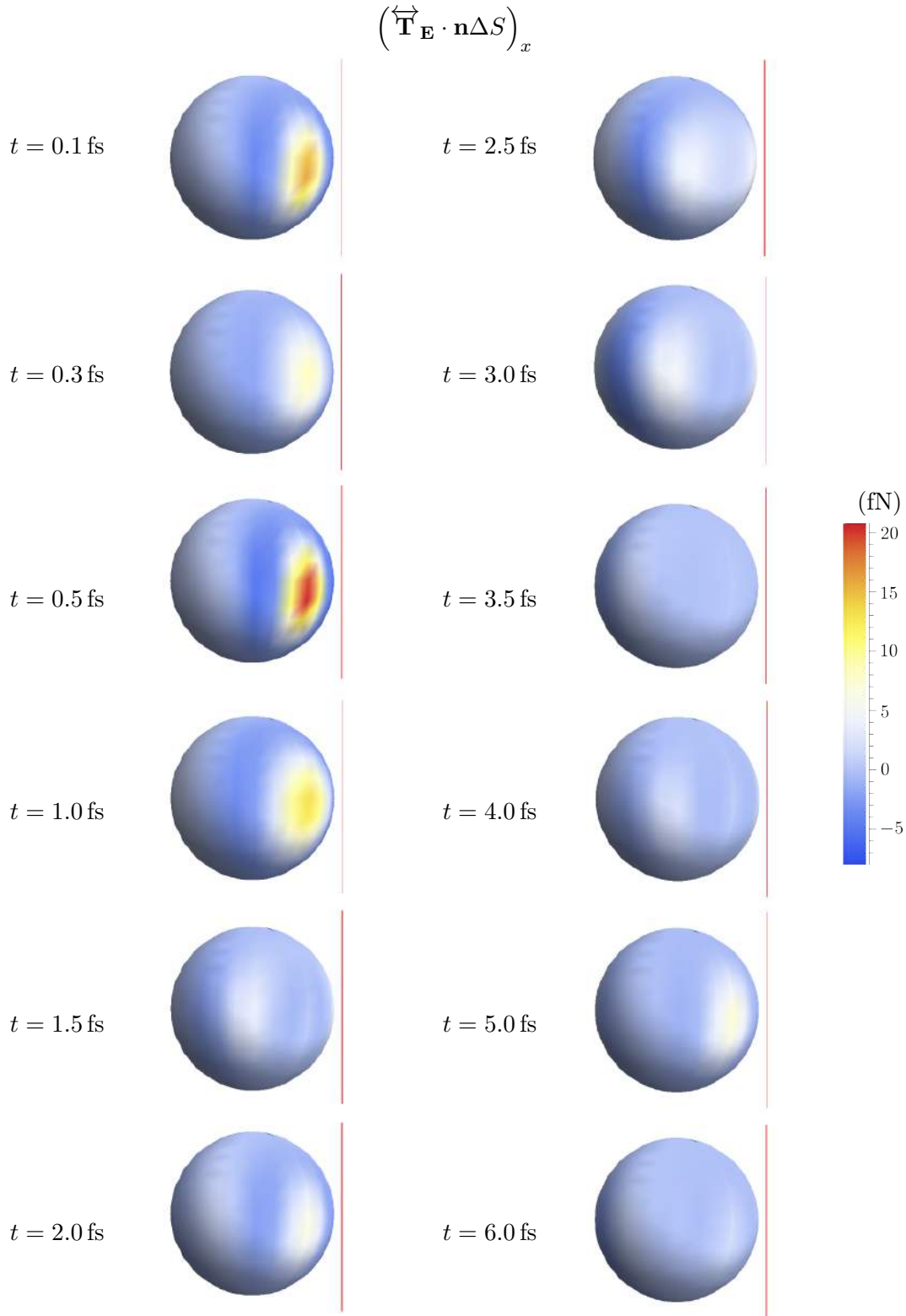$t = 2.0\,\text{fs}$

$t = 6.0\,\text{fs}$

Figure 6.5: The x component of the electric part of the Maxwell stress tensor multiplied by the surface element from Eq. (6.1) (left column) and magnetic part from Eq. (6.2) (right column). Different femtosecond times are displayed for each row. The red line represents the trajectory of the electron, which is now far away.

$$\left(\overleftrightarrow{\mathbf{T}}_{\mathbf{E}} \cdot \mathbf{n} \Delta S\right)_z$$
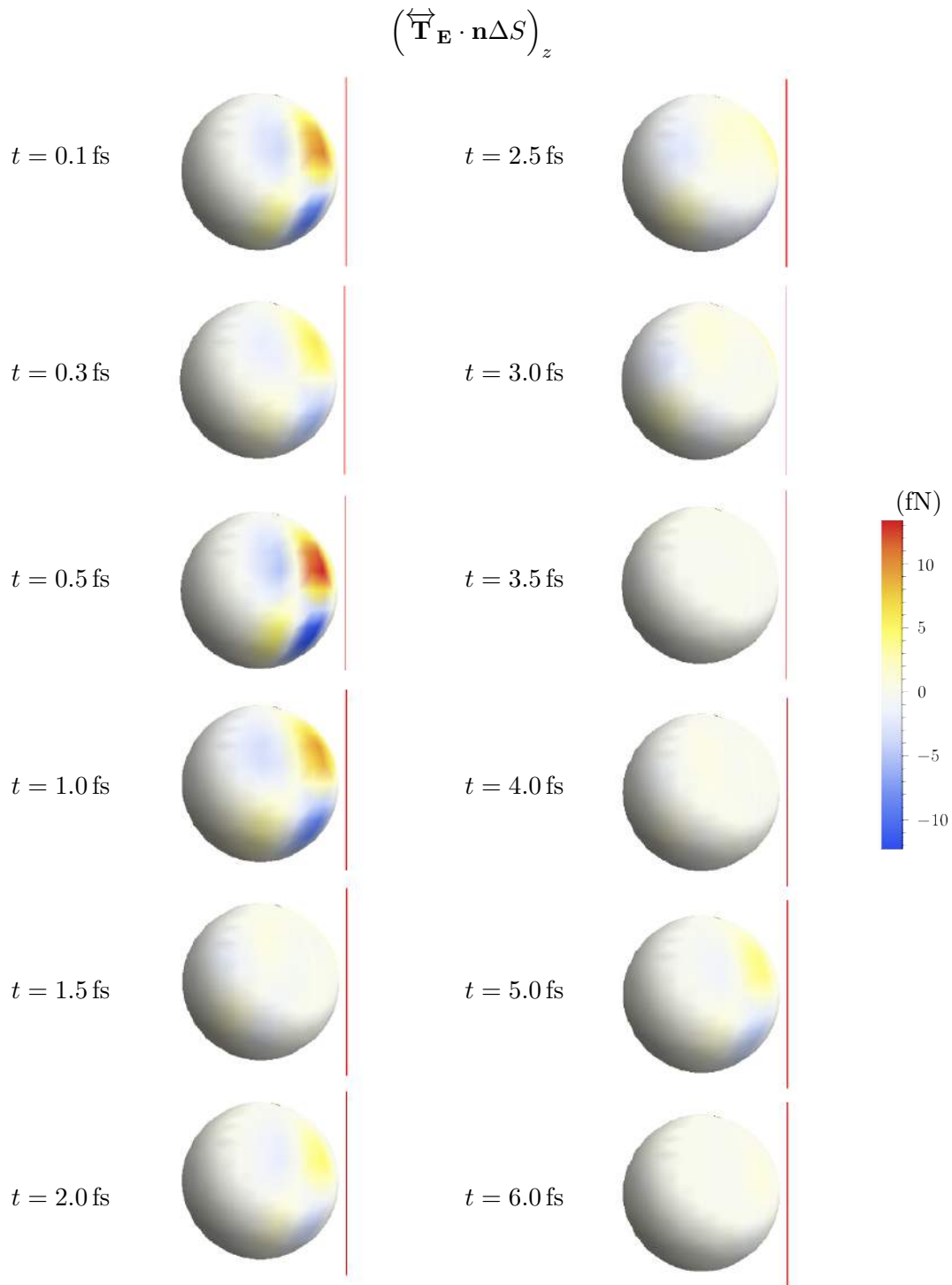

Figure 6.6: The z component of the electric part of the Maxwell stress tensor multiplied by the surface element from Eq. (6.1) (left column) and magnetic part from Eq. (6.2) (right column). Different femtosecond times are displayed for each row. The red line represents the trajectory of the electron, which is now far away.

6.4. Calculation of forces

Until now, we were plotting the time-dependent Maxwell stress tensor without saying what its meaning is in our situation. If we look at equation (1.45), we can realize that the Maxwell stress tensor integrated over closed surface gives the mechanical force $\mathbf{F}_{\mathrm{mech}} = \mathrm{d}\mathbf{p}_{\mathrm{mech}}/\mathrm{d}t$ only when the fields are static, which is not our case. Our integrated Maxwell stress tensor also includes the term corresponding to the time derivative of the field momentum $\mathrm{d}\mathbf{p}_{\mathrm{field}}/\mathrm{d}t$:

$$\oiint_{S} \overleftrightarrow{\mathbf{T}} \cdot \mathbf{n}\mathrm{d}S = \frac{\mathrm{d}\mathbf{p}_{\mathrm{mech}}}{\mathrm{d}t} + \frac{\mathrm{d}\mathbf{p}_{\mathrm{field}}}{\mathrm{d}t} = \frac{\mathrm{d}\mathbf{p}_{\mathrm{tot}}}{\mathrm{d}t} \tag{6.5}$$

Relation (1.45) was derived for vacuum, where $\mathbf{D} = \varepsilon_0 \mathbf{E}$ and $\rho = \rho_{\mathrm{F}}$. For us it is not necessary to modify the Maxwell stress tensor, which can be evaluated just above the surface of the metallic sphere in free space. However, we should modify the $\mathbf{p}_{\mathrm{field}}$ term as it is integrated over the volume of the sphere, where the assumption of a vacuum environment is no longer valid. With this modification the force acting on free charges reads

$$\mathbf{F}_{\mathrm{mech}} = \frac{\mathrm{d}\mathbf{p}_{\mathrm{mech}}}{\mathrm{d}t} = \oiint_{S} \overleftrightarrow{\mathbf{T}} \cdot \mathbf{n}\mathrm{d}S - \frac{\mathrm{d}}{\mathrm{d}t} \iiint_{V} (\varepsilon \mathbf{E}^{\mathrm{ind,in}} \times \mathbf{B}^{\mathrm{ind,in}})\mathrm{d}V. \tag{6.6}$$

Attosecond regime

In figure 6.7 we can observe the attosecond time dependence of the x component of the integrated Maxwell stress tensor without the field momentum time derivative subtraction. We plotted separately the electric contribution, which is positive in the whole time range, and the magnetic part, which contributes mostly negatively and in later times positively. The time derivative of the total momentum is obtained by summing of these two parts.
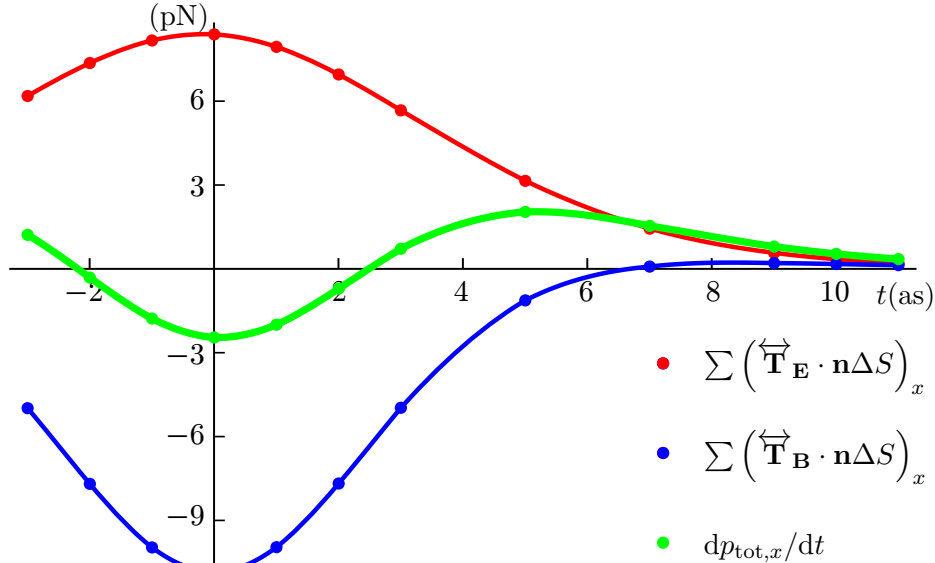

Figure 6.7: Time dependence of $\mathrm{d}p_{\mathrm{tot},x}/\mathrm{d}t$ (x component) obtained by integration of the Maxwell stress tensor over the spherical surface (green dots). We can also observe the electric (red dots) and the magnetic contribution (blue dots). Lines of the same colour interpolate the calculated data.

We calculate also the time dependence of the z component of the integrated Maxwell stress tensor in figure 6.8. The behaviour of the electric and the magnetic part is similar, i.e. for negative times it is positive and then it gets reversed.
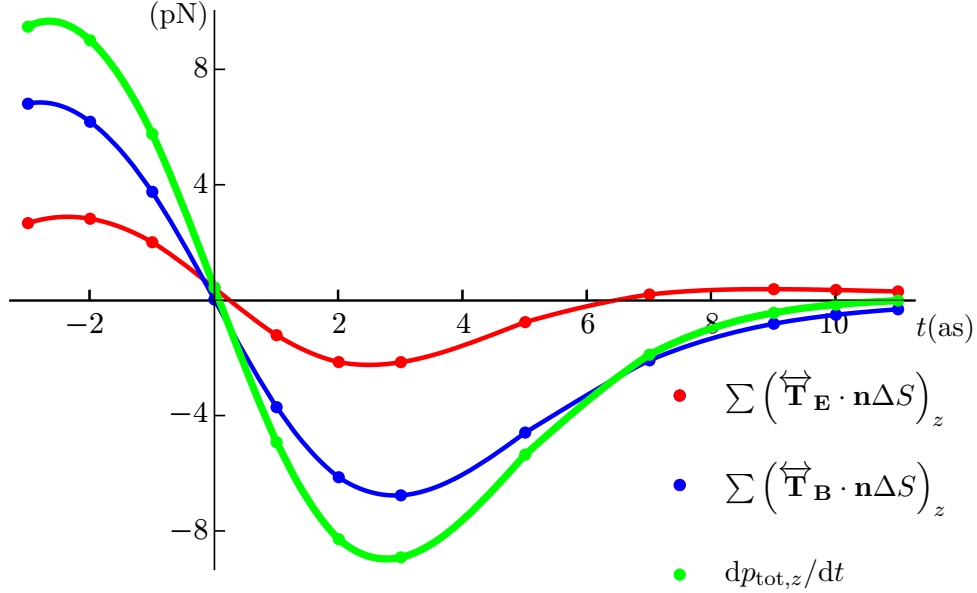

Figure 6.8: Time dependence of $\mathrm{d}p_{\mathrm{tot},z}/\mathrm{d}t$ (z component) obtained by integration of Maxwell stress tensor over the spherical surface (green dots). We can also observe the electric (red dots) and the magnetic contribution (blue dots). Lines of the same colour interpolate the calculated data.

Forces created within attoseconds are quite large, but we have to be careful, because considerable amount of the time derivative of total momentum can be connected with the time derivative of the field momentum, while the mechanical part would not play an important role. To have an idea of how big this field contribution can be to the $\mathrm{d}\mathbf{p}_{\mathrm{tot}}/\mathrm{d}t$ be, we integrated the Maxwell stress tensor over a "virtual" sphere filled by vacuum, where we used the exact analytical solution of the external fields produced by a moving electron from Eqs. (5.3) and (5.4). We took the same parameters as in previous calculations.

The results for both the x and z component are depicted in figure 6.9, where we observe qualitatively and also quantitatively very similar behaviour as in figures 6.7 and 6.8, especially in the case of the magnetic contribution. We also plot the calculated time derivative of the field momentum, which, as expected, agrees with the total one obtained from the surface integration of the Maxwell stress tensor (in this case there is no mechanical force).

Now we know that the contribution of the field momentum time can be very important, but to perform correct calculation, we have to deal with Eq. (6.6) which requires to subtract the field contribution.

So far we have performed this calculation, as it is very computationally demanding, only for time $t = 0\,\mathrm{as}$ and obtained

$$\frac{\mathrm{d}p_{\mathrm{field},x}(t=0)}{\mathrm{d}t} = -4.68812\,\mathrm{pN},$$
$$\frac{\mathrm{d}p_{\mathrm{field},z}(t=0)}{\mathrm{d}t} = 5.27117 \cdot 10^{-2}\,\mathrm{pN}.$$
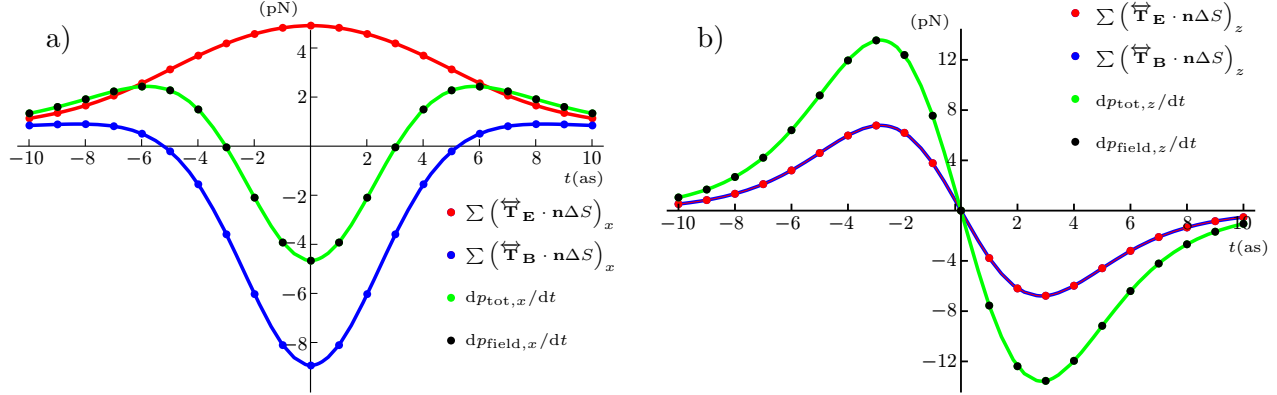
Figure 6.9: Time dependence of a) $\mathrm{d}p_{\mathrm{tot},x}/\mathrm{d}t$ (x component) and b) $\mathrm{d}p_{\mathrm{tot},z}/\mathrm{d}t$ (z component) obtained by integration of Maxwell stress tensor over the spherical surface filled by vacuum (green dots). We can also observe the electric (red dots) and the magnetic contribution (blue dots). Black dots correspond to calculated time derivative of the field momentum, which is equal to the total one. Lines of the same colour interpolate the calculated data.

After subtracting these values from the total momentum derivative, we get following values for the desired mechanical momentum

$$F_x = \frac{\mathrm{d}p_{\mathrm{mech},x}(t=0)}{\mathrm{d}t} = 2.21019\,\mathrm{pN},$$

$$F_z = \frac{\mathrm{d}p_{\mathrm{mech},z}(t=0)}{\mathrm{d}t} = 0.394397\,\mathrm{pN}.$$

According to this calculation, it seems that even after field momentum time derivative subtraction, the mechanical momentum transfer in attosecond regime will be nonzero and in order of pN. However, we still have to be careful, because we restricted the maximum number of modes to $n_{\mathrm{max}} = 5$ and convergence tests related to the "mesh" refinement would be required.

Femtosecond regime

In the femtosecond regime, we calculated the forces in the same manner as in case of the attosecond regime. When we sum up the electric and magnetic contribution, we find out that the magnetic part contributes with a force of the order of aN which is three orders of magnitude smaller than the electric one of the order of fN. This could be expected because the magnitude of magnetic field during these times is very small as we presented in figure 5.5.

The x and z component of the electric part is plotted in figures 6.10 and 6.12, respectively. The sum of magnetic contribution for different femtosecond times can be found in graphs 6.11 and 6.13.

We should remark that except at $t = 3\,\mathrm{fs}$, the x component of the total momentum time derivative is always positive, whereas the z component is going from positive to negative values and then back to positive. Both dependences exhibit quite oscillating behaviour. However, as we emphasized, also in the femtosecond regime we need to subtract the field momentum time derivative at each time to obtain the pure mechanical force acting on the particle.
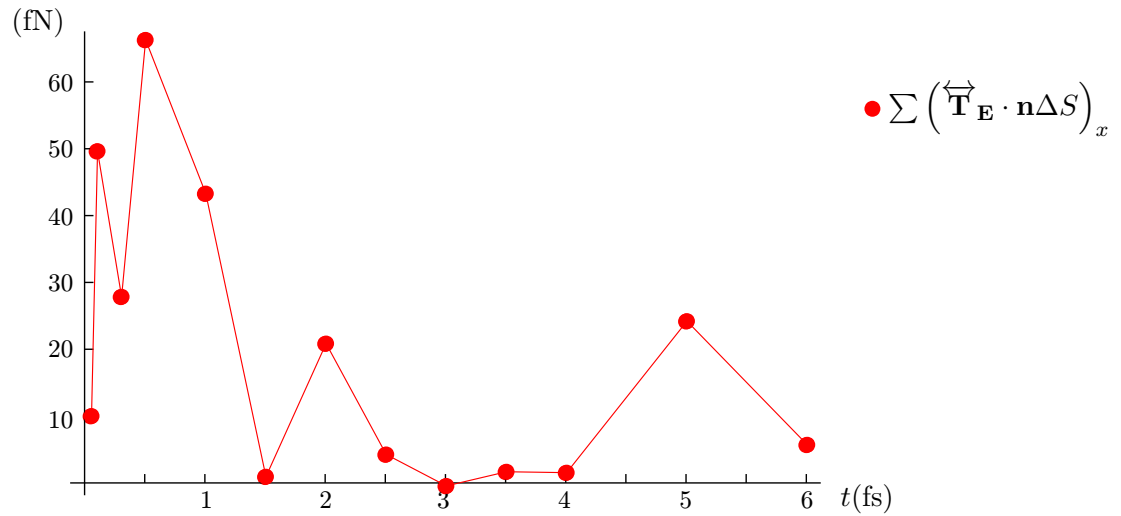
Figure 6.10: Time dependence of electric contribution to the $dp_{\text{tot},x}$ plotted for femtoseconds after the electron flyby obtained by summing the values displayed on the surface of the spheres in figure 6.5. Red lines connecting the calculated points serve as a guide for eye.

Figure 6.11: Time dependence of magnetic contribution to the $dp_{\text{tot},x}$ plotted for femtoseconds after the electron flyby. Blue lines connecting the calculated points serve as a guide for eye.

Figure 6.12: Time dependence of electric contribution to the $\mathrm{d}p_{\mathrm{tot},z}$ plotted for femtoseconds after the electron flyby obtained by summing the values displayed on the surface of the spheres in figure 6.6. Red lines connecting the calculated points serve as a guide for eye.
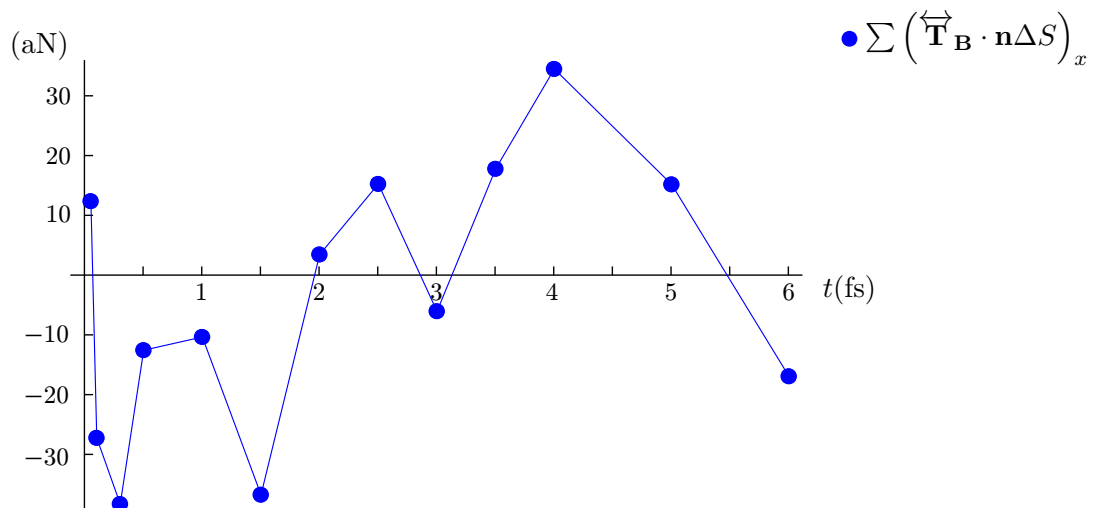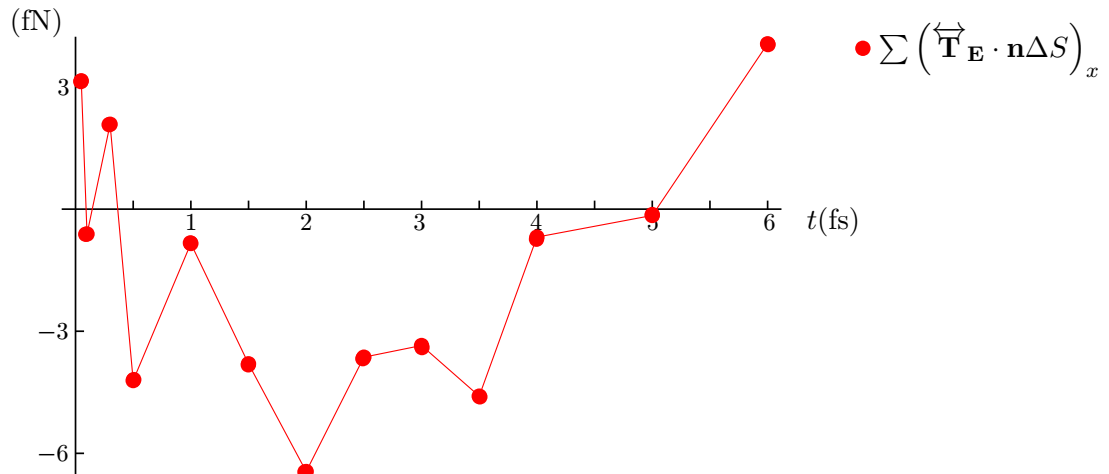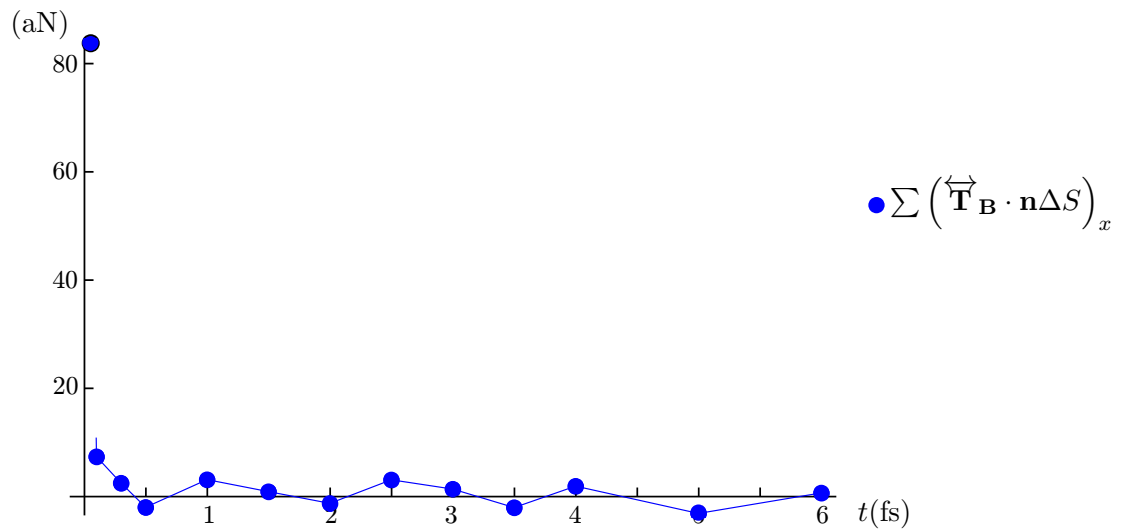

Figure 6.13: Time dependence of magnetic contribution to the $\mathrm{d}p_{\mathrm{tot},z}$ plotted for femtoseconds after the electron flyby. Blue lines connecting the calculated points serve as a guide for eye.

7. Summary

In this master thesis we dealt with the theoretical description of the fields inside and outside of a small metallic sphere influenced by fast electron passing by its close proximity and therefore producing external disturbance. This problem is very important for the fundamental understanding of many interesting phenomena, since an ambiguous behaviour of the nanoparticle has been predicted. The particle can experience both attraction and repulsion with respect to electron beam, depending on impact parameter.

First we briefly introduced the theory of the electromagnetic field and the formalism used to describe the spectra in electron energy loss spectroscopy, which is closely related to our problem. We also described three basic numerical approaches that are commonly used, when we need to solve the problem of electron energy loss. Our main interest is focused on the boundary element method, which was utilized for comparison with analytical results in following chapters.

Then we continued with previously developed approaches leading to analytical expressions of the fields outside the sphere exploiting multipole expansion and showed, how the fields look like in frequency domain. We compared calculated EEL spectra and the fields with numerical results obtained from the boundary element method.

In the main part of the thesis we transformed the fields from frequency to time domain as we wanted to reveal, what is happening in real time when the electron passes near the particle, and discussed the results for two different time scales – attoseconds and femtoseconds. Attoseconds correspond to times of the closest approach of electron to the particle, which can feel large external fields. However, at this time scale particle is not able to respond and the induced fields are very small. On the contrary, in the femtosecond regime localized surface plasmon oscillations are generated as a response to external fields that were acting on the particle in attoseconds. During these times, the electron is very far from the particle, but the induced fields are quite large.

The last section was devoted to calculations of the mechanical force acting on the particle as we wanted to find out the reason why the particle sometimes experiences attraction and sometimes repulsion. We were dealing with this problem again in attoseconds and then in femtoseconds. We performed the surface integration of Maxwell stress tensor, which represents the time derivative of the total momentum. However, we showed that this is not equal to the mechanical force, which can be obtained by subtraction of the field momentum time derivative. As these calculations are very computationally demanding, we were able to calculate the pure mechanical force for time ($t = 0\,\mathrm{as}$).

What seems crucial for future calculations, is not only the emphasized subtraction of field momentum time derivative to obtain the force causing the nanoparticle movement, but also the testing of convergence for increasing n_{max}, more points where the fields are calculated and more sophisticated models for dielectric functions characterizing the response of the particle. We should also think about the validity of our approach which does not take nonlocality [12] into account or treats the electron as a localized particle.

68

Bibliography

[1] Lumerical Knowledge Base. http://docs.lumerical.com/en/index.html?nanophotonic_applications_electron_beam_spectroscopy.html. Accessed: 2014-06-12.

[2] Lumerical Solutions, Inc. http://www.lumerical.com/tcad-products/fdtd/. Accessed: 2014-06-12.

[3] MATLAB. http://www.mathworks.com. Accessed: 2014-06-12.

[4] ABRAMOWITZ, M., AND STEGUN, I. A. *Handbook of Mathematical Functions with Formulas, Graphs, and Mathematical Tables.* Dover, New York, 1964.

[5] AIZPURUA, J. *Coupling of electrons and electromagnetic surface modes in scanning transmission electron microscopy.* PhD thesis, Euskal Herriko Unibersitatea, 1998.

[6] ASHCROFT, N. W., AND MERMIN, D. N. *Solid state physics*, 1 ed. Thomson Learning, Toronto, 1976.

[7] BATSON, P. E., REYES-CORONADO, A., BARRERA, R. G., RIVACOBA, A., ECHENIQUE, P. M., AND AIZPURUA, J. Plasmonic nanobilliards: Controlling nanoparticle movement using forces induced by swift electrons. *Nano Letters 11*, 8 (2011), 3388–3393.

[8] BIGELOW, N. W., VASCHILLO, A., IBERI, V., CAMDEN, J. P., AND MASIELLO, D. J. Characterization of the electron- and photon-driven plasmonic excitations of metal nanorods. *ACS Nano 6*, 8 (2012), 7497–7504.

[9] BOHREN, C. F., AND HUFFMAN, D. R. *Absorption and Scattering of Light by Small Particles.* Wiley-VCH, 1998.

[10] CRETU, O., RODRÍGUEZ-MANZO, J., DEMORTIÈRE, A., AND BANHART, F. Electron beam-induced formation and displacement of metal clusters on graphene, carbon nanotubes and amorphous carbon. *Carbon 50*, 1 (2012), 259–264.

[11] DAS, P., CHINI, T. K., AND POND, J. Probing higher order surface plasmon modes on individual truncated tetrahedral gold nanoparticle using cathodoluminescence imaging and spectroscopy combined with fdtd simulations. *The Journal of Physical Chemistry C 116*, 29 (2012), 15610.

[12] DAVID, C., AND GARCÍA DE ABAJO, F. J. Spatial nonlocality in the optical response of metal nanoparticles. *The Journal of Physical Chemistry C 115*, 40 (2011), 19470–19475.

[13] DRAINE, B. T. The discrete-dipole approximation and its application to interstellar graphite grains. *Astrophysical Journal 333* (1988), 848.

[14] DUFFY, D. G. *Green's Functions with Applications.* Chapman & Hall/CRC, 2001.

[15] ECHENIQUE, P. M., AND PENDRY, J. B. Absorption profile at surfaces. *Journal of Physics C 8* (1975), 2936–2942.

[16] ETCHEGOIN, P. G., LE RU, E. C., AND MEYER, M. An analytic model for the optical properties of gold. *The Journal of Chemical Physics 125*, 16 (2006), –.

[17] FERMI, E. The ionization loss of energy in gases and in condensed materials. *Physical Review 57* (1940), 485.

[18] FERRELL, T. L., AND ECHENIQUE, P. M. Generation of surface excitations on dielectric spheres by an external electron beam. *Physical Review Letters 55* (1985), 1526–1529.

[19] FOX, M. *Optical Properties of Solids*. OUP, Oxford, 2010.

[20] GARCÍA DE ABAJO, F. J. Relativistic energy loss and induced photon emission in the interaction of a dielectric sphere with an external electron beam. *Physical Review B 59*, 4 (1999), 3095–3107.

[21] GARCÍA DE ABAJO, F. J. Momentum transfer to small particles by passing electron beams. *Physical Review B 70* (2004), 115422.

[22] GARCÍA DE ABAJO, F. J. Optical excitations in electron microscopy. *Reviews of Modern Physics 82*, 1 (2010), 209–275.

[23] GARCÍA DE ABAJO, F. J., AND AIZPURUA, J. Numerical simulation of electron energy loss near inhomogeneous dielectrics. *Physical Review B 56*, 24 (1997), 15873.

[24] GARCÍA DE ABAJO, F. J., AND HOWIE, A. Relativistic electron energy loss and electron-induced photon emission in inhomogeneous dielectrics. *Physical Review Letters 80*, 23 (1998), 5180.

[25] GARCÍA DE ABAJO, F. J., AND HOWIE, A. Retarded field calculation of electron energy loss in inhomogeneous dielectrics. *Physical Review B 65*, 11 (2002), 115418.

[26] GARCIA-MOLINA, R., GRAS-MARTI, A., HOWIE, A., AND RITCHIE, R. H. Retardation effects in the interaction of charged particle beams with bounded condensed media. *Journal of Physics C: Solid State Physics 18*, 27 (1985), 5335.

[27] GEUQUET, N., AND HENRARD, L. EELS and optical response of a noble metal nanoparticle in the frame of a discrete dipole approximation. *Ultramicroscopy 110*, 8 (2010), 1075.

[28] GUILLAUME, S.-O., DE ABAJO, F. J. G., AND HENRARD, L. Efficient modal-expansion discrete-dipole approximation: Application to the simulation of optical extinction and electron energy-loss spectroscopies. *Physical Review B 88* (Dec 2013), 245439.

[29] HILLIER, J., AND BAKER, R. F. Microanalysis by means of electrons. *Journal of Applied Physics 15*, 9 (1944), 663–675.

[30] HOHENESTER, U. Simulating electron energy loss spectroscopy with the MNPBEM toolbox. *Computer Physics Communications 185*, 3 (2014), 1177–1187.

[31] HOHENESTER, U., AND TRÜGLER, A. MNPBEM: A Matlab toolbox for the simulation of plasmonic nanoparticles. *Computer Physics Communications 183*, 2 (2012), 370–381.

[32] JACKSON, J. D. *Classical Electrodynamics*, 3rd ed. John Wiley & Sons, New York, 1998.

[33] KOH, A. L., FERNÁNDEZ-DOMÍNGUEZ, A. I., MCCOMB, D. W., MAIER, S. A., AND YANG, J. K. W. High-resolution mapping of electron-beam-excited plasmon modes in lithographically defined gold nanostructures. *Nano Letters 11*, 3 (2011), 1323–1330.

[34] Komrska, J. *Fourierovské metody v teorii difrakce a ve strukturní analýze.* VUTIUM, Brno, 2001.

[35] Komrska, J. *Vlnová optika, část Difrakce světla.* Akademické nakladatelství CERM, s.r.o., Brno, 2004.

[36] Low, F. E. *Classical Field Theory: Electromagnetism and Gravitation.* John Wiley & Sons, New York, 1997.

[37] Lucas, A. A., and Šunjić, M. Fast-electron spectroscopy of surface excitations. *Physical Reviw Letters 26* (1971), 229–232.

[38] Maier, S. A. *Plasmonics: Fundamentals and Applications.* Springer, Bath UK, 2007.

[39] Mie, G. Beiträge zur Optik trüber Medien, speziell kolloidaler Metallösungen. *Annalen der Physik 330,* 3 (1908), 377–445.

[40] Morse, P. M., and Feshbach, H. *Methods of Theoretical Physics.* McGraw-Hill, 1953.

[41] Nelayah, J., Kociak, M., Stephan, O., García de Abajo, F. J., Tence, M., Henrard, L., Taverna, D., Pastoriza-Santos, I., Liz-Marzán, L. M., and Colliex, C. Mapping surface plasmons on a single metallic nanoparticle. *Nature Physics 3,* 5 (2007), 348–353.

[42] Novotny, L., and Hecht, B. *Principles of Nano-Optics.* Cambridge University Press, 2006.

[43] Palik, E. D. *Handbook of Optical Constants of Solids.* Academic Press, New York, 1985.

[44] Pelton, M., Aizpurua, J., and Bryant, G. Metal-nanoparticle plasmonics. *Laser & Photonics Reviews 2,* 3 (2008), 136–159.

[45] Pennycook, S. J., and Nellist, P. D., Eds. *Scanning Transmission Electron Microscopy.* Springer, 2011.

[46] Raki, A. D., Djuriši, A. B., Elazar, J. M., and Majewski, M. L. Optical properties of metallic films for vertical-cavity optoelectronic devices. *Applied Optics 37,* 22 (1998), 5271–5283.

[47] Reyes-Coronado, A., Barrera, R. G., Batson, P. E., Echenique, P. M., Rivacoba, A., and Aizpurua, J. Electromagnetic forces on plasmonic nanoparticles induced by fast electron beams. *Physical Review B 82* (2010), 235429.

[48] Ritchie, R. H. Plasma losses by fast electrons in thin films. *Physical Review 106* (1957), 874–881.

[49] Rivacoba, A., Zabala, N., and Aizpurua, J. Image potential in scanning transmission electron microscopy. *Progress in Surface Science 65,* 1–2 (2000), 1–64.

[50] Ruthemann, G. Diskrete Energieverluste schneller Elektronen in Festkörpern. *Naturwissenschaften 29* (1941), 145.

[51] Stern, E. A., and Ferrell, R. A. Surface plasma oscillations of a degenerate electron gas. *Physical Review 120* (1960), 130–136.

[52] Stratton, J. A. *Electromagnetic Theory.* McGraw-Hill, New York, 1941.

[53] Zheng, H. Using molecular tweezers to move and image nanoparticles. *Nanoscale 5* (2013), 4070–4078.

[54] Zheng, H., Mirsaidov, U. M., Wang, L.-W., and Matsudaira, P. Electron beam manipulation of nanoparticles. *Nano Letters 12*, 11 (2012), 5644–5648.

Appendix A: Mathematical apparatus

Delta distribution

Dirac delta distribution (sometimes called function although it does not fulfil strict mathematical requirements on functions) is very useful when we want e.g. express local response. It can be defined in different ways, the most common is [34]:

$$\int\limits_{-\infty}^{\infty} \delta(x)\mathrm{d}x = 1, \qquad \delta(x) = 0 \quad \text{for} \quad x \neq 0. \tag{A1}$$

Delta distribution has so-called sifting property, which can also serve as a definition of the distribution and is expressed as [14]

$$\int\limits_{x_1}^{x_2} f(x)\delta(x - x_0)\mathrm{d}x = \begin{cases} \frac{1}{2}[f(x_0^-) + f(x_0^+)] & \text{if } x_0 \in (x_1, x_2), \\ \frac{1}{2}f(x_0^+) & \text{if } x_0 = x_1, \\ \frac{1}{2}f(x_0^-) & \text{if } x_0 = x_2, \\ 0 & \text{if } x_0 \notin \langle x_1, x_2 \rangle, \end{cases}$$

and for continuous $f(x)$ becomes

$$\int\limits_{x_1}^{x_2} f(x)\delta(x - x_0)\mathrm{d}x = f(x_0) \qquad \text{when} \qquad x_0 \in (x_1, x_2). \tag{A2}$$

There exist many equalities, but for now we pick up that properties of delta distribution that are used in this thesis:

$$\delta(x) = \delta(-x),$$
$$\delta(ax - x_0) = \frac{1}{|a|}\delta\left(x - \frac{x_0}{a}\right),$$
$$f(x)\delta(x - a) = f(a)\delta(x - a),$$
$$\delta(x - a) = \frac{1}{2\pi} \int\limits_{-\infty}^{\infty} \exp(\mathrm{i}p(x - a))\mathrm{d}p.$$

We can also get delta distribution from a complete orthonormal set of functions on interval $\{x_1, x_1 + a\}$, $x, x_0 \in (x_1, x_1 + a)$

$$\sum_n \Psi_n^*(x)\Psi_n(x_0) = \delta(x - x_0). \tag{A3}$$

For delta distribution in E_N in Cartesian coordinate system following relations hold

$$\int_D \cdots \int f(\mathbf{x})\delta(\mathbf{x} - \mathbf{x}_0)\mathrm{d}^N\mathbf{x} = f(\mathbf{x}_0) \qquad \text{when} \qquad \mathbf{x}_0 \in D,$$

$$\delta(\mathbf{x} - \mathbf{x}_0) = \prod_{k=1}^{N} \delta(x_k - x_{0k}),$$

$$\delta(a\mathbf{x}) = \frac{1}{|a|^N}\delta(\mathbf{x}).$$

Fourier transform

Fourier transform is a special case of integral transformation and is very important in many fields (e.g. physics, mathematics or electrotechnics). We can define Fourier transform and inverse Fourier transform by expressions [34]

$$\mathrm{FT}\{f(\mathbf{x})\} = A^N \int_{-\infty}^{\infty} \cdots \int f(\mathbf{x})\exp(-\mathrm{i}k\mathbf{X}\cdot\mathbf{x})\mathrm{d}^N\mathbf{x}, \tag{A4}$$

$$\mathrm{FT}^{-1}\{F(\mathbf{X})\} = B^N \int_{-\infty}^{\infty} \cdots \int F(\mathbf{X})\exp(\mathrm{i}k\mathbf{X}\cdot\mathbf{x})\mathrm{d}^N\mathbf{X}, \tag{A5}$$

where constants A, B and k have to fulfill the condition

$$AB = \frac{|k|}{2\pi}, \tag{A6}$$

In points of continuity, functions $f(\mathbf{x}) = \mathrm{FT}^{-1}\{F(\mathbf{X})\}$ and $F(\mathbf{X}) = \mathrm{FT}\{f(\mathbf{x})\}$ are coupled via Fourier transformation.

If we want to transform a function dependent on both space variables (in E_3 space) and time variables, we employ Fourier transform in form

$$\mathrm{FT}\{f(\mathbf{r},t)\} = F(\mathbf{k},\omega) = \iiiint_{-\infty}^{\infty} f(\mathbf{r},t)\exp[-\mathrm{i}(\mathbf{k}\cdot\mathbf{r} - \omega t)]\mathrm{d}^3\mathbf{r}\mathrm{d}t, \tag{A7}$$

while its inverse transform reads

$$\mathrm{FT}\{F(\mathbf{k},\omega)\} = f(\mathbf{r},t) = \left(\frac{1}{2\pi}\right)^4 \iiiint_{-\infty}^{\infty} F(\mathbf{k},\omega)\exp[\mathrm{i}(\mathbf{k}\cdot\mathbf{r} - \omega t)]\mathrm{d}^3\mathbf{k}\mathrm{d}\omega. \tag{A8}$$

Properties of Fourier transform

An extensive literature dealing with properties of Fourier transform exists, we used nice book with applications on physical problems [34]. We present here a short overview of properties used in our work:

1. Relations for Fourier transform of derivatives with respect to spatial and time variables

$$\mathrm{FT}\left\{\frac{\partial f(\mathbf{r},t)}{\partial t}\right\} = -\mathrm{i}\omega\mathrm{FT}\{f(\mathbf{r},t)\}, \qquad \mathrm{FT}\left\{\frac{\partial f(\mathbf{r},t)}{\partial x_i}\right\} = \mathrm{i}k_i\mathrm{FT}\{f(\mathbf{r},t)\}. \tag{A9}$$

2. Fourier transform of convolution is equal to product of Fourier transforms

$$\text{FT}\{f(\mathbf{x}) \star g(\mathbf{x})\} = \frac{1}{A^N}\text{FT}\{f(\mathbf{x})\}\text{FT}\{g(\mathbf{x})\}, \tag{A10}$$

where convolution is defined via

$$f(\mathbf{x}) \star g(\mathbf{x}) = \int\limits_{-\infty}^{\infty} \cdots \int f(\mathbf{y})g(\mathbf{x} - \mathbf{y})\mathrm{d}^N\mathbf{y} \tag{A11}$$

Fourier transform of real function and the Rayleigh-Parseval theorem

Important theorem states that if Fourier integral of function $f(\mathbf{x})$ exists, the function is real if and only if $F(\mathbf{X})$ is hermitian

$$f(\mathbf{x}) = f^*(\mathbf{x}) \iff F(\mathbf{X}) = F^*(-\mathbf{X}) \tag{A12}$$

If we have two functions $f_1(\mathbf{x})$ and $f_2(\mathbf{x})$ and their Fourier transforms $F_1(\mathbf{X}) = \text{FT}\{f_1(\mathbf{x})\}$ and $F_2(\mathbf{X}) = \text{FT}\{f_2(\mathbf{x})\}$, following equality holds:

$$A^N \int\limits_{-\infty}^{\infty} \cdots \int f_1(\mathbf{x})f_2^*(\mathbf{x})\mathrm{d}^N\mathbf{x} = B^N \int\limits_{-\infty}^{\infty} \cdots \int F_1(\mathbf{X})F_2^*(\mathbf{X})\mathrm{d}^N\mathbf{X}. \tag{A13}$$

Now let us consider the special case, when $f_1(t)$ and $f_2(t)$ are real functions of time ($f_1(t) = f_1^*(t)$, $f_2(t) = f_2^*(t)$). If we substitute these functions in Eq. (A13) and use Eq. (A12), we obtain (with our particular choice of coefficients)

$$\int\limits_{-\infty}^{\infty} f_1(t)f_2(t)\mathrm{d}t = \frac{1}{2\pi}\int\limits_{-\infty}^{\infty} F_1(\omega)F_2^*(\omega)\mathrm{d}\omega = \frac{1}{\pi}\int\limits_{0}^{\infty} \text{Re}\left[F_1(\omega)F_2(\omega)\right]\mathrm{d}\omega. \tag{A14}$$

Appendix B: Optical properties of metals

To find optical properties of metals, we use the framework of classical Lorentz-Drude model (sometimes called only Drude model), which treats the metal as an environment containing heavy positive ions sitting in a crystalline lattice and an electron gas composed of conduction electrons. We then assume so heavy ions, that their movement is negligible compared to the electrons, which move freely but suffer instantaneous collisions. Between the collisions they do not interact with the fields of positive ions neither other electrons [6].

If we apply external electric field $\mathbf{E}$, the electrons will experience force acting on them. Then we get equation of motion

$$\ddot{\mathbf{r}}m_{\mathrm{e}} + \dot{\mathbf{r}}m_{\mathrm{e}}\gamma = -e\mathbf{E}, \tag{B1}$$

where $\mathbf{r}$ is a displacement vector, m_{e} is electron mass and γ is a probability of scattering event per unit time. If we expect harmonically time-dependent external field ($\mathbf{E}(t) = \mathbf{E_0}\exp(-\mathrm{i}\omega t)$), solution will take the form

$$\mathbf{r}(t) = \frac{e}{m_{\mathrm{e}}}\frac{1}{\omega^2 + \mathrm{i}\gamma\omega}\mathbf{E}(t). \tag{B2}$$

As the electrons are being displaced from their equilibrium positions, the matter gets polarized. The polarization vector is defined as average value of dipole moment ($\mathbf{p} = -e\mathbf{r}$) in unit volume, therefore in this case it can be expressed as

$$\mathbf{P}(t) = -\frac{\mathcal{N}e^2}{m_{\mathrm{e}}(\omega^2 + \mathrm{i}\gamma\omega)}\mathbf{E}(t), \tag{B3}$$

where $\mathcal{N}$ is number of electrons per unit volume. After comparison of Eq. (B3) with Eq. (1.14) and considering Eq. (1.16), we finally get expression for dielectric function

$$\varepsilon_{\mathrm{r}} = 1 - \frac{\omega_{\mathrm{p}}^2}{\omega^2 + \mathrm{i}\gamma\omega}, \tag{B4}$$

where we introduced the plasma frequency $\omega_{\mathrm{p}}^2 = \mathcal{N}e^2/\varepsilon_0 m_{\mathrm{e}}$. We can also include other non-resonant contributions to polarization and modify Eq. (B4)

$$\varepsilon_{\mathrm{r}} = \varepsilon_\infty - \frac{\omega_{\mathrm{p}}^2}{\omega^2 + \mathrm{i}\gamma\omega}. \tag{B5}$$

We can also write the dielectric function by the terms of its real and imaginary part

$$\varepsilon_{\mathrm{r}} = \varepsilon_{\mathrm{r1}} + \mathrm{i}\varepsilon_{\mathrm{r2}}, \tag{B6}$$

where the real and imaginary part read

$$\varepsilon_{\mathrm{r1}} = \mathrm{Re}\{\varepsilon_{\mathrm{r}}\} = \varepsilon_\infty - \frac{\omega_{\mathrm{p}}^2}{\omega^2 + \gamma^2}, \tag{B7}$$

$$\varepsilon_{\mathrm{r1}} = \mathrm{Im}\{\varepsilon_{\mathrm{r}}\} = \frac{\omega_{\mathrm{p}}^2}{\omega(\omega^2 + \gamma^2)}. \tag{B8}$$

In table B.1 there are summarized Drude parameters used within the MNPBEM toolbox [31] for three different metals (silver, gold and aluminum). Drude dielectric functions (B5) of these

metals are plotted together with experimental data from reference [43] in figures B.1, B.2 and B.3, respectively. We can see that experimental data measured for gold do not match the model as well as in the case of aluminum and silver especially due to the interband transitions.

	ω_{p}	γ	ε_{∞}
Ag	9.07	0.022	3.3
Au	9.07	0.066	10.0
Al	15.83	1.06	1.0

Table B.1: Drude parameters for silver, gold and aluminum used within the MNPBEM toolbox [31].

The contribution of the electron interband transitions to the dielectric function can be modelled by additional Lorentz oscillators:

$$\varepsilon_{\mathrm{r}} = \varepsilon_{\infty} - \frac{\omega_{\mathrm{p}}^2}{\omega^2 + \mathrm{i}\gamma\omega} + \sum_{j} \frac{\omega_{\mathrm{p}}^2 f_j}{\omega_{0,j}^2 - \omega^2 - \mathrm{i}\gamma_j\omega}, \tag{B9}$$

where f_j is a strength, $\omega_{0,j}$ a frequency and γ_j a damping related to the Lorentz oscillator, which represents a particular transition [19], [46]. This becomes very important especially in the case of optical properties of gold which, as we can see in figure B.2, can be described by simple Lorentz-Drude model only for narrow band of energies up to 2.5 eV. More sophisticated treatment of the dielectric function of gold can be found in reference [16] and in [46] where they were dealing also with other metals.
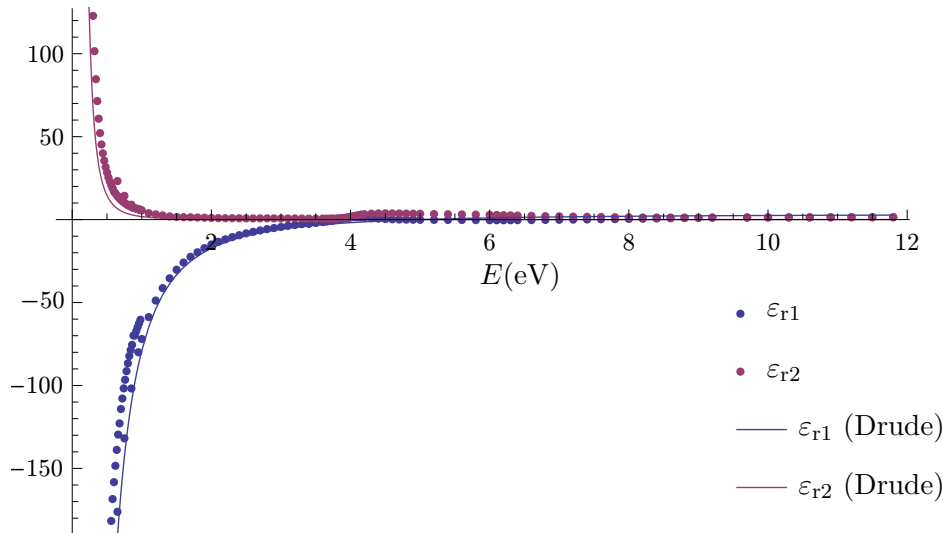

Figure B.1: Lorentz-Drude dielectric function of silver (solid lines) with parameters from table B.1 and experimental data taken from [43] (dots).
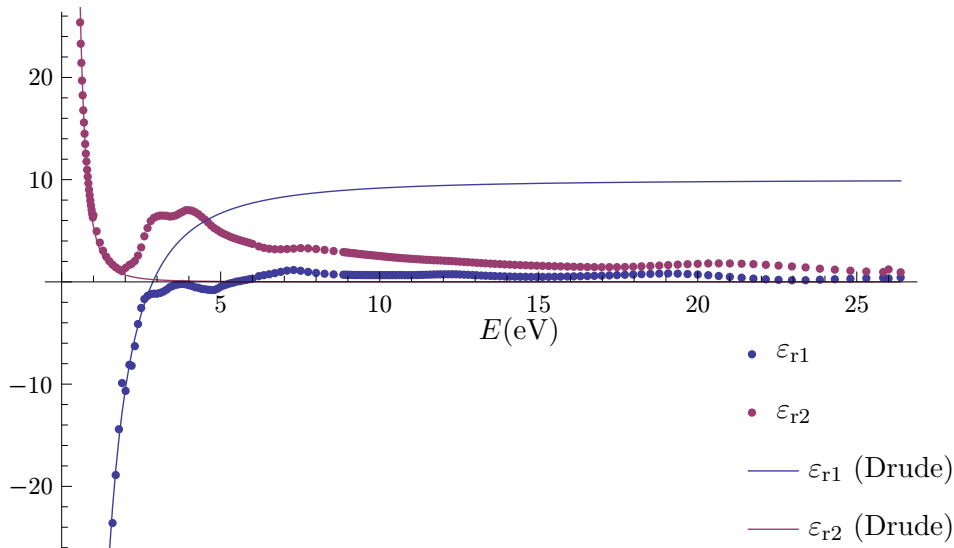
Figure B.2: Lorentz-Drude dielectric function of gold (solid lines) with parameters from table B.1 and experimental data taken from [43] (dots).
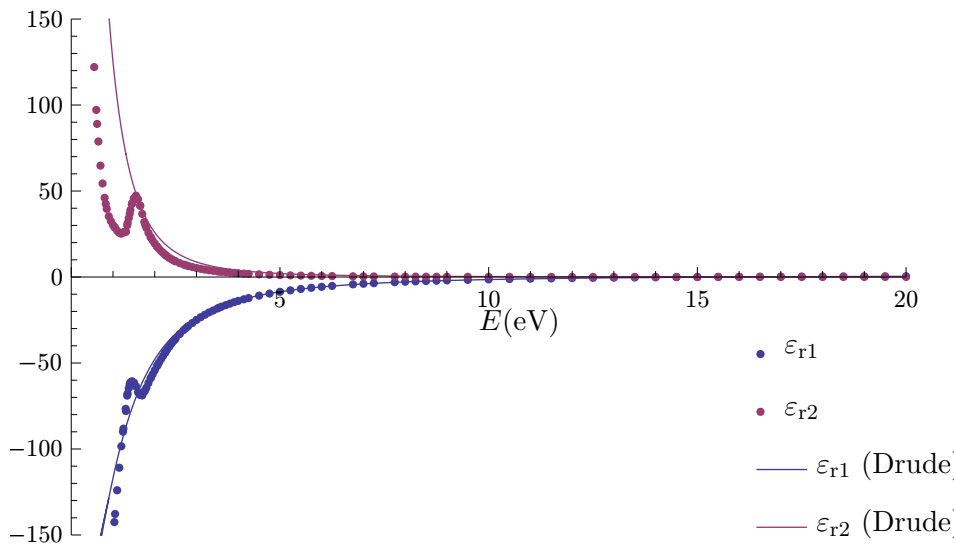

Figure B.3: Drude dielectric function of aluminum (solid lines) with parameters from table B.1 and experimental data taken from [43] (dots).